Particle size distribution of methane hydrates and particle growth using a CFD-PBM model

Master Thesis in Process Technology
by
Claus Mevik

University of Bergen, Department of Physics and Technology

June 2018

Acknowledgements

First of all I would like to express my gratitude to my supervisors Professor Pawel Kosinski and Professor Boris Balakin for introducing such an interesting topic for my thesis. In addition to excellent guidance throughout the year, they have provided me the right tools for understanding and completion of my thesis. A special appreciation to both of my professors is in order since they have both greatly motivated me during my master thesis work. Boris Balakin has helped me with his outstanding knowledge theoretically and with the simulation software Star-CCM+. Pawel Kosinski has motivated me both before and during my master thesis work, always had an open door policy and provided me with continuously evaluation of my thesis during this year.

Further, I would like to thank my fellow students for the feeling of companionship in stressful times as well as a friendly and productive working environment. A special gratitude to Kristine Gangsøy who has provided both knowledge, motivation and a whole lot of laughter.

In addition, I would like to thank Jean-Michel Herri for providing me with additional info regarding this thesis.

I would also like to thank my family for the unconditional support through my years at the University of Bergen. Last but not least, I want to express my sincere gratitude to Silja Lohne for always believing in me, as well as supporting me through thick and thin.

Bergen, June 2018

Claus Mevik

Abstract

Gas hydrates are solid crystalline compounds that contain water and gas molecules, and can be considered to be a natural occurring phenomena located in enormous amounts around the world. Particle growth and agglomeration of gas hydrates that leads to plugging of a pipeline can delay production significantly and even damage equipment. The increase in use of enhanced oil recovery (EOR) techniques causes more water to be produced. Therefore, research on a high water cut system contributes to understanding plugging formation mechanisms.

This thesis presents two numerical experiments using computational fluid dynamics (CFD), which are conducted with a three-dimensional Eulerian-Eulerian approach using the simulation software Star-CCM+. In addition, mesh independence and validation of the simulations were also performed. The main objectives of the numerical experiments were to: determine and interpret the particle size distribution (PSD) of hydrate particles in a tank with different stirring rates caused by an impeller using a 5-phase CFD model, study particle growth and hydrate formation using a 2-phase CFD-PBM model, and do an analytical analysis of particle diameter size with different stirring rates using various methods. The reasearch was inspired by the work of Herri et al.[1], where they found an increasing particle diameter size with the stirring rate.

The analytical analysis revealed that almost all methods used resulted in too large values of particle diameter. However, a trend of decreasing particle diameter size with stirring rate could be seen. Furthermore, the exception was the method using an implicit relation developed by Zerpa et al. [2], which was in coherence with the values from Herri et al. [1], and showed a decreasing particle diameter size with stirring rate.

The result of the numerical simulations using a 2-phase CFD-PBM model, showed that particle growth and particle diameter size increased with lower stirring rate, which are in coherence with the analytical analysis in this thesis. A possible explanation could be at a lower stirring rate, more particles gather in the top area of the tank, where both concentration of methane and growth rate are largest at this point. Therefore, particles may grow bigger around the top boundary of the tank. This reveals an opposite trend compared to the simulation model done by Herri et al. [1], and the results from the 2-phase CFD-PBM model do not appear to be in qualitative agreement.

A concept of a "bell" shaped curve for the mean particle diameter from the numerical simulations using a 5-phase CFD model was developed. At low shear and stirring rate, hydrates stay at the water-gas interphase due to buoyancy. Increased stirring rate, cause the largest particles to be transported up to the measurement location used in the model, where the particle diameter grow. However, if the stirring rate is increased further, the particle diameter is reduced again due to the slurry becoming homogeneous.

Contents

List of Figures

List of Tables

Nomenclature

Abbreviations

CFD	Computational Fluid Dynamics
CSM	Colorado School of Mines
CSMHyK	Transient gas hydrate model
DEM	Discrete Element Method
E-E	Eulerian-Eulerian
E-L	Eulerian-Lagrangian
FD	Finite Difference
FE	Finite Element
FV	Finite Volume
HEN	Heterogeneous Nucleation
HON	Homogeneous Nucleation
PBM	Population Balance Model
PSD	Particle Size Distribution
TKE	Turbulence Kinetic Energy

Greek

ϵ	Turbulent dissipation rate	[$\mathrm{m}^2/\mathrm{s}^3$]
γ	Interfacial tension	[J/m^2]
γ	Shear rate	[s^{-1}]
κ	Turbulent kinetic energy	[$\mathrm{m}^2/\mathrm{s}^2$]
λ	Molecular free path	
μ	Dynamic viscosity	[$\mathrm{Pa} \cdot \mathrm{s}$]

μ_a	Apparent viscosity of the suspension	$[\mathrm{Pa} \cdot \mathrm{s}]$
μ_o	Liquid phase viscosity	$[\mathrm{Pa} \cdot \mathrm{s}]$
μ_r	Ratio of μ_a and μ_o	
ν	Kinematic viscosity	$[\mathrm{m}^2/\mathrm{s}]$
ν_m	Molar volume	$[\mathrm{m}^3/\mathrm{mol}]$
ω	Angular velocity	[rad/s]
ϕ	Volume fraction	
ϕ_e	Effective volume fraction of hydrate agglomerates	
ϕ_{hyd}	Volume fraction of the hydrate phase	
ϕ_{max}	Maximum packing fraction of hydrates	
ρ	Density	$[\mathrm{kg}/\mathrm{m}^3]$
τ	Shear stress	[Pa]
${\rho_N}^H$	Molecular density	$[\mathrm{mole}/\mathrm{m}^3]$

Roman

$\bar{d}$	Average particle diameter size	[m]
ΔG	Total excess Gibbs free energy	[J]
Δg^{exp}	Experimental molar Gibbs free energy	[J]
Δg^{pd}	Molar Gibbs free energy for products	[J]
$\Delta G^{phase\,trans.}$	Change in Gibbs free energy for phase transition	[J/mole]
Δg^{rx}	Molar Gibbs free energy for reactants	[J]
$\Delta G_{crit.}$	Critical Gibbs free energy	[J]
$\vec{C}_D$	Drag coefficient	
$\vec{F}$	Force	[N]

$\vec{M}$	Drag force	[N/m^3]
$\vec{n}$	Unit normal vector	
$\vec{v}$	Velocity	[m/s]
A	Hamaker constant	[J]
a	Acceleration	[m/s^2]
a_l	Mass-transfer surface area per volume of liquid	[m^{-1}]
B'	Birth kernel	
C	Concentration	[mol/m^3]
C_b	Bulk concentration	[mol/m^3]
C_c	Cunningham correction factor	
C_μ	Turbulence model parameter	
C_{CH4}	Concentration of methane	[mol/m^3]
C_{eq}	Equilibrium concentration	[mol/m^3]
C_{ext}	Interfacial concentration imposed by gas/liquid equilibrium	[mol/m^3]
$C_{i,j}$	Coefficient for the particle-particle interaction	
D	Diffusion constant	[m^2/s]
d	Diameter	[m]
D'	Death kernel	
d_0	Primary particle size	[m]
d_a	Agglomerate diameter	[m]
d_f	Fractal dimension of the agglomerate	
D_p	Particle diameter	[m]
D_s	Stirrer diameter	[m]

D_v	Diffusivity constant	[m^2/s]
$d_{a,max}$	Maximum agglomerate diameter	
D_{eq}	Equilibrium agglomerate diameter	[m]
E	Energy	[J]
e	Specific energy	[J]
E_p	Energy potential	[J]
F_a	Adhesion force	[J/m]
G	Growth rate	[m/s]
h	Mean free path	[m]
h	Surface roughness	[]
I	Turbulence intensity	
J	Flux	[mol/m^{2}s]
K	Turbulent kinetic energy	[J/kg]
k_B	Boltzmann constant	[J/K]
k_d	Growth rate constant	
k_f	Thermal conductivity coefficient of the base fluid	[W/m $\cdot$ K]
k_L	Mass transfer coefficient	[m/s]
$k_L a_l$	Methane absorption	[s^{-1}]
L	Turbulent length scale	[m]
l	Turbulent length scale	[m]
m	Mass	[kg]
M_j	jth-order moment of the population density function	
N	Number density	[1/m^3]

n	Number of particles	
N_p	Power number of stirring device	
N_T	Total number of total particles per unit volume	[Number/mm^3]
N_{rate}	Stirring rate	[1/s]
p	Pressure	[Pa]
Q_t	External source/sink of the flow energy	[W=J $\cdot$ s^{-1}]
q_v	Volumetric heat generation	[W/m^3]
$q_{interphase}$	Interphase heat transfer rate	[W]
R	Particle radius	[m]
r	Dissolution rate	[mol/m^3·s]
R_0	Non-agglomerated primary particles radius	[m]
r_c	Crystal radius	[m]
$r_{crit.}$	Critical crystal radius	[m]
R_{eq}	Mean equilibrium particle radius	[m]
Re	Reynolds number	
Re_p	Reynolds number for the particle	
Re_r	Relative reynolds number	
Sc	Schmidt number	
Sh	Sherwoood number	
t	Time	[s]
u	Turbulent velocity scale	[m/s]
V	Volume of stirred medium	[m^3]
v	Initial velocity	[m/s]

v_{rel}	Mean relative velocity in the collision surface	[m]
w	Mass fraction	
z	Separation distance	[m]
$\bar{C}_{CH4}$	Average concentration of methane	[mol/m^3]
Å	Ångstrøms	[m]

1 Introduction and motivation

The interest for natural gas hydrates has increased significantly the past decades due to the vast amount of stored energy mainly found in ocean sediments. Gas resources from natural gas hydrates in the world are estimated to be around 10^{13} m^3, which is double the conventional fossil fuels discovered today. Natural gas hydrate fields can be found across the globe, mainly at the continental margins with water depths that exceed 300-500 metres. However, gas hydrate fields can be found onshore as well, which is limited to the permafrost regions that has a cold temperature from shallow to enourmous depths [3].

Natural gas hydrates are made up of solid water structures with a gas compound trapped inside. These water molecules act as hosts, and create a cage through hydrogen bonding, while the gas compound, or guest molecule, acts as a stabilizing agent that upholds the cage. A large pressure and low temperature is needed for natural gas hydrates to form, and there are several types of guest molecules like ethane, propane, carbon dioxide. However, methane is the most abundant guest molecule found in the world today [4].

Gas hydrates can also develop into a problem in the petroleum industry. In the case of transporting natural gas, water and/or oil, gas hydrates can start to grow and agglomerate leading to plugging the pipeline. This can delay the production or even damage valuable process equipment. For instance, the use of thermodynamic inhibitors is expensive and requires vast amounts for injection when a oil/gas field is mature. A lot of research has been done on low water cut systems, but as more enhanced oil recovery (EOR) techniques are applied to reservoir fields, more water is produced. Therefore, for a high water cut system, development of a new procedure handling hydrate strategies is limited by the understanding of hydrate plug formation mechanisms.

The topic of this thesis is the investigation of chemical particle growth and particle dispersion of a hydrate-water system in an agitated tank for different stirring rates. Simulations based on the work of Herri et al. [1] was performed, as well as an analytical analysis of particle size development using various methods. Understanding the process of formation and distribution of gas hydrates in a high water cut system can give crucial knowledge for advancement of gas hydrates as an energy resource as well as understanding the mechanisms regarding pipeline plugging.

Objective

The objective of this thesis was the investigation of two different mechanisms that determine the granulometry of a liquid-slurry flow. First, the aim was to describe the particle dispersion in a 5-phase CFD model, which consists of five dispersed hydrate phases in a liquid-solid system, due to turbulent diffusion for different stirring rates. In addition, a 2-phase CFD-PBM model was developed, where hydrate particle growth due to chemical interactions was studied, where the concentration of the methane gas was set to the top boundary of the tank. Furthermore, an analytical analysis using different approaches for particle diameter size investigation was also done. It was also interesting to examine the different parameters in a flow pattern like shear rate γ, turbulent dissipation rate ϵ, y+ values and the turbulent kinetic energy parameters. Nevertheless, mesh independence and validation of the model was studied as well. This was inspired by the work of Herri et al. [1]. The numerical simulations were performed with a three-dimensional Eulerian-Eulerian multiphase model, and are carried out by use of the software Star-CCM+, and ten unique simulations were done.

2 Fundamentals

2.1 Natural Gas Hydrates

Natural gas hydrates has the potential to be an enormous energy source to the world's population. This energy resource is spread across the globe, but restricted to continental margins with water depths that exceeds 300-500 metres. In addition, from shallow to considerable depths and cold temperature, permafrost regions are also an environment natural gas hydrates can occur. For instance, there is a gas hydrate field located in the western Siberian permafrost called Messoyakha. Nevertheless, a gas hydrate production trial using CO_2 / CH_4 exchange led by ConocoPhillips and Japan Oil, Gas and Metals National Corporation took place in Alaska, North Slope. The Ignik Sikumi field experiment was conducted mainly to evaluate the the implications of this hydrate production technique at a field scale. The method was to exchange carbon dioxide molecules for methane molecules within a hydrate structure, releasing the methane for production [5, 6].

According to Kvenvolden [3], an estimation of the amount of gas resource from natural gas hydrates in the world was found to be around 10^{13} m^3. This number is double the amount of conventional fossil fuels discovered today. Natural gas hydrates are made up of a solid water structure with a gas compound trapped inside. This rigid water structure, which consists of hydrogen bonded water cavities, acts as a host. Meanwhile, the gas compound is a guest molecule, and depending on the type of guest molecule, well defined hydrate structures will form under low temperature and high pressure conditions, which can be seen in figure 1. There are several types of guest molecules, such as methane, propane, carbon dioxide and ethane.

Van der Waals forces that act between the guest molecule and cavity make sure that the structure does not collapse. For this reason, the chemical composition and size of the guest molecule is of huge importance on the stability of the hydrate structure. The ratio of cavity to molecular diameter must be favourable for the molecule to fit inside the cavity, but also provides enough stability for the structure. According to Sloan [4], the lower limit size ratio is about 0.76. Below this value, the molecular attractive forces are not strong enough to provide cavity stability. The upper limit size ratio is about 1.0, and above this value, the guest molecule simply cannot fit inside a cavity without distorting the structure.

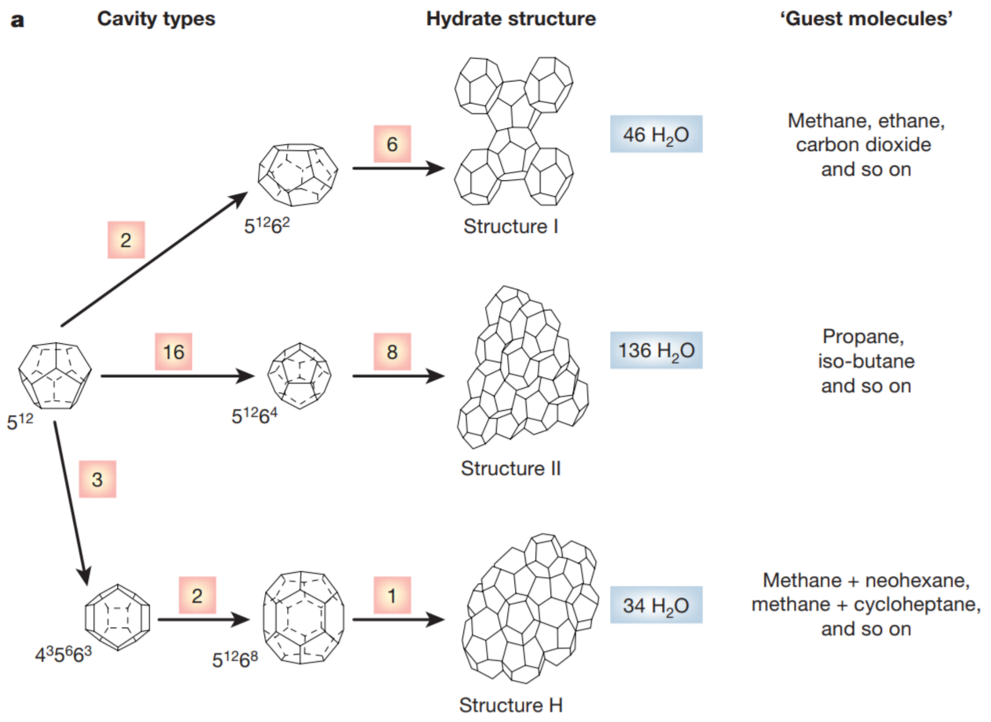

Figure 1: The three common hydrate crystal structures [7].

Gas hydrates can be considered as natural occurring phenomena, which can be labelled as an energy source, but on the other hand hydrates constitute an industry problem [4].

2.1.1 Hydrate structures

There are three types of hydrate structures. The most common types in petroleum industry are the cubic structures I and II. A much less common type is the hexagonal structure H. These structures are classified by the design of the water molecules and the layout of cavities, which are categorized as small, intermediate or large cavities. Since the gas molecules will contribute to keep the structure stabilized, different hydrates will form depending on type of gas compound filling the cavities. Logically, large guest molecules prefer large cavities and vice versa [8].

The hydrate structures are made up of different cages with a different geometry. The dodecahedron is a cage made from a twelve-sided polyhedron where each face is a regular pentagon. Another example is the tetrakaidecahedron, which has a fourteen-sided polyhedron with two hexagonal faces and twelve pentagonal faces. The latter is known as a large cage, while the former is known as a small cage. There is also a large cage with a 16-sided polyhedron called hexakaidecahedron, which consists of twelve pentagonal faces and four hexagonal faces. An overview of the different polyhedrons are showed in figure 2 [8].

These structures are made up of five polyhedra, which again are organized with a specific description method n_i^{mi}. The parameter n_i is the number of edges in face type "i", and mi is the number of faces with edges n_i. Therefore, the twelve-sided pentagonal dodecahedron is then classified as 5^{12} since it has twelve pentagonal faces with equal angles and edge lengths. Because of its twelve pentagonal- and two hexagonal faces, the 14-sided cavity tetrakaidecahedron is denoted $5^{12}6^4$ [4].

Hydrate structure I consists of six small dodecahedron and two large tetrakaidecahedron cages. There are 46 water molecules per unit cell in this structure. Carbon dioxide CO_2, methane CH_4 and hydrogen sulfide H_2S are all guest molecules that can take up both the large and the small cavities of structure I. Ethane C_2H_6, on the other hand, can only fit in the large cavities. These different kinds of molecules have diameters in the range of 4.2 and 6 Å [4].

Hydrate structure II differs from structure I by its complexity. In this case, its structure can be distinguished by a dodecahedron and a hexakaidecahedron. The latter is a sixteen-sided polyhedron with four hexagonal faces and twelve pentagonal faces. There are 136 water molecules per unit cell in this structure.

Structure II is dominated by gas compounds like isobutane C_4H_{10}, nitrogen N_2 and propane C_3H_8. Nitrogen can fit both the small and large cages, whilst propane and isobutane can only fit in the large cages. Nitrogen will form as a single guest with a diameter below 4.2 Å in the small cages. The larger molecules have a diameter between 6 and 7 Å [4].

The type H structures are more uncommon compared to structures I and II. There are three types of cages that make up this hydrate type. First, there is the previously mentioned dodecahedron that consists of a 12 sided polyhedron where each face is a regular pentagon. Second, it is an irregular dodecahedron with three square faces, six pentagonal faces, and three

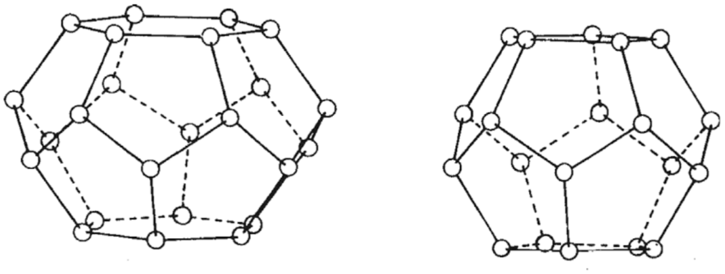

Tetrakaidecahedron
14-sided polyhedron
(large cage)

Dodecahedron
12-sided polyhedron
(small cage)

TYPE I HYDRATE

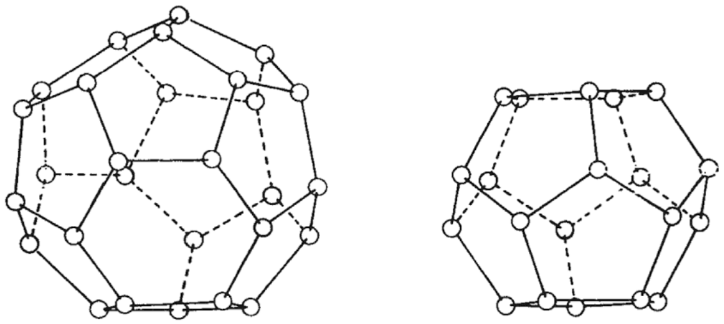

Hexakaidecahedron
16-sided polyhedron
(large cage)

Dodecahedron
12-sided polyhedron
(small cage)

TYPE II HYDRATE

Figure 2: Structure I and II polyhedral cages [8].

hexagonal faces. Lastly, an irregular icosahedron, which is a 20-sided polyhedron, with 12 pentagonal faces and eight hexagonal faces. The crystal itself is made up three small- two medium- and one large cage. A smaller molecule like methane will occupy either the small or medium cage, while larger molecules like methylbutane or cyclohexane will take up the large cage [8].

2.1.2 Gas hydrate formation and growth

Gas hydrate formation conditions include a high pressure and low temperature, which is illustrated in figure 3. Formation of gas hydrates mostly develop on the water-gas interface since the concentration of the hydrate component exceeds the mutual fluid solubility [7].

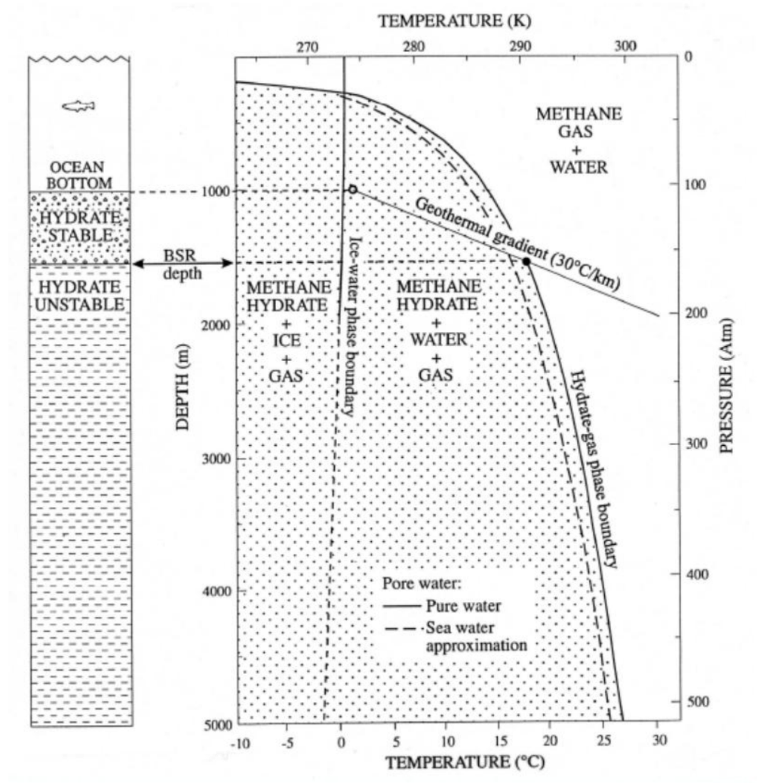

Figure 3: Hydrate stability zone [9].

Formation of gas hydrates can be separated into stages like nucleation, induction time and growth. Hydrate nucleation is the process where a tiny batch of hydrate nuclei, which consists of gas and water molecules, tries to attain critical size for continued growth. This stage can be seen in the left bottom corner in figure 4. The nucleation period takes place in the microscopic scale containing tens to thousands of molecules, therefore this stage is challenging to be observed experimentally. Two concepts of nucleation are heterogeneous nucleation (HEN) and homogeneous nucleation (HON). HON is a process that involves large numbers of molecules that collide simultaneously. As a result, clusters may increase in sequences until the critical size is reached. In addition, this process is free of impurities. Kvamme [10] suggested that the nucleation process could be explained by the minimization of Gibbs free energy. Equation (1) illustrates a competition between the surface excess free energy and the volume excess free energy, and can be expressed by:

$$\Delta G = \Delta G^{surface} + \Delta G^{phase\,trans.} = 4\pi r_c^2\gamma + \frac{4}{3}\pi r_c^3 {\rho_N}^H \Delta G^{phase\,trans.} \leq 0, \quad (1)$$

where ΔG is the total excess Gibbs free energy, γ is the interfacial tension, r_c is the crystal radius, ${\rho_N}^H$ is the molecular density, and $\Delta G^{phase\,trans.}$ is the intensive change in Gibbs free energy related to the phase transition. The critical size may be obtained and growth can occur if the change of Gibbs free energy related to the phase transition can overcome the penalty from creating new surface area. The critical Gibbs free energy can be obtained if equation (1) is modified and by setting the outcome to zero, the expression becomes:

$$\Delta G_{crit.} = \frac{4\pi r_{crit.}^2}{3}, \quad (2)$$

where $\Delta G_{crit.}$ is the critical Gibbs free energy, which is the the energy that must be overcome to reach critical size. The critical crystal size $r_{crit.}$, is the minimum size needed for the hydrate crystal to develop and grow.

HON is less likely to occur in real life situations since a solution is seldom free of impurities. HEN is then a more likely nucleation process, which take a foreign body into account. Because of this, the contact angle between the surface of the foreign body and the hydrate crystal has to be addressed.

Furthermore, equation (2) can be adjusted to:

$$\Delta G'_{crit.} = \phi \Delta G_{crit.}, \tag{3}$$

where ϕ is the volume fraction related to the contact angle. This results in a lower value of critical Gibbs free energy for HEN to be smaller or equal to HON. Therefore, HEN is more feasible to take place in nature [11] [10]. There are several different hypotheses on nucleation and these phenomena are in focus in the scientific environment.

The induction time is defined as the time passed until the presence of hydrate phase can be detected on a macroscopic scale. During this time both pressure and temperature are within hydrate formation conditions. However, during the induction time, gas hydrates is less likely to form because of metastability.

The next step is called the growth period, where swift hydrate growth develops. This happens when the critical size for the hydrate nuclei is achieved and result in growth of hydrates. According to Englezos et al. [12], the growth stage is governed by hydrate kinetics coupled with heat and mass transfer. The hydrate cages are occupied and concentrated by the gas, but the growth rate is dependent of the amount of water and gas molecules present. As figure 4 shows, the slope of gas consumption swiftly increases in the beginning, but decreases with time due to water consumption during hydrate formation [11]. The reason is the initial high availability of both phases that results in a steady, swift growth, but in time the reduction in either gas or water cause the growth rate to decrease and eventually comes to a halt.

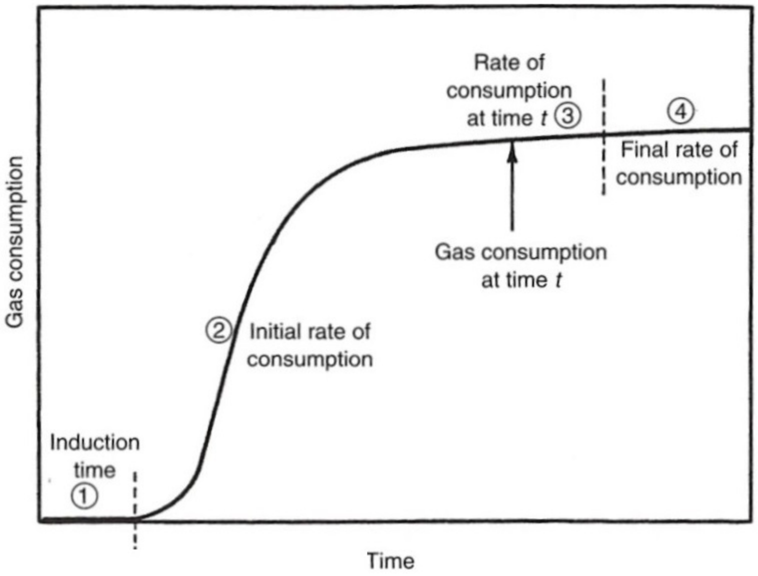

Figure 4: Gas consumption as a function of time for hydrate formation [11].

2.1.3 Nucleation driving forces

To understand the hydrate formation process, the nucleation driving force must be studied. According to Sloan [11], a general driving force for the nucleation process can be expressed by:

$$\Delta g^{exp} = \Delta g^{rx} - \Delta g^{pd}, \tag{4}$$

where Δg^{exp} is the experimental molar Gibbs free energy, Δg^{rx} and Δg^{pd} is the molar Gibbs free energy of the reactants and products, respectively. Figure 5 illustrates hydrate formation as a function of temperature (subcooling). The AB curve represents the equilibrium, while CD the supersaturation curve. By moving into the metastable region at point Q, the driving force is increased relative to point P, and nucleation may or may not take place. The driving force is considerably increased to the left of the CD curve, therefore it is likely hydrate nucleation takes place.

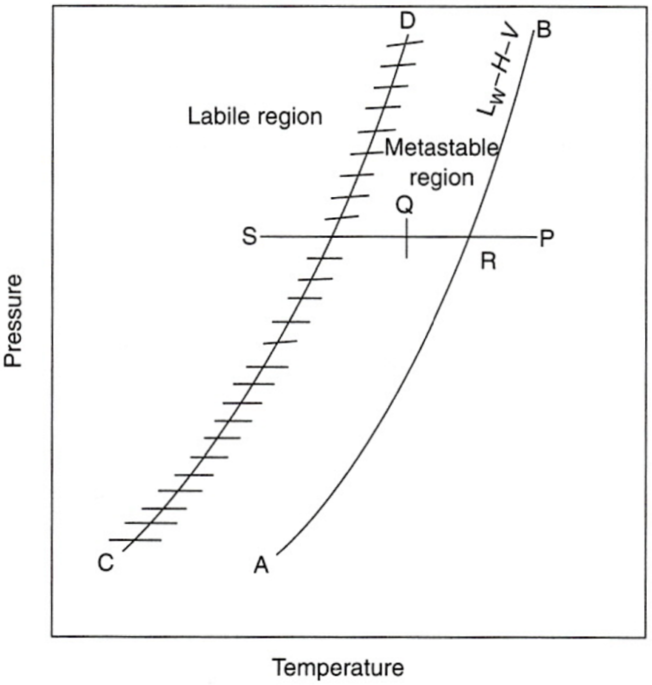

Figure 5: Hydrate formation as a function of subcooling. The equilibrium line AB and supersaturation line CD are shown [4].

2.1.4 Gas hydrates and problems in the industry

As figure 6 shows, in the case of transporting natural gas, water condensation can occur on the pipeline walls so that the flow becomes a liquid-gas system. Therefore, gas hydrates can start to grow. After some time they will agglomerate and then finally create an obstruction called a plug. Figure 8 shows a gas hydrate plug formed in an oil pipeline [4]. This will delay the production significantly and can even damage the equipment. Thermodynamic inhibitors, like alcohol or glycerol, may be introduced to change the chemical potential, which hinders the system from entering the thermodynamically stable conditions for hydrate formation. It will ultimately modify the hydrate stability zone, and shift the hydrate equilibrium conditions to higher pressures and/or lower temperature [13, 14].

Since the use of thermodynamic inhibitors is expensive and requires vast amounts for injection when a oil/gas field is mature, a certain low dosage

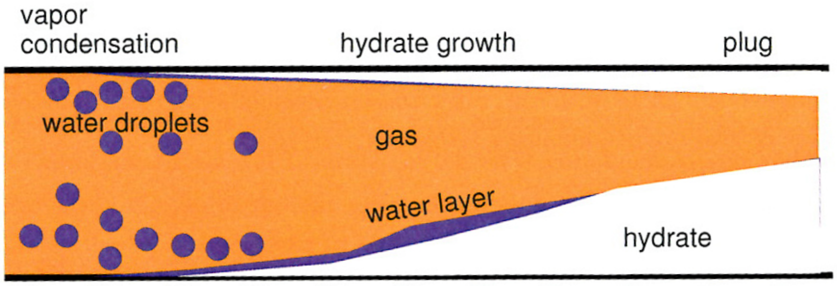

Figure 6: Gas hydrate propagation in a pipeline transporting gas [13].

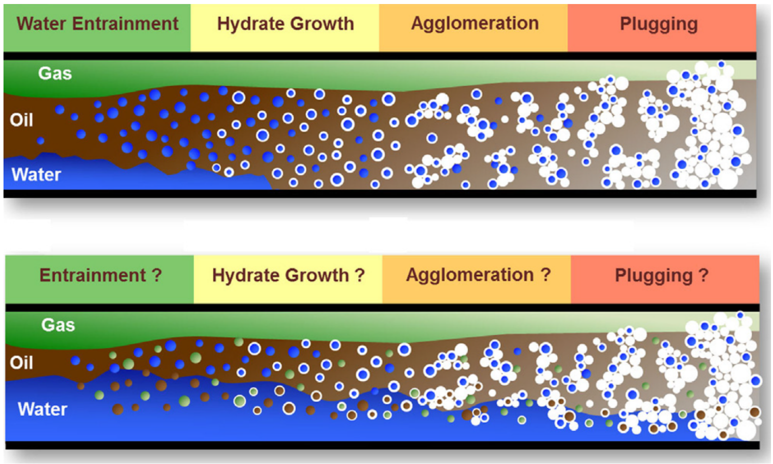

Figure 7: Illustration of a hydrate formation and plugging mechanism in a low (top) and high (bottom) water cut system [14].

hydrate inhibitors were also developed and used. These delay the hydrate growth, or so called nucleation, i.e. preventing hydrate plugging at a much more inexpensive way. Since the oil and gas fields mature, the need for oil recovery increases, while the amount of water produced is then also increased. Therefore, the risk of pipeline plugging escalates as well. For a low water cut system, scientists know fairly well what physical processes that occur. On the other hand, for a high water cut system, development of a new procedure handling hydrate strategies is limited by the understanding of hydrate plug formation mechanisms. This illustrated in figure 7 [14].

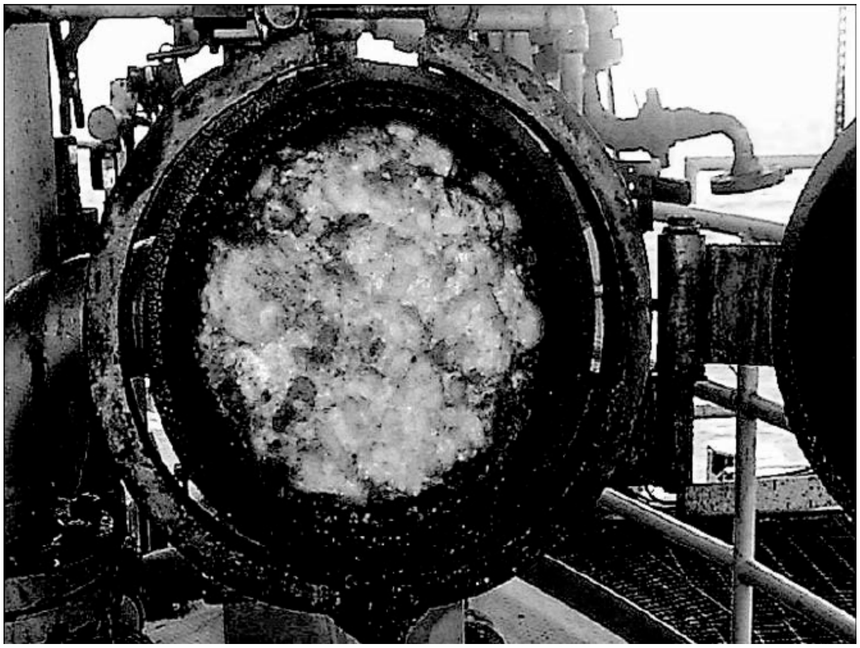

Figure 8: A gas hydrate plug formed in an oil pipeline [4].

2.2 CFD

CFD is a research tool applied to carry out numerical analysis to solve mathematical equations regarding fluid flows. CFD is a sub-category of fluid dynamics which has many diverse engineering applications.

All types of fluid are driven by three fundamental physical principles: mass is conserved and energy is conserved, and Newton's second law follows from these principles. Basic mathematical equations can express these principles and are either on partial differential or integral form. The goal is to produce values of flow field main parameters at discrete points in time and/or space by discretisize these equations into algebraic forms. The end product of this research tool is a collection of numbers. Both regular- and supercomputers enable the posibillity to do thousands of calculations and solve simple- or very complex CFD problems [15].

To achieve the basic equations for fluid flow, the following procedure is always followed:

1. The appropriate physical principles must be chosen:

   (a) Mass is conserved
   (b) $\vec{F} = m\vec{a}$ (Newton's second law)
   (c) Energy is conserved

2. Apply these physical principles to a suitable model of the flow

3. The last step is to extract the mathematical equations from this application. These equations must express the physical principles.

Development of technology and fluid dynamics have benefited tremendously from the advancement of this computational approach. Aeronautics, automobile and engine applications, industrial manufacturing, naval architecture to name a few have use of some sort of CFD modeling, and it will continue to play a major role in the future [15].

2.2.1 Models of the flow

The physical principles need to be applied to a suitable model of flow. For a general flow there are four different models. Figure 9 illustrates a control volume V, control surface S and streamlines, which represent the flow. There are four models of flow: a finite control volume fixed in space with fluid moving through it, a finite control volume moving with the fluid, an infinitesimal fluid element fixed in space and an infinitesimal fluid element moving along a streamline [15].

Applying physical principles to a model would generate a set of flow-equations in a specific form. The flow-equations would be in integral form for a finite control volume and could be transformed to partial differential form at a later stage. The integral, or the partial differential form, in a fixed control volume in space provides equations called conservation form. On the other hand, a control volume that moves in space would give equations, either in integral- or partial differential form, called the non-conservation form [15].

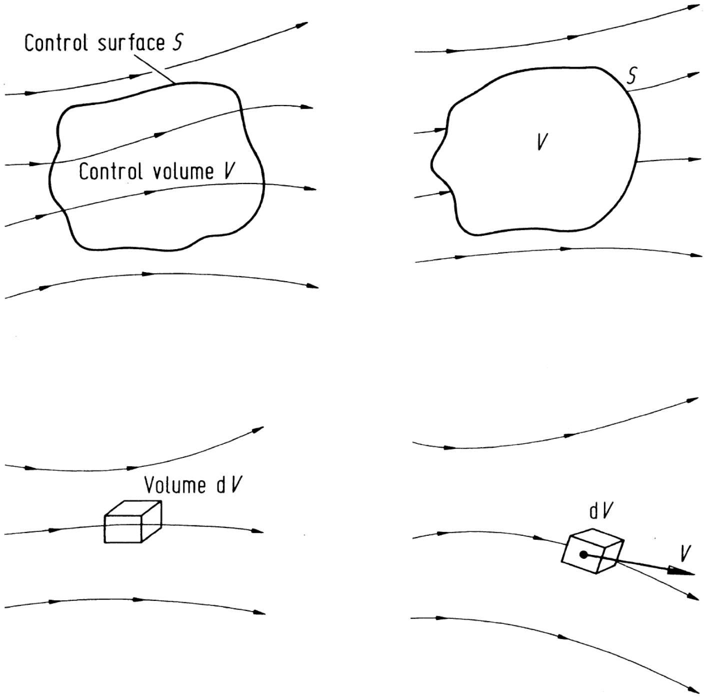

Figure 9: a) Finite control volume fixed in space with fluid moving through it, b) Finite control volume moving with the fluid such that the same fluid particles are always in the same control volume, c) Infinitesimal fluid element fixed in space with the fluid moving through it, d) Infinitesimal fluid element moving along a streamline with the velocity $\vec{v}$ [15].

2.2.2 Continuity equation

The fundamental physical principle known as mass is conserved can be expressed as:

Net mass flow out of control volume through surface S = time rate of decrease of mass inside control volume

or

Rate of mass flow in - rate of mass flow out = rate of mass accumulation

$$\frac{\partial \rho}{\partial t} + \nabla \cdot (\rho \vec{v}) = 0. \tag{5}$$

Equation (5) is a partial differential equation in conservation form. The continuity equation will form regardless of which model of flow used when applying this physical principle [15].

2.2.3 Momentum equation

The momentum equation [15] is based on the physical principle Newton's second law. Any of the four models of the flow can be used to apply this physical principle, but it is favourable to use the moving infinitesimal fluid element model shown as d) in figure 9 for both the momentum- and the energy equation:

$$\rho \frac{Du}{Dt} = -\frac{\partial p}{\partial x} + \frac{\partial \tau_{xx}}{\partial x} + \frac{\partial \tau_{yx}}{\partial y} + \frac{\partial \tau_{zx}}{\partial z} + \rho f_x. \tag{6}$$

Equation (6) is for the x component of the momentum equation for a viscous flow. There are similar expressions for the y- and z components. These are all scalar equations in non-conservative form and called the Navier-Stokes equations.

2.2.4 Energy Equation

The physical principle to be applied to a model of flow is that energy is conserved, which is essentially the first law of thermodynamics. When applied to the moving fluid element moving along a streamline the first law express that:

Rate of change of energy inside fluid element = Net flux of heat into element + Rate of work done on element due to body and surface forces

$$\frac{\partial(\rho_c E)}{\partial t} + \frac{\partial(\rho_c E u_i)}{\partial x_i} = \frac{\partial(\tau_{ij} u_i)}{\partial x_i} - Q_t, \tag{7}$$

where Q_t is the external source/sink of the flow energy and E is the total energy [15].

2.2.5 Boundary conditions

A flow field over a helicopter and a sports car share the same governing equations. What makes them different are the boundary- and initial conditions. These conditions will provide solutions to the governing equations and this will make up the distinct flow field for a certain geometry. Boundary conditions therefore have specific and an important role in CFD. This is critical for obtaining the solution to the governing flow equations [15].

For a viscous flow, the physical boundary condition on a certain surface assumes zero relative velocity between the gas and the surface. This is called a no-slip condition. If the surface is stationary with the flow moving past it at the same time, then:

$$u = v = w = 0. \tag{8}$$

There is also a "no-slip" condition regarding the temperature at the surface. This boundary condition is:

$$T = T_w, \tag{9}$$

where T_w is the temperature at the wall, and therefore also the temperature of the fluid layer directly in contact with the wall, and T is the gas temperature.

The flow velocity at the surface is a non-zero, finite value for an inviscid flow. Since there is no friction the flow cannot attach to the surface. The wall boundary is given by:

$$\vec{v} \cdot \vec{n} = 0, \tag{10}$$

where $\vec{n}$ is a normal unit vector at a point at the surface and $\vec{v}$ is the velocity vector. For a solid wall, the velocity vector $\vec{v}$ is tangent to the wall [15].

2.2.6 Discretization

Discretization is a process of replacing the continuous domain with a discrete domain that consists of N points using a grid. Mathematical expressions such as integral or differential problems are viewed as having an infinite number of values in the domain. These values are then handled with different discretization techniques providing a finite number of discrete points in the domain. The goal for discretization is to make the equations suitable for

for numerical calculations and get a discrete number from the governing equations in the computational domain [15].

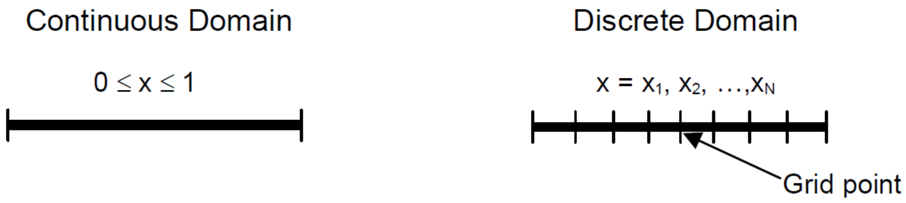

Figure 10: Continuous domain and a discrete domain[15].

Figure 10 shows only a simple view of the discrete domain, but this can be expanded into a more detailed description of the grid. Figure 11 displays the grid in the xy-plane with spacing Δx and Δy, which are very often uniform. Nevertheless, it is not mandatory for Δx or Δy to be uniform. As figure 11 shows, the grid points can be identified by index i in the x-direction, and index j in the y-direction [15].

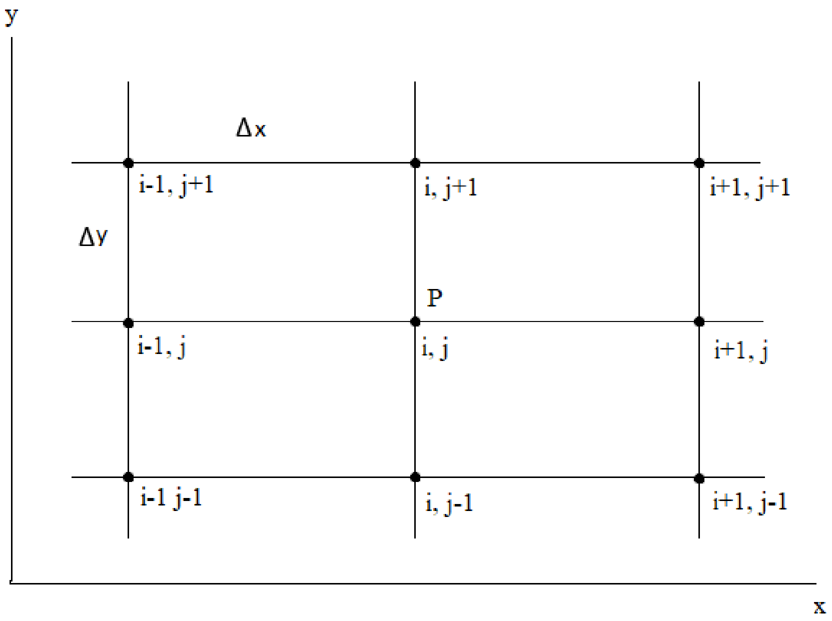

Figure 11: Discrete grid points. Redrawn from Anderson et al. [15].

There are two common discretization techniques called the method of finite difference (FD) and finite volume (FV). A two-dimensional flow field governed by the Navier-Stokes equations are called partial differential equations. A solution to these would bring expressions for velocity, density, pressure etc. as function of x and y for every point in the flow we choose. However, if the partial differential equations are replaced by algebraic difference quotients, where they are asserted in terms of the flow-field variables at two or more of the discrete grid points. These equations are then replaced by a system of algebraic equations. These can be solved for the flow-field variables at the discrete grid points [15].

The method of finite volume (FV) follows almost the same procedure as the FD method: the main difference is the use of integral form of the equations, instead of the partial differential form. This is obtained by using the divergence theorem. It is then possible, as for the FD method, to represent the equations in the form of algebraic equations. Furthermore, the domain is divided into cells. This method is also used in a wide variety of CFD problems [16, 15].

3 Multiphase modeling

When investigating particle growth and size distribution, it is of huge importance to understand the concept of modelling the multiphase flow. A multiphase flow is defined as a system with two phases or more, like liquid, gas or solid, that exists at the same time. These phases can have either a single- or a multicomponent of various chemical species. It is common to distinguish between four subcategories of a multiphase flow: gas-liquid, gas-solid, liquid-solid and three phase flows.

Both a two-phase and a six-phase model have been studied in this thesis, more precisely liquid-solid flows. The solid particles make up the dispersed phase while the liquid is the continuous phase, and the solid particles get carried by the liquid. Water is in the liquid phase and gas hydrates are in solid form, which represent the dispersed phase. This particular flow is often called a slurry-flow.

3.1 Eulerian-Eulerian and Eulerian-Lagrangian multiphase modelling

The Eulerian-Eulerian (E-E) multiphase model was selected for this thesis to be the main approach for handling the simulations. Due to the large number of dispersed phases included in one of the simulation models, the E-E approach was considered to be the best choice regarding computational efficiency. The Eulerian-Lagrange approach could possibly become too complex for this case.

The main difference between these two approaches, is the treatment of the dispersed phase. In the E-E approach both the particles and fluid are treated as a continuum and the corresponding equations are solved for both phases. This allows solving the Navier-Stokes equations for each phase, as well as momentum, enthalpy and continuity equations. Because of its treatment of the dispersed phase, this approach is usually considered to be the most computationally efficient, as previously mentioned. It also covers the full range of volume fraction from 0 to 1, and it is capable to obtain mean quantities directly without any post-processing of the results. This model is however, most applicable for a dense flow rather than a dilute flow. Particle-wall, particle-particle interactions cannot be expressed directly, and modelling size distribution of each particle is complex. Convergence could be challenging because of strong couplings of each phase [17].

In the Eulerian-Lagrangian approach, the Navier-Stokes equations are solved for the continuous phase, but the dispersed phase is modelled as a system of single particles. This leads to a method that solves the equations of motion for the individual particle. If the simulation scenario includes a dense particle cloud, the computational time will be enormous. This is because this approach, regarding the dispersed phase, is very accurate since each particle requires its own set of equations. Unlike the E-E method, the E-L approach is ideal for particle size distribution and detailed modelling of mass transfer between particles and the surrounding fluid. It is also designed for particle-particle collisions and agglomerations. In spite of the advantages, the E-L method is limited to smaller concentration of particles and post-processing of the results are required to compute volume fractions. On the other hand, the E-E method provides volume fractions directly from the solver.

3.2 Governing equations

The Eulerian-Eulerian two phase model was used to describe the flow. The continuity equation can be expressed like:

$$\frac{\partial \phi_i \rho_i}{\partial t} + \nabla \cdot (\phi_i \rho_i \vec{v_i}) = 0, \tag{11}$$

where ϕ is the volume fraction, ρ is density and $\vec{v}$ is the velocity vector. Nevertheless, $i = f$ represent the fluid phase and $i = p$ is the particles. These phases are related by the expression of volume fraction:

$$\sum_i \phi_i = 1 \tag{12}$$

The momentum equation can be written as:

$$\frac{\partial (\phi_i \rho_i \vec{v_i})}{\partial t} + \nabla (\phi_i \rho_i \vec{v_i} \vec{v_i}) = -\phi_i \nabla p + \nabla (\phi_i \mu_i \vec{v_i}) + \phi_i \rho_i g + \vec{M_i}, \tag{13}$$

where p is the static pressure field and μ is dynamic viscosity. The parameter $\vec{M}$ is drag force, and is equal to $\vec{F_D} \cdot n$, where n is the number density. Drag force is further described in section 3.5.

The energy equation is written as:

$$\frac{\partial(\phi_i \rho_i e_i)}{\partial t} + \nabla(\phi_i \rho_i e_i \vec{v_i}) = \nabla(\phi_i k_f \nabla T_i) - q_{interphase,i} + q_{v,i}, \tag{14}$$

where k_f is the thermal conductivity coefficient of the base fluid, e is the specific energy, q_v is the volumetric heat generation, and $q_{interphase}$ is the interphase heat transfer rate.

3.3 Diffusion

Diffusion is the movement, or flow, of matter from a region of high concentration to a region of low concentration. An injection of a gas into a tank filled with liquid will eventually result in diffusion. For this reason, diffusion is known as a transport phenomenon, which is illustrated in figure 12. An example of diffusion using CFD can be seen in figure 14 [18].

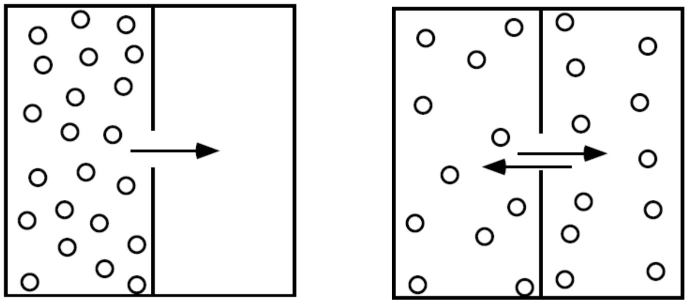

Figure 12: An illustration of diffusion as a transport phenomenon due to existing differences in concentration [18].

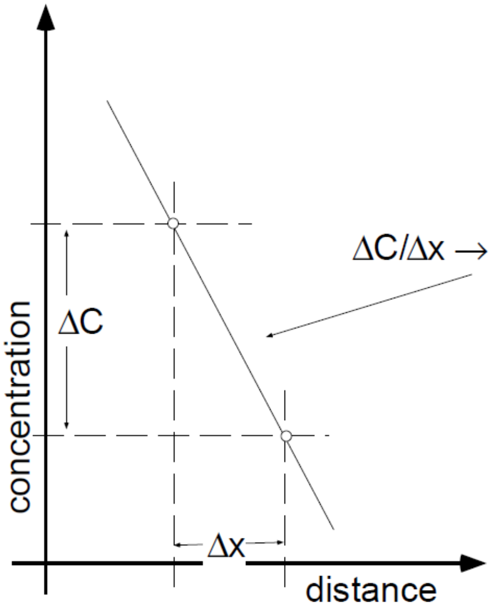

Figure 13: The driving force for diffusion: concentration gradient [18].

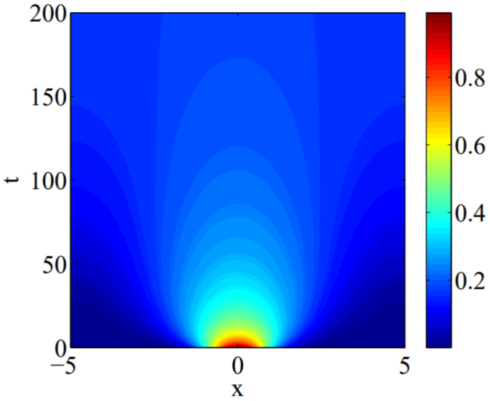

Figure 14: Illustration of diffusion simulated with CFD software [18].

The flux in each diffusion reaction follows the following expression:

Flux = conductivity x driving force,

where in the case of molecular diffusion, conductivity is referred to as the diffusion constant, which has the symbol D. Furthermore, the driving force is the concentration gradient, which is the rate of change of the concentration with distance, and can be seen in figure 13 [18].

There are two types of diffusion processes, steady state and non-steady state diffusion. Steady state diffusion represents a constant number of atoms that is crossing an interface. As can be seen from figure 13, dC/dx = constant and $dC/dt = 0$. Steady state diffusion is based on Fick's first law, and can be expressed as [18]:

$$J = -D\left(\frac{dC}{dx}\right), \tag{15}$$

where J is the flux and C is the concentration. The flux is the amount of substance that will flow through a unit area during a time interval. The negative sign represents the gradient, and the particle flow is from a high concentration region to a low concentration region.

In this thesis, the process of non-steady state diffusion takes place, which is a partial differential equation named Fick's second law [18]:

$$\frac{\partial C}{\partial t} = D\frac{\partial^2 C}{\partial x^2} \tag{16}$$

This is therefore a time dependent process, where the rate of diffusion is a function of time. Hence, dC/dx varies with time, while $dC/dt \neq 0$.

3.4 Particle size distribution

Particle size distribution (PSD) has many usage areas across multiple scientific disciplines, especially powder and industrial crystallization. In this theis, the PSD for a stirred tank containing particles will be studied. Generally, the method of PSD is to gather information about the number of particles present corresponding to size. There are many ways to collect data by measuring the particles in with different methods. Herri et al. [1] built a turbidity sensor, which could obtain in-situ PSD determination of gas hydrate particles, and an illustration can be viewed in figure 43. A useful parameter used in PSD is the size distribution function $N(v)dv$, which represents the number of particles in a unit volume of the multiphase mixture with volume between v and $v + dv$ [19].

3.5 Drag force

Drag force is a force acting opposite to the relative motion of any object moving with respect to the surrounding fluid. This force can be expressed as:

$$\vec{M} = \frac{3}{4}\frac{\vec{C}_D}{C_c}\frac{\phi_d \rho_c}{d_p}|\vec{v_r}\vec{v_r}|, \tag{17}$$

where ϕ_d is the volume fraction of the dispersed phase, ρ_c is the density of the fluid, d_p is the diameter of the particle and $\vec{v_r}$ is the relative slip velocity between phases. The parameter C_D is the drag coefficient, and the Schiller-Naumann method was used in this case [20], which can be expressed as:

$$\vec{C}_D = \frac{24}{Re_p}(1 + 0.15{Re_p}^{0.687}), \tag{18}$$

which is valid for $Re_p \leq 1000$ and is referred as the Stokes flow regime.

In the case of a turbulent flow with values of $Re_p \geq 1000$, the drag coefficient [20] becomes $\vec{C}_D = 0.445$.

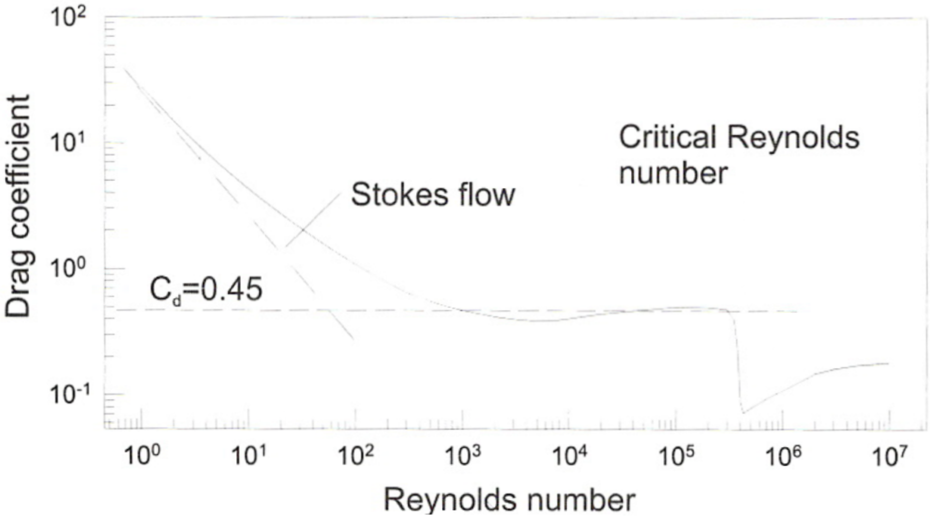

Figure 15: Illustration of the different drag force coefficients of a sphere with Reynolds number [21]

An illustration of the variation of drag coefficients of a sphere with Reynolds number can be viewed in figure 15 [21].

The relative Reynolds number for the particle Re_p [21], is defined in this case as:

$$Re_p = \frac{\rho_c |\vec{v}_r| d_p}{\mu_c} \tag{19}$$

The Cunningham correction factor C_c [20] can be expressed as:

$$C_c = 1 + \frac{2\lambda}{d_p}(1.257 + 0.4e^{\frac{1.1d_p}{2\lambda}}), \tag{20}$$

where λ is the molecular free path:

$$\lambda = \frac{\mu_c}{p}\sqrt{\frac{\pi k_B T_c}{2m}}, \tag{21}$$

where k_B is the Boltzmann constant and m is the mass of the fluid.

3.6 Mass transfer

Mass coupling can occur through evaporation, chemical reactions and condensation. For hydrate particle growth, it is important to understand how methane dissolve into the water from the top of the tank. In this thesis, equations for mass transfer are needed when studying this subject. Change in mass of methane in water follows the relation:

$$\frac{dm}{dt} = \pi Sh D \rho_c D_v (w_{A,\infty} - w_{A,s}), \tag{22}$$

where Sh is the Sherwood number and acts as a constant of proportionality, and is defined as the ratio of the convective mass transfer to the mass diffusivity. In addition, D_v is the diffusivity constant for methane in water. $w_{A,s}$ is the mass fraction of component A in the mixture at the surface of the droplet, while $w_{A,\infty}$ is the mass fraction of A in the free stream [21].

3.7 Phase Coupling

A schematic diagram of coupling effects is shown in figure 16. The dispersed phase is described by temperature, velocity, size and concentration. The carrier phase is characterized by temperature, density, pressure, velocity field as well as concentration of the gas phase. Coupling can take place through momentum, energy and mass transfer between phases. There are two ways of defining phase coupling. If the flow of one phase influences the other without any reverse effect it is said to be one-way coupled. On the other hand, two-way coupling is present if there is an interactive effect between the flows of the phases. Parameters like temperature and velocity can change depending if one- or two-way coupling is present. The different types of parameters represent the importance of coupling [21].

Coupling can occur through mass, momentum, and energy transmission between phases. Because of drag force on the continuous and dispersed phase, momentum coupling is present. However, momentum coupling can also happen due to depletion or addition as a result of mass transfer. Heat transfer between the phases results in energy coupling. Addition of mass through evaporation or depletion of mass due to condensation is responsible for mass coupling. One must determine the parameters magnitude if two- or one-way coupling is required [21].

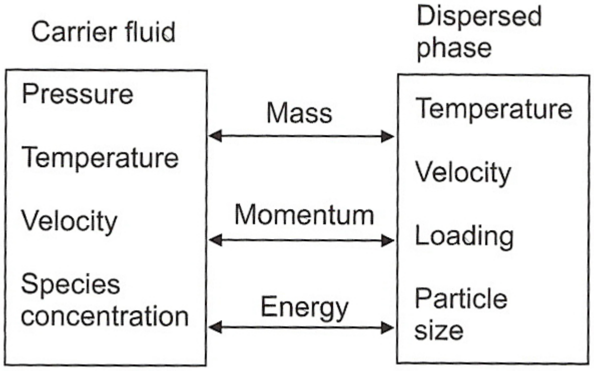

Figure 16: Diagram of coupling effects [21]

Figure 17 shows the example of hot particles injected into cool gas flowing in a pipeline that results in temperature of the particles to decrease. At the same time the velocity of the particles will increase due to the gas velocity. This system is one-way coupled if the particles only affect the gas without the gas altering parameters of the particles. On the other hand, if two-way coupling is present and the particles affect the gas, further parameters would change. The gas temperature would increase and gas density would decrease. To satisfy mass conservation the gas velocity increases as well. Because of the reduction of temperature difference the particles would be accelerated to a higher velocity. The result is a more negative pressure gradient due to the increased gas velocity and particle velocity acceleration [21].

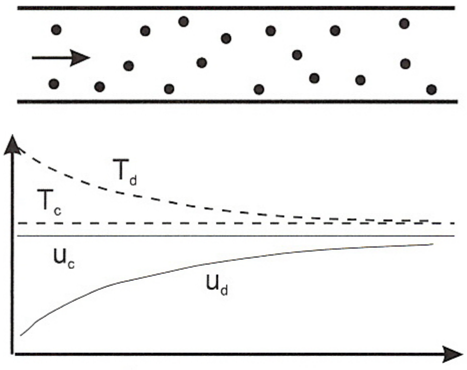

One-way coupling

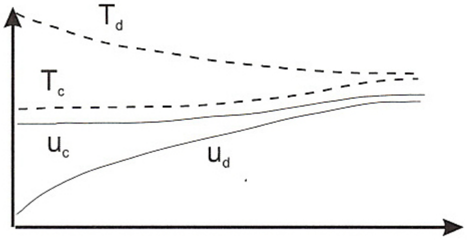

Two-way coupling

Figure 17: Interpretation of one- and two-way coupling for a flow in a pipeline [21].

3.8 Van-der-Waals interactions

Van der Waals forces are intermolecular forces that exist between molecules that are electrically neutral, and include repulsion and attraction between surfaces and molecules. There are three different types of phenomena that make up the van der Waals forces, and they are called dipole-dipole, dipole-induced-dipole and london dispersion force. These are considered to be weak forces, and not as strong as chemical bondings. Nevertheless, van der Waals forces are present in many different scientific fields and are of significance [22, 23].

To describe the van der Waals interactions between macroscopic objects, it is best illustrated with the Lennard-Jones total potential energy between molecules A and B based on the separation between them:

$$E_p\left(total\right) = E_p\left(repulsion\right) + E_p\left(attraction\right) = \frac{B}{r^{12}} - \frac{A}{r^6}. \tag{23}$$

A common way to express the van der Waals pair potential is:

$$w(r) = -\frac{C}{r^6}. \tag{24}$$

In equation (23), A and B are constants for the molecules and r is the separation between the molecules. These attractive and repulsive forces determine the potential energy of the molecules, as it varies as the separation distance changes. If these forces are equal, the equilibrium distance r_0 has been reached for the molecules [24, 23]. Figure 18 illustrates the potential energy as a function the separation distance between the molecules.

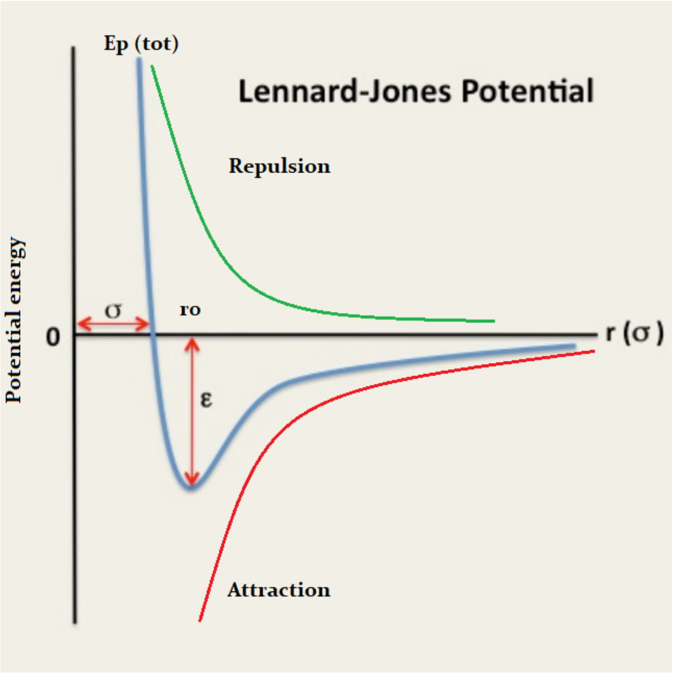

Figure 18: Lennard-Jones potential, which shows the total potential energy as the separation distance r varies between the molecules [22].

The repulsive force corresponds to a positive energy, while the attractive force corresponds to a negative energy. Therefore, the red and green line in figure 18 show how the potential energy of attraction and repulsion changes with separation, respectively. As the molecules move closer together, the attractive forces dominate, making the potential energy more negative. The equilibrium separation r_0 is where the potential energy is at its minimum. Furthermore, if the molecules moves closer together, the repulsive forces will dominate and the potential energy will start to increase and eventually become positive as figure 18 shows.

To successfully measure the magnitude of the van der Waals forces acting on solid bodies, the addition of molecules that make up the surfaces must be studied. Hamaker [21] made several calculations for numerous geometries, where one of them is the force between two infinite flat plates with a certain separation. This is presented in equation (25) where F is the force per unit area between the plates, z as the separation distance and A as the Hamaker constant:

$$F = \frac{A}{6\pi z^3}. \tag{25}$$

As figure 19 shows, Hamaker also calculated the force F between two spheres in contact with separation distance z, and the diameters of the molecules D. This is expressed as:

$$F = \frac{Ad}{12z^2}, \tag{26}$$

where

$$d = \frac{D_1 \cdot D_2}{D_1 + D_2}. \tag{27}$$

The separation distance z is at the contact point.

The general expression for the Hamaker constant A, can be written as:

$$A = \pi^2 \cdot C_{i,j} \cdot \rho_1 \cdot \rho_2, \tag{28}$$

where C is the coefficient for the particle-particle interaction, or the van-der-Waals constant for the molecule pair. Furthermore, ρ_i is the molecular

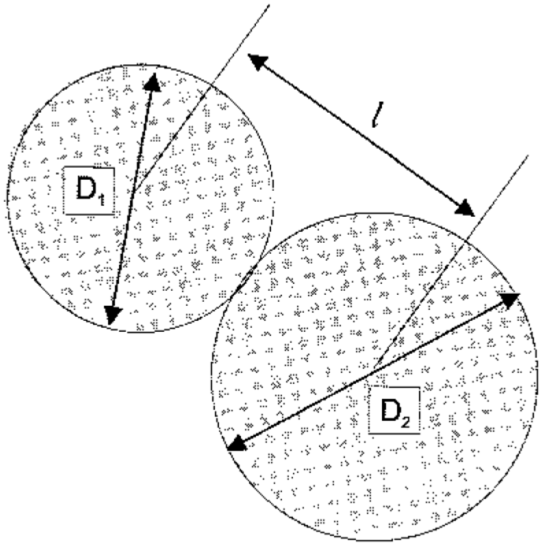

Figure 19: Two sphere particles in contact [21].

density for the interaction particles constituting the body. It is possible to calculate the interaction parameter C from the van der Waals potential, which can be viewed in equation (24).

To calculate an unknown Hamaker constant in terms of known ones, the following relation can be used [25]:

$$A_{ikj} \approx \left(\sqrt{A_{ii}} - \sqrt{A_{kk}}\right)\left(\sqrt{A_{jj}} - \sqrt{A_{kk}}\right), \tag{29}$$

where two components i and j are separated by a medium of component k. When two surfaces of component i are separated by a medium of component k, the expression becomes:

$$A_{iki} \approx \left(\sqrt{A_{ii}} - \sqrt{A_{kk}}\right)^2. \tag{30}$$

Adhesive force can be described as attractive forces between molecules that are different from each other. These forces include mechanical and electrostatic forces. If the force between a liquid and a surface is strong enough, it will pull the water molecules out of their spherical formation and spread them out on the surface making a thin film.

The parameter z is the particle separation distance, and consists of the mean free path for the water molecules. The parameter h [26] and d_{nuclei} is also often called roughness. The surface roughness is related to surface texture, and represent the deviations from the ideal form of the surface. This can be illustrated in figure 20:

$$z = h + 2d_{nuclei} \tag{31}$$

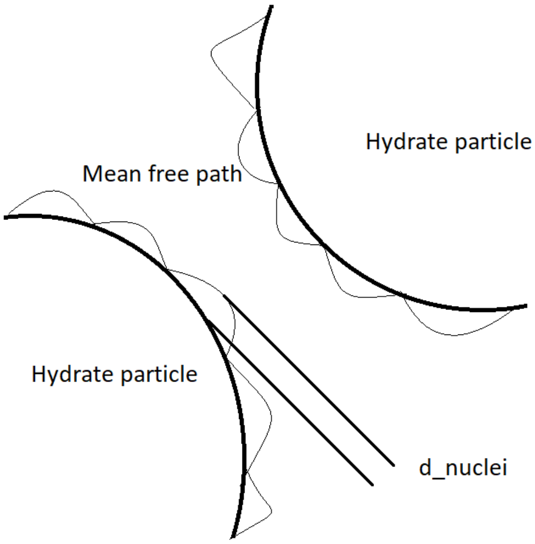

Figure 20: Mean free path of methane hydrate particles, including roughness of a surface.

3.9 Turbulence kinetic energy

In this thesis, it is necessary to calculate the initial conditions for the turbulent kinetic energy equations (TKE). Turbulence is characterized by continuously changing the magnitude and direction of the speed at a point in a flow. This can be illustrated by fluctuations or eddies, and can be viewed in figure 21. TKE represent the mean kinetic energy per unit mass related to eddies in the flow. These equations must be calculated by CFD in order for fluid turbulence to be modelled and obtain an accurate fluid flow prediction [27].

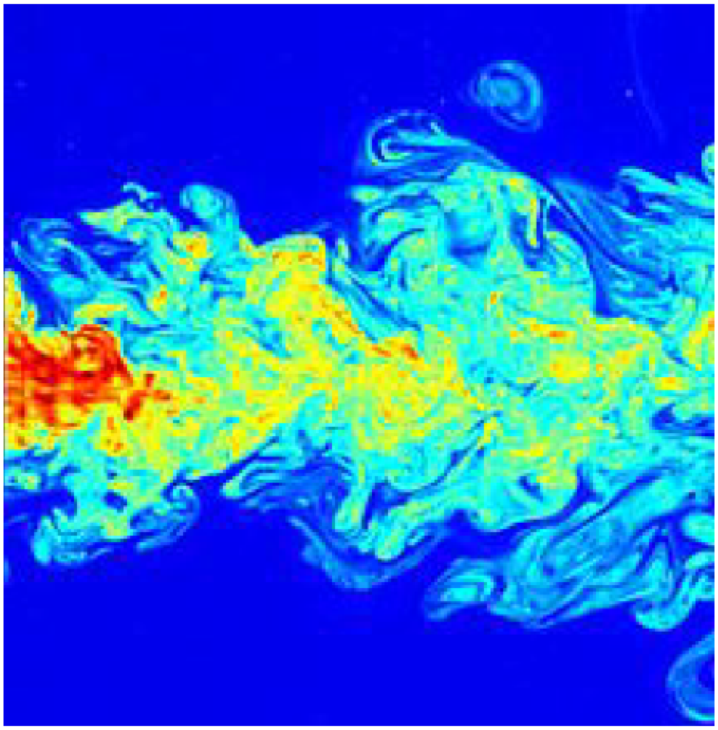

Figure 21: Illustration of turbulent eddies [27].

The turbulent kinetic energy K can be expressed as:

$$K = \frac{3}{2} \cdot (uI)^2 , \tag{32}$$

where I is the initial turbulence intensity and u is the initial velocity magnitude. Furthermore, the turbulence intensity I, can be referred to as the turbulence level. This dimensionless parameter can be expressed by:

$$I = 0.16 \cdot Re^{-\frac{1}{8}}, \tag{33}$$

where the Reynolds number is calculated like:

$$Re = \frac{\omega \cdot d^2}{\nu}. \tag{34}$$

Equation (34) involves the angular velocity ω, the diameter of the geometry d, as well as the kinematic viscosity ν.

The turbulent length scale l, represent the size of the eddies in a turbulent flow, and can be expressed as:

$$l = 0.07 \cdot d. \tag{35}$$

The turbulent kinetic energy dissipation rate ϵ is also needed, and can be expressed by:

$$\epsilon = C_\mu^{\frac{3}{4}} \cdot K^{\frac{3}{2}} \cdot l^{-1}, \tag{36}$$

where C_μ is a dimensionless $k - \epsilon$ model parameter, which has a typical value of 0.09 [27, 20].

4 Methodology

This section shows the geometry and mesh used in the simulations. In addition, different models and solvers are presented as well.

4.1 Geometry

The geometry is based on a tank with a cylinder form. This is inspired by the work of Herri et al. [1] with purpose to carry out numerical simulations regarding particle size distribution and particle growth of the hydrate phase. The cylinder has a volume of 900 cm^3, a diameter of 10.80 cm and height 9.82 cm, which is illustrated in figure 22. The suspension is stirred with a four-blade radial impeller driven by a vertical shaft connected to the top of the cylinder. A radial impeller pushes the fluid to the sides rather than up or down. It also has a constant angle of attack that typically results in high shear rates. The geometry contains also four equal sized baffles in the outer region of the cylinder. These baffles prevent any unwanted turbulent eddies near the outer region of the cylinder, and can be viewed in figure 23. The system is filled with liquid water with a density corresponding to a pressure and temperature of 30 bar and 1°C, respectively. Depending on what the objective is, a certain number of dispersed phases are added to the tank, representing hydrate particles with suitable density. Several parameters can then be measured for different stirring rates of the impeller. These numerical simulations are all conducted with different stirring rates. The experimental setup from Herri et al. [28] can be viewed in figure 26.

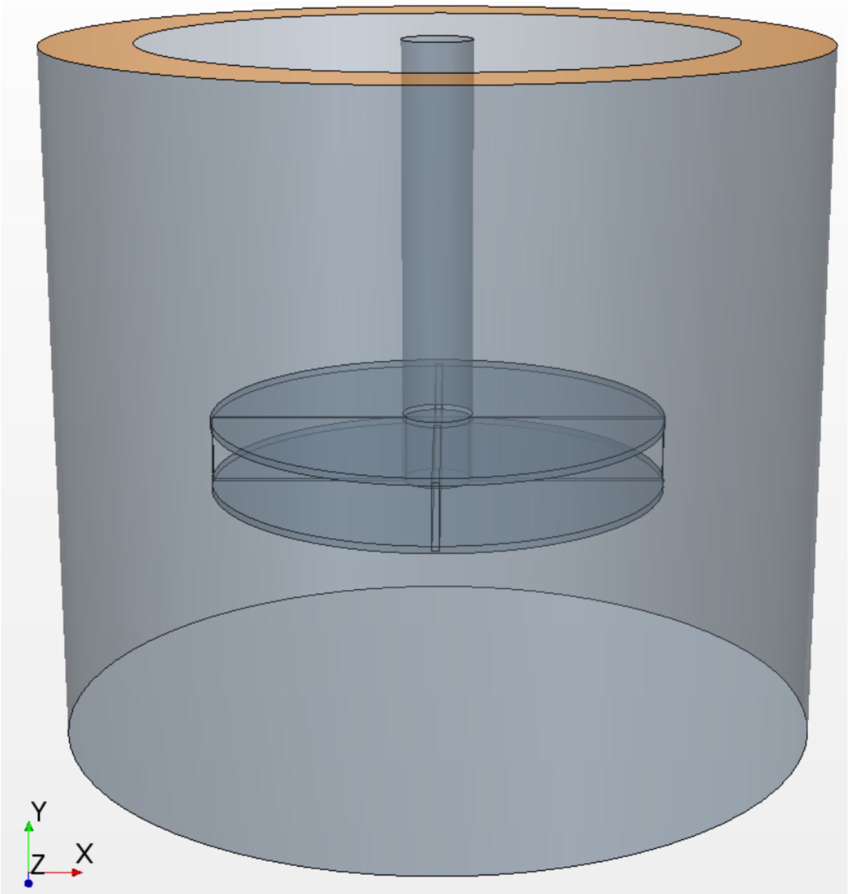

Figure 22: See-through CAD model of the cylinder.

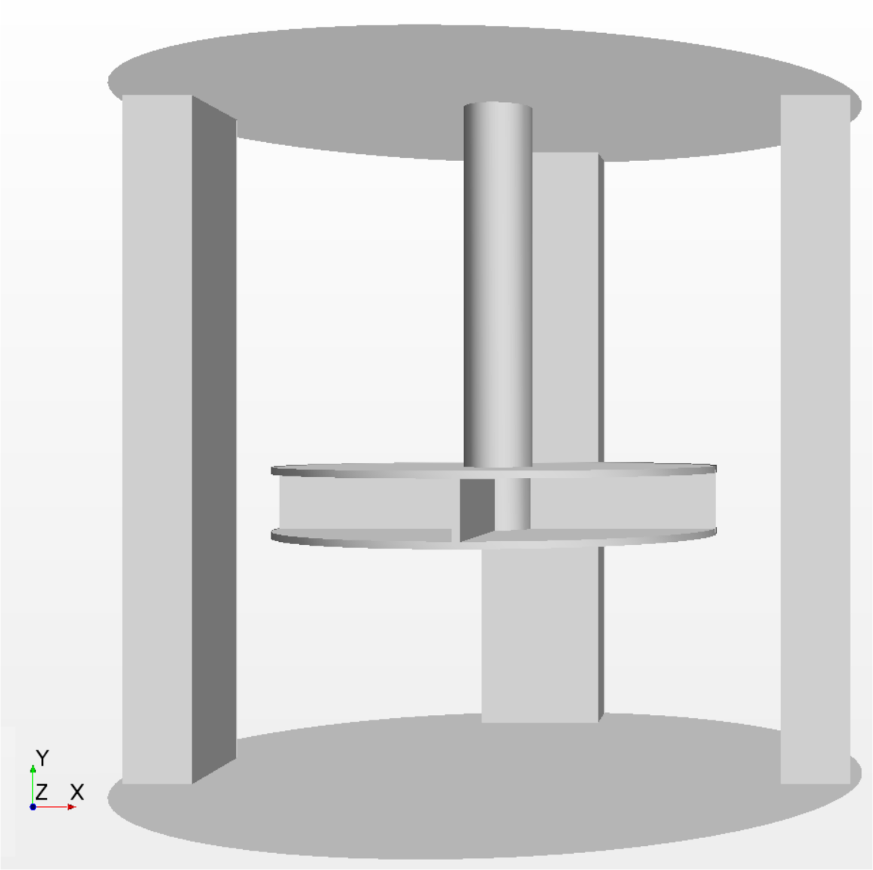

Figure 23: CAD model of the radial impeller rotating with 250 to 600 rpm. The four baffles are located in the outer region. One baffle as well as the side walls of the cylinder are hidden for illustration purposes.

To define the solutions to our CFD problems, it is essential to characterize the boundary conditions. The cylinder is divided into two regions, namely a fluid and rotating region. The fluid region is stationary, and the rotating region consists of an impeller, which is shown in figure 24. The cylinder top surface is a pressure outlet, and can be seen in figure 25, while the rest of the geometry are solid no-slip walls. This particular shear stress specification produces a zero velocity for the fluid relative to the boundary.

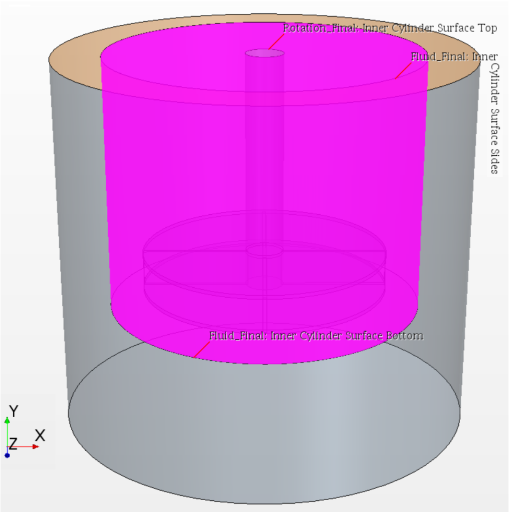

Figure 24: Fluid and rotating region boundaries.

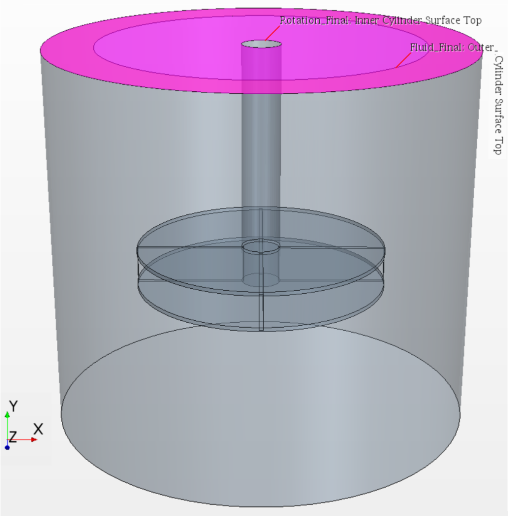

Figure 25: The top boundary for the cylinder is a pressure outlet.

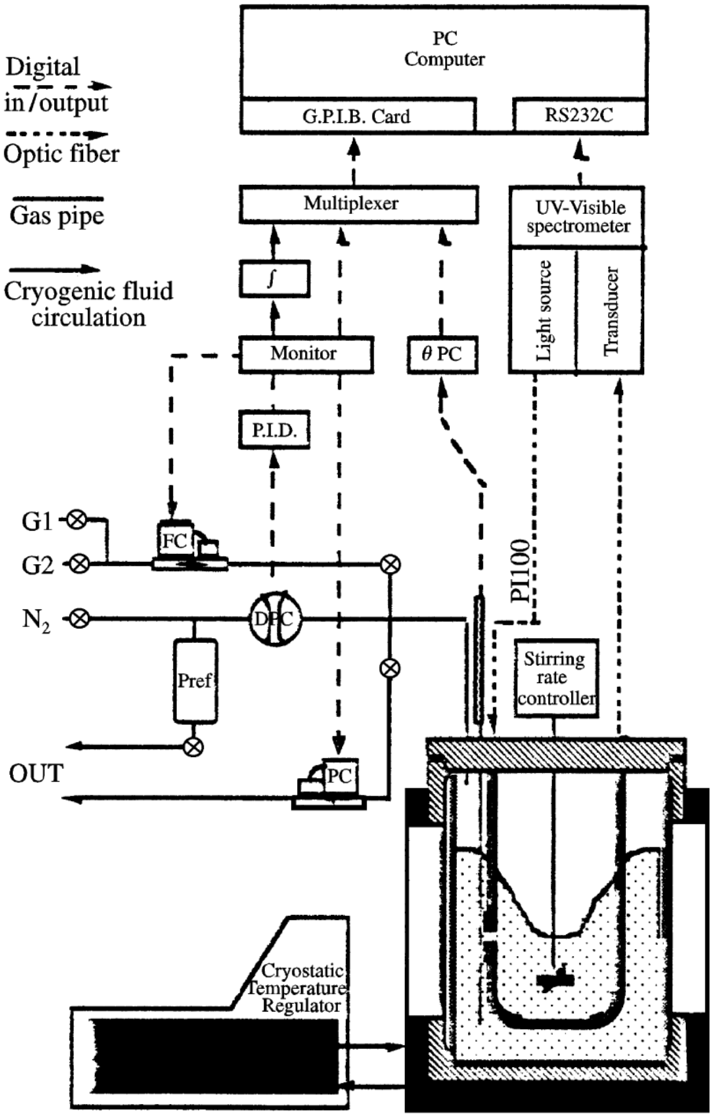

Figure 26: Experimental setup used in the work of Herri et al. [1], where the tank is located in the bottom corner [28].

4.2 Model description

The $\kappa - \omega$ model was only used to perform mesh independence and validation of the simulations. Initial conditions for the turbulence kinetic energy (TKE) parameters can be viewed in table 2. Validation of the simulations was done by measuring the velocity as a function of position, which can be viewed in section 6.3. This was made possible by inserting probe lines inside the tank, and the location of these probes can be viewed in figure 59.

However, due to problems acquiring values for turbulent dissipation rate ϵ from the software solver, the model was replaced by the $\kappa - \epsilon$ turbulence model for the numerical simulations shown in this thesis. This allowed extraction of turbulent dissipation rate ϵ from the solver. Details of the $\kappa - \epsilon$ model can be viewed in section 4.2.1.

Table 1: The most important physical models and solvers selected to make up the simulation-environment

General Models	$\kappa - \epsilon$ Turbulence, Three-Dimensional Implicit Unsteady, Reynolds-Averaged Navier-Stokes Two-layer All Y+ Wall treatment, Constant Density
Solvers	Implicit Unsteady, Segregated flow, $\kappa - \epsilon$ Turbulence

Table 1 shows the most important physical models and solvers selected for the simulations.

4.2.1 General models

The system was three-dimensional and the numerical method was an implicit unsteady model. The segregated flow model is an alternative for incompressible or mildly compressible flows, especially when computational time is considered. It was assumed that the fluid was incompressible through the continuum, and therefore constant density was selected for the equation of state.

Since this was a turbulent environment, the Reynolds-averaged Navier-Stokes model was selected. This led to the choice of the $\kappa - \epsilon$ turbulence model and therefore the two-layer all y+ wall treatment. The $\kappa - \epsilon$ turbulence model is a two-equation model type which is in control of computing transport equations for the turbulent kinetic energy κ and its dissipation rate ϵ to determine the turbulent viscosity [20].

Values of y+, especially in the rotating region, was monitored during the simulations for flow-pattern validation purposes. Since walls are a source of vorticity in most flow problems, an accurate prediction of turbulence and flow parameters across the wall boundary layer is crucial [20].

4.2.2 Solvers

The implicit unsteady solver handles the update at each physical time for the calculation. In addition, it controls the time-step size. The segregated flow solver controls the solution update for the segregated flow model using a mathematical algorithm. This solver type includes two additional solvers for the velocity and pressure, where it is possible to set under-relaxation factors and algebraic parameters. The $\kappa - \epsilon$ turbulence solver handles the solution of the turbulence transport equations in the whole continuum for which $\kappa - \epsilon$ is activated.

4.2.3 Initial conditions for TKE

TKE parameters are calculated using the equations described in chapter 3.9, where the values can be seen in table 2. This procedure was only done when using the $\kappa - \epsilon$ model doing the mesh independence and validation of flow. Otherwise, default values for the TKE parameters were used.

Table 2: Initial conditions and general properties for the simulations

Parameter	Symbol	Value	Unit
Turbulence Intensity	I	0.045	
Turbulent Length Scale	L	0.0076	m
Turbulent Velocity Scale	u	0.20	m/s
Turbulent Dissipation rate	ϵ	0.0037	m^2/s^3
Turbulent Kinetic Energy	κ	0.0031	m^2/s^2

4.2.4 Mesh

Since Star-CCM+ features a wide range of meshers it is imperative to choose the right one for the specific geometry in question, otherwise the numerical solution might not be accurate. The geometry is split into two regions: a fluid region, which is stationary, and a rotating region that consist of an impeller that rotates. Therefore, the type of mesh will differ for each of them. The fluid region has a polyhedral mesher and a surface remesher model selected. The latter, was chosen to improve the general quality of existing surface. It was used to retriangulate the surface. For the rotating region the polyhedral- and prism layer meshers were selected in addition to the surface re-mesher and surface wrapper [20].

The objective of the polyhedral mesher is to produce a balanced solution for complex mesh generation problems. This model applies an polyhedral shape of the cell to build the core mesh. In general, an average of 14 cell faces per polyhedral cell is created. The polyhedral mesh properties was constructed using a continuum mesh for this region. The base size was set to 1.5 mm both for the fluid and rotating region after numerous experiments to find a satisfying result. It was found to be an acceptable balance between computational time and detail. See chapter 6.3 for more discussion [20].

A prism layer mesher was selected for the purpose to generate orthogonal prismatic cells next to wall surfaces or boundaries. This was interesting since it may improve the accuracy of the flow solution. In this case, one prism layer with a 200 % size relative to base was sufficient. Its absolute size was therefore 3 mm.

The surface wrapper was used on the rotating region since the geometry of the impeller section is relatively complex with multiple intersecting small parts. This tool can generally be used if the geometry is overly detailed. Its purpose is to close any gaps, provide a triangulated surface definition and simplifying the surface geometry by removing non-essential detail. Commonly it is used with the surface re-mesher to maintain a high quality starting surface for the volume meshers [20].

4.3 Model description: Eulerian-Eulerian Multiphase

For the 2-phase CFD-PBM simulation model, there was only one dispersed hydrate phase added to the system. For the 5-phase CFD model, the procedure was to add five dispersed hydrate phases with different particle size for each of them to the cylinder tank, couple them with volume fraction, take the average size, and compare with the laboratory experiments done by Herri et al. [1]. This can be expressed as:

$$\bar{d} = \frac{d_1 \cdot \phi_1 + d_2 \cdot \phi_2 + d_3 \cdot \phi_3 + d_4 \cdot \phi_4 + d_5 \cdot \phi_5}{\sum \phi}. \tag{37}$$

For the different stirring rates, the base size of the mean particle diameter d_{avrg}, is from the experimental values of Herri et al. [1], which can be seen in table 9. These experimental values are labelled as "Phase 1" in tables 3 and 4 and show the distribution of the particle diameter for the other phases as well.

Table 3: Distribution of particle diameter of the dispersed hydrate phases for stirring rates 350-600 rpm

Phase	d_{avrg} 600 rpm [μm]	d_{avrg} 450 rpm [μm]	d_{avrg} 350 rpm [μm]
1	18.57	15.41	15.54
2	27.86	23.12	23.31
3	32.50	26.97	27.19
4	9.29	7.71	7.77
5	4.64	3.85	3.88

Table 4: Distribution of particle diameter of the dispersed hydrate phases for stirring rates 250-300 rpm

Phase	d_{avrg} 300 rpm [μm]	d_{avrg} 250 rpm [μm]
1	15.71	15.30
2	23.57	22.94
3	27.50	26.77
4	7.86	7.65
5	3.93	3.82

The particle size values for the different phases listed in table 3 and 4 represents an increase of 50 % and 75 % for phase 2 and 3, while a decrease of 50 % and 75 % for phase 4 and 5 in respect of the base size.

Table 5 shows the most important models that were selected.

Table 5: The most important physical models and solvers selected to make up the simulation-environment for five dispersed hydrate phases

General Models	Three-Dimensional, Implicit Unsteady Cell Quality Remediation, Gravity Eulerian Multiphase, Multiphase Interaction, Multiphase Segregated Flow
Solvers	Implicit Unsteady, Multiphase Segregated Flow $\kappa - \epsilon$ Turbulence, Volume Fraction
Eulerian Multiphase	Constant Density Two-Layer All Y+ Wall Treatment $\kappa - \epsilon$ Turbulence, Liquid, Particle Reynolds-Averaged Navier-Stokes
Multiphase Interaction	Drag Force, Interaction Length Scale Multiphase Material Continuous-Dispersed Phase Interaction

4.3.1 General models

The cell quality remediation model contributes to and improves the general robustness of the solution. It identifies poor quality cells and modifies them after certain criteria have been met [20].

The task of a multiphase segregated flow model is to solve the conservation equations for each Eulerian phase present in the simulation environment.

In addition, gravity is also selected. Other general models can be viewed in section 4.2.1 chapter.

4.3.2 Eulerian Multiphase- and Multiphase Interaction models

Water is chosen as a liquid for the tank with a density at 1001.36 kg/m^3 [29], which corresponds to a temperature at 1°C and 30 bar of pressure inspired by the experimental setup from Herri et al. [1]. Ice is chosen for the hydrate particles with a density of 910.0 kg/m^3 [1]. Since particles are present, the drag force model is necessary for calculating the force on the particles in the dispersed phase due to its velocity relative to the continuous phase. The particle mean diameter is chosen from the interaction length scale model. It is also required to define which is the continuous and dispersed phase, and the continuous-dispersed phase interaction model takes care of this.

4.3.3 Initial conditions

Table 6 show the default values are used for the initial conditions in this case.

Table 6: Initial conditions and general properties for the simulations

Parameter	Symbol	Value	Unit
Fluid Density	ρ_c	1001.36	kg/m^3
Particle Density	ρ_c	910.00	kg/m^3
Fluid Dynamic Viscosity	μ_c	$1.72 \cdot 10^{-}3$	Pa · s

The initial volume fraction is different for each stirring rate and can be seen in table 8. However, for the 5-phase CFD simulation, all five dispersed phases had the same initial volume fraction for that stirring rate. This is to avoid any excessive complications with the simulation and computational time.

4.3.4 Mesh

The mesh is imported from the $\kappa - \epsilon$ model setup, see chapter 4.2.4 for more information.

4.4 PBM model

Particles can alter and affect the flow behaviour in a system considerably. A population balance approach can be utilized to achieve better understanding of processes where the size of solid particles changes, and to determine the extent of these particles influencing the fluid flow. The goal is to predict the evolution of the PSD of these particles. An illustration of the population balance principle is shown in figure 27 [13]. According to Dehling et al. [30], the PBM research field has received increasingly attention in the last decade. Nevertheless, PBM has been extended to the study of other particle properties than size, i.e. particle density and particle composition [13, 31].

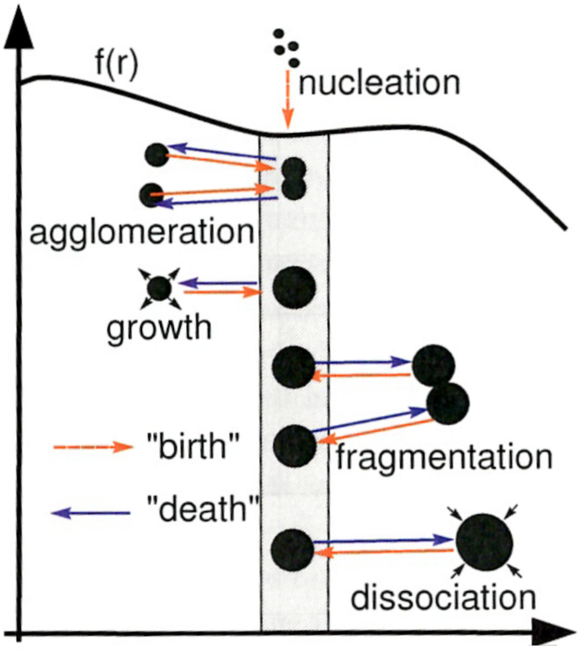

Figure 27: An illustration of the population balance principle [13].

This section presents the PBM model used for simulating chemical growth of hydrate particles. The PBM technique is a scientific framework that is often applied to systems describing how the amount of particles in a certain size band of their PSD changes due to their rate of "birth" and "death" kernel, which will be explained later in this section. The PBM method was developed by Smoluchowski, and this is a much faster and simpler alternative to DEM-modeling of flow containing gas hydrates, which involves a separate numerical treatment of single particles. Instead, the PBM technique handles moments of the size distribution. In general, a PBM model combined with CFD is often focused on prediction of the particle size as well as the total number of particles within a computational cell [32].

In this thesis, a 2-phase CFD-PBM model was developed for an agitated system filled with a water-hydrate slurry mixture pressurized with natural gas, where the concentration of the gas was set to the top boundary of the tank. Therefore, the moments of the PSD were also applied to this boundary. Numerical simulations of how the hydrate particles grew were performed, and growth rate was therefore needed. To achieve this, information about concentration of methane for the whole tank had to be collected. Nevertheless, it was decided to implement only growth rate, and not agglomeration, from the PBM model developed by Herri et al. [1], and the moments of the particle size were coupled with the continuous phase as passive scalars in the simulation software.

The model description is basically the same as in section 4.3.2 with a few adjustments. Instead of five dispersed phases, we reduce the number to just one dispersed- and one continuous phase. The initial conditions have also been adjusted, and these parameters can be seen in table 7. In addition, the turbulence specification parameters are set to their default values.

The population balance equation of the hydrate crystals, which describes the change of the PSD, can be expressed as [33, 1, 13]:

$$\frac{\partial f}{\partial t} + G\frac{\partial f}{\partial R} = B'\left(R\right) - D'\left(R\right). \tag{38}$$

The "birth" kernel $B'\left(R\right)$, represent the increase of the amount of particles due to nucleation, growth or agglomeration of smaller particles. Nevertheless, this can also be due to dissociation or fragmentation or larger particles. On the other hand, the "death" kernel $D'\left(R\right)$, is the decrease of the number of particles due to the same phenomena, except for nucleation. Furthermore, R is the particle radius, G is the growth or dissociation rate and $f(r)$ is the number density function [1, 13].

Equation (38) can be simplified with the introduction of moment transformation:

$$M_j = \int_0^\infty r^j f(r) dr, \tag{39}$$

where M_j is the j-th moment of particle size distribution. Thus, the population balance equation can be transformed into a differential equation [1]:

$$\frac{dM_j}{dt} = j \cdot G \cdot M_{j-1}. \tag{40}$$

The first four PSD-moments physically represent the number of particles, their size, area and volume [13]. The 0th moment is therefore equal to the total number of particles per unit volume, and the expression becomes:

$$N_T = M_0, \tag{41}$$

where this is estimated to $N_T = M_0 = 1 \cdot 10^6$.

For the bulk zone, the mass balance equation in dissolved methane becomes:

$$\frac{dC_b}{dt} = k_L a_l \cdot (C_{ext} - C_b) - \frac{4 \cdot \pi}{\nu_m} \cdot G M_2, \tag{42}$$

where $k_L a_l$ is the methane absorption and M_2, which is the second moment of the particle size distribution. Methane absorption is used for the calculation of methane concentration C_b. C_{ext} is the interfacial concentration imposed by the gas/liquid equilibrium and ν_m is the molar volume of the hydrate particles.

Equation (42) is used for calculating how much methane is dissolved in water. The first term, $k_L a_l \cdot (C_{ext} - C_b)$, provides information about methane concentration that originates from the surface. The second term, $-\frac{4 \cdot \pi}{\nu_m} \cdot G M_2$, describes gas hydrates consuming the phase.

The growth rate term is proposed by Herri et al. [1] in the form:

$$G = k_g \left(C_b - C_{eq} \right), \tag{43}$$

where C_{eq} is the equilibrium concentration in dissolved methane in the presence of the hydrate phase, and C_b is the bulk methane concentration. The growth rate constant k_g, which can be seen in equation (13) in Herri et al. [1], includes incorporation of gas molecules into the hydrate structure and gas transport from the bulk of the solution to the liquid/crystal interface. However, the growth rate constant k_g, is presented in a different way in Herri et al. [1], compared to what is needed in this thesis. The growth rate constant k_g does not account for local properties. There is a better way to express this parameter, which will be called k_d from now on. The parameter k_d is also included in the expression for the Sherwood number for the particle:

$$Sh_p = \frac{k_d \cdot D_p}{D_v}. \tag{44}$$

To calculate the Sherwood number for the particle, the Ranz-Marshall correlation can be used. This is written as:

$$Sh = 2 + 0.6 Re_r^{0.5} Sc^{0.33}, \tag{45}$$

where Re_r is the relative Reynolds number, which represents the relative speed between the droplet and the carrier liquid [21]. In this thesis, the Reynolds number for the particle will be used to calculate the particle growth rate in the tank:

$$Re_p = \frac{\rho_c \cdot |\vec{v_c} - \vec{u_d}| \cdot {d_p}^2}{\mu_c}, \tag{46}$$

where this expression is calculated based on the particle size and introduces the magnitude of the velocity difference in the continuous and dispersed phase $|\vec{v_c} - \vec{u_d}|$. The parameter d_p is the diameter of the particle and μ_c is the viscosity of the continuous phase.

The Schmidt number Sc is the relation between viscous diffusion rate and molecular diffusion rate, where this parameter can be defined by:

$$Sc = \frac{\nu}{D_v}, \tag{47}$$

where ν is the kinematic viscosity of water.

Finally, the diameter of the particle can be expressed as:

$$2 \cdot R = \frac{M_1}{M_2}. \tag{48}$$

Table 7: Initial conditions and general properties for the PBM-model

Parameter	Symbol	Value	Unit
Particle Density	ρ_d	910.00	$\mathrm{kg/m^3}$
Fluid Density	ρ_c	1001.36	$\mathrm{kg/m^3}$
Fluid Dynamic Viscosity	μ_c	$1.72 \cdot 10^-3$	$\mathrm{Pa \cdot s}$
Growth Rate	G	$3.30 \cdot 10^{-8}$	m/s

The methane concentration in the continuous phase, pressure outlet top region and the equilibrium concentration is set to 60 $\mathrm{mol/m^3}$, 73.6 $\mathrm{mol/m^3}$ and 68.9 $\mathrm{mol/m^3}$, respectively. The volume fractions for the hydrate phase is set to an average value found from Herri et al. [1] for the different stirring rates, which can be seen in table 8. The initial hydrate volume fraction is applied to a layer in the top area of the tank, which can be seen in figure 28. The values is from the experiments of Herri et al. [1]. The value for the volume fraction of water is set to 1- ϕ_{hyd}.

Table 8: Initial conditions for the hydrate volume fractions at different stirring rates

Stirring rate [rpm]	Hydrate Volume Fraction Value [μ]
600	812.93
450	219.11
350	148.02
300	261.67
250	258.51

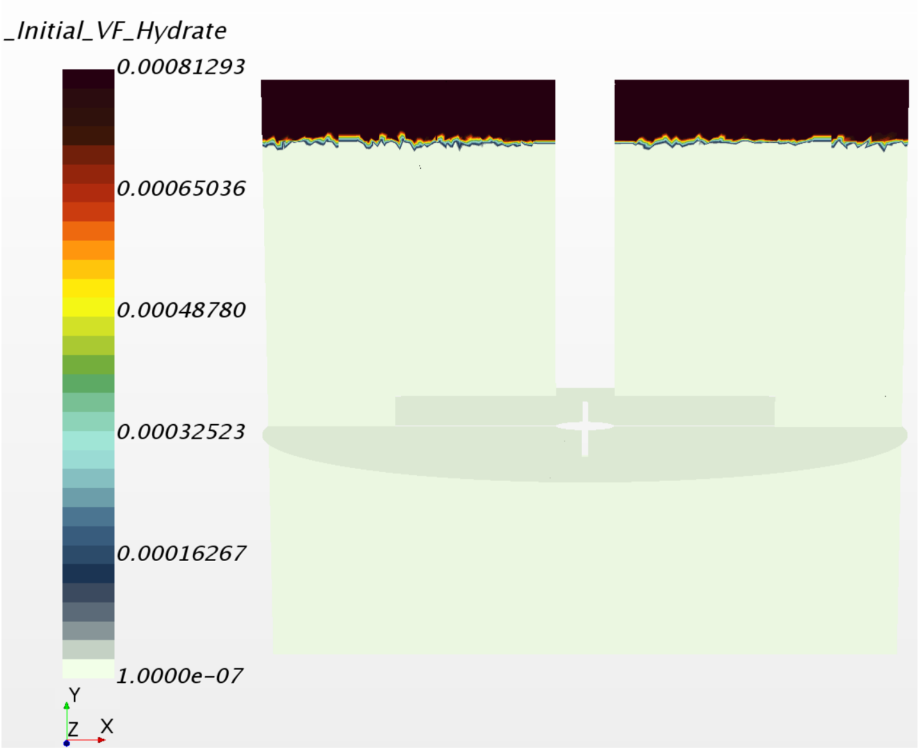

Figure 28: Initial hydrate volume fraction location in the tank.

For the population balance, there are two zones that can be identified as stated by Vysniauskas et al. [34] and Jones et al. [35], and can be seen in figure 29.

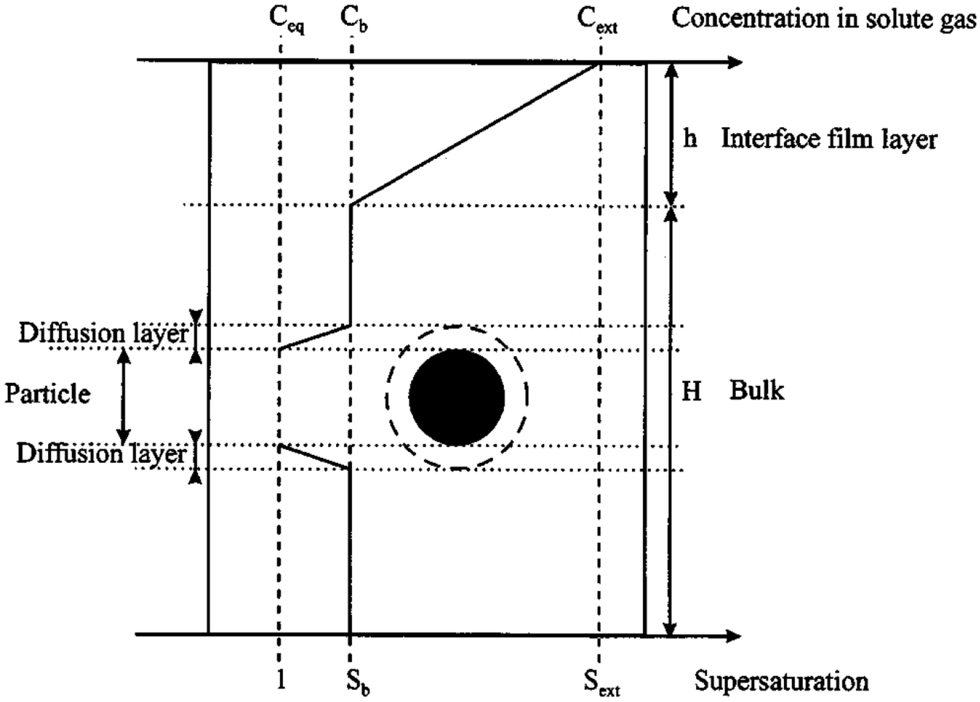

Figure 29: Overview of the different concentration profiles in the stirred tank [1].

The first region is the interface layer, which measures roughly a few tens of micrometers. Due to the small size of this zone, there should be a constant concentration gradient in dissolved methane. This zone involves only primary nucleation as a crystallization method. This area contains a high level of supersaturation in contrast to the rest of the tank. Therefore, primary nucleation is especially active in the interfacial film. This is considered to be a source of nuclei for the bulk zone of the tank.

The other zone is called the bulk zone, which should have a homogeneous concentration and is responsible for the crystallization process. This includes primary nucleation, growth, agglomeration and secondary nucleation.

The population balance equation of the hydrate crystals and the mass balance equation in dissolved methane in the bulk zone are the main equations that describe the time progression in the system. However, the main variables are the concentration C_b in dissolved methane in the bulk zone and the population density function in the bulk zone $f(R,t)$ [1].

It is important to understand how to simulate methane dissolved in water. It is possible to solve for diffusion of an component within the flow. Since the diffusion is constant for methane in water, it should be achievable to successfully simulate. Herri et al. [1] conducted their experiments and found the concentration of methane in water as:

$$Supersaturation = \frac{C_{CH4}}{C_{eq}}. \tag{49}$$

Their simulation of the supersaturation in a simplified model of primary nucleation / growth can be illustrated in figure 30.

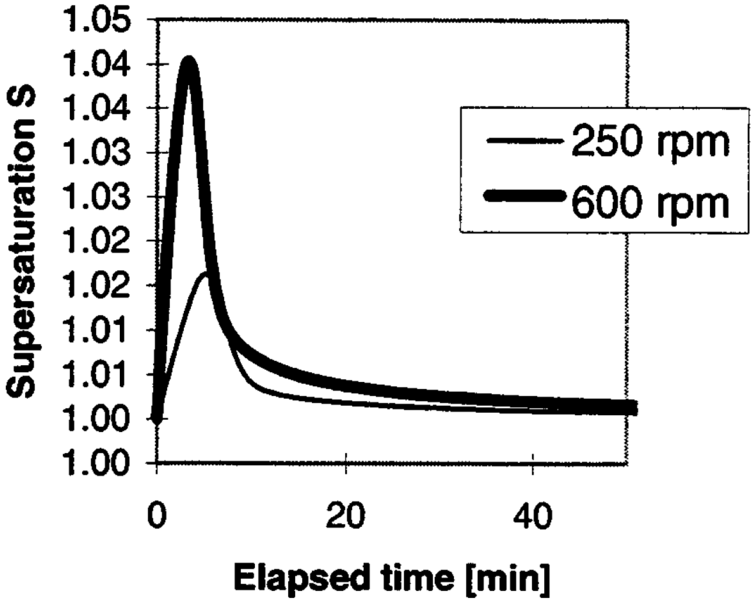

Figure 30: Illustration of the simulated supersaturation as a function of time [1].

Methane absorption rate, $k_L a_l$, as a function of stirring rate ω is also important to study to successfully implement the diffusion of methane for the simulations. Herri et al. [1] provides this influence of the stirring rate on the rate of methane absorption, and is shown in figure 31. The expression for the dissolution rate can be viewed in equation 50.

$$r = k_L a_l \cdot (C_{ext} - C_b) \, . \tag{50}$$

However, a constant growth rate was introduced to reduce the computational costs. In addition, the moments were kept coupled with the continuous phase instead of the dispersed phase to eliminate errors. It means that the growth rate is no longer dependant of the growth rate constant k_d. Therefore, several parameters described above are not needed in this approach. The new expression for growth rate is then:

$$G = G_{estimated} \cdot \frac{C_{CH4}}{\bar{C}_{CH4}}, \tag{51}$$

where the values of $G_{estimated}$ and the initial concentration of methane C_{CH4}, are 3.30 $\cdot 10^{-8}$ m/s and 60.0 mol/m^3, respectively. The average concentration of methane during the simulation, $\bar{C}_{CH4}$ changes in time, and the graph is shown in figure 32.

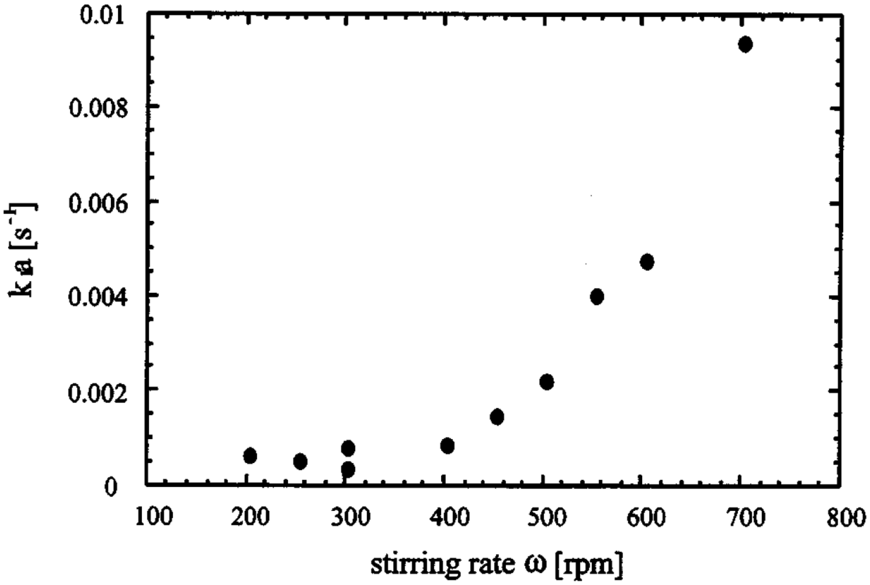

Figure 31: Illustration of methane absorption $k_L a_l$ as a function of stirring rate ω [1].

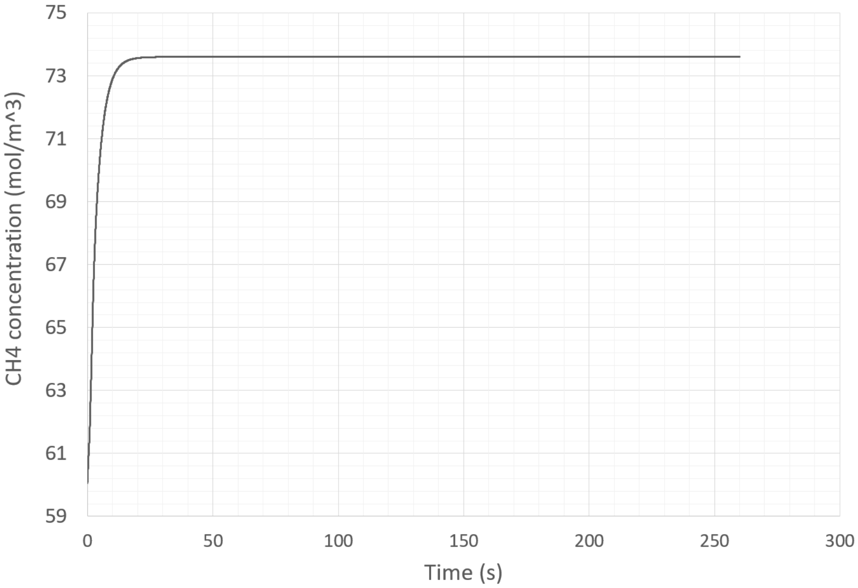

Figure 32: Methane concentration for the 2-phase CFD-PBM model.

5 Literature survey

This thesis focus on hydrate particle size distribution (PSD), which describes particle dispersion in a system. In addition, growth of particle hydrates over time were also studied, where a population balance model (PBM) for a water system was introduced. This enables the possibility for CFD simulations of both topics in a three-dimensional domain.

This following literature survey addresses previous research and experiments performed on gas hydrate agglomeration, particle growth, numerical-simulations and particle size distribution.

For oil/gas systems, there have been numerous experiments and theoretical studies of this subject in the literature. This is a complex subject, which includes multiphase-flow, thermodynamics, chemistry and solid mechanics. Since the formation of gas hydrates requires both low temperature and high pressure, performing real world experiments could be a challenge. Because of the high pressure needed, safety considerations come into play making the process of reproducing industrial conditions in a laboratory setting difficult. The use of CFD enables the possibility to overcome these obstacles and simulate the different scenarios with ease. Nevertheless, certain simplifications may be introduced due to computational time and resources. In spite of it, CFD gives us detailed information about the behaviour of fluid and particle interactions [13].

5.1 Experimental Studies

5.1.1 Methane hydrate crystallization

Herri et al. [1] performed experiments of the crystallization process of methane hydrate and the influence of the stirring rate. Since a large pressure and low temperature are needed for the crystallization process to take place, these conditions are often met in underwater pipelines. These experiments were motivated by the incorporation of a vast amount of additives to alter the equilibrium temperature of formation and the chemical potential so that the crystallization process was prevented. The greater the depth and pressure in question, the larger quantity needed.

In later years, additional additives have been discovered to be immensely more efficient, and require often only 1 % in weight of the water phase, where others could easily require 50 %. Herri et al. [1] pursued this concept that the nature of additives is not fully understood. The reason for this was the lack of experimental studies regarding the nucleation growth of the hydrate phase.

An experimental setup that includes a pressurized reactor, where relevant process and parameters could be investigated was built. A turbidity sensor was responsible for collecting data of the PSD, and therefore used for the methane hydrate crystallization identification. An optical method is less intrusive with the data collection among the many methods of gathering data regarding PSD. Methane was injected to the reactor filled with liquid water. Because of the high level of methane concentration, the vital zone was identified as the gas/liquid interface.

Bishnoi et al. and Englezos et al. [34, 36, 12] observed the appearance of the first crystals in the film region just beneath the gas/liquid interface. Afterwards, it dispersed in the bulk. This observation was found by most of the scientists researching the process of gas hydrate crystallization. Bishnoi et al. proposed the gas/liquid interface approach as a solution of the mentioned problem. These authors suggested a correlation between crystal growth rate and gas consumption rate, where they determined the growth to be the rate-determining step of crystallization. This was later questioned by Skovborg and Rasmussen [37], and by using the experimental data from Bishnoi et al., they suggested a model where the mass transport of gas in the film region is the limiting step. Gaillard and Herri validated this conclusion [38, 1].

The objective of the experiments conducted by Herri et al. [1], was meant to enhance the understanding of the mechanisms of crystallization of methane hydrate. A population balance model for the hydrate crystals was introduced, which in addition to nucleation and growth of hydrate particles, considered agitation-induced agglomeration and hydrodynamic fragmentation. In detail, the PBM model included several parameters like growth rate, death and birth kernel. The death kernel is the decrease of the number of particles due to growth or agglomeration, while the birth kernel is the increase in particles due to the contributions of primary and secondary nucleation, growth or agglomeration. This model was based on the crystallization concept of the gas hydrate formation, and injection of methane gas concentration. Although, this model developed by Herri et al. [1] did not account for the influence of the formation of the solid phase on the mixture viscosity. A mass balance equation for dissolved methane in the bulk zone was used to describe the process of crystallization. The Ranz-Marshall correlation was then introduced, along with Schmidt number, Sherwood number and Reynolds number for the particle. The crystal size is imperative for the validation of this concept, as Skovborg and Rassmussen identified [37]. Herri et al. [1] used PSD in their experiments, for the purpose of control and monitoring, as well as understanding the development of the process. This was then used to gather data about the mean particle diameter as well as total number of particles distributed in the tank for different stirring rates [1].

They conducted successful experiments on the formation of methane gas hydrates. A simplified model of nucleation, or growth, described the influence of stirring rate on the initial total number and the initial mean diameter of the particles. The results from the simulation of a simplified model of particle growth can be seen in figure 33. From their experiments, they found out that for a low stirring rate, the mean particle diameter was relatively small. On the other hand, for a high stirring rate, the mean particle diameter was found to be larger. Influence of agglomeration was tested with intention to explain the development of the mean particle diameter, as well as the total number of particles, as a function of time. However, experiments showed that these phenomena did not have much influence at a low stirring rate, which contradicts the observed increased mean particle diameter. On the other hand, it did describe the curve of total number of particles as a function of time relatively well. The crystallization behaviour at high stirring rates was described using four models, where only one of them was able to correlate with the experimental results [1].

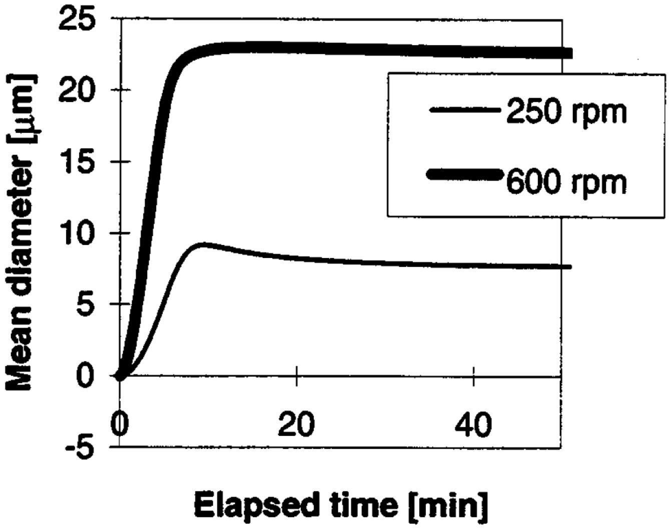

Figure 33: Results from the PBM simulation for a simplified growth model done by Herri et al. [1]. This shows an increasing particle diameter size with stirring rate.

5.1.2 The formation of methane and ethane gas hydrates

Englezos et al. [12] performed experiments to investigate the formation of methane and ethane gas hydrate formation. They focused on a kinetic model with only one adjustable parameter. This parameter is the rate constant for the growth of the hydrate particles. Data were obtained in a semi-batch stirred tank reactor, where they did experiments at different temperature and pressure ranging from 274 K to 282 K, and 0.636 MPa to 8.903 MPa, respectively. For the interfacial mass transfer, the two-film theory was introduced, while the kinetic model was responsible for the crystallization theory. In addition to mass balance expressions, a population balance model was introduced based on the work of Kane et al. [39]. The stirring rates used in this experiment ranged from 300 to 450 rpm, with an increment of 50 rpm.

They calculated the number of moles of the methane gas that had been consumed due hydrate formation or dissolution. With a larger driving force, or higher pressure, a larger amount of methane moles was consumed. On the other hand, a lower pressure resulted in a lower amount of methane moles consumed. This can be viewed in figure 34.

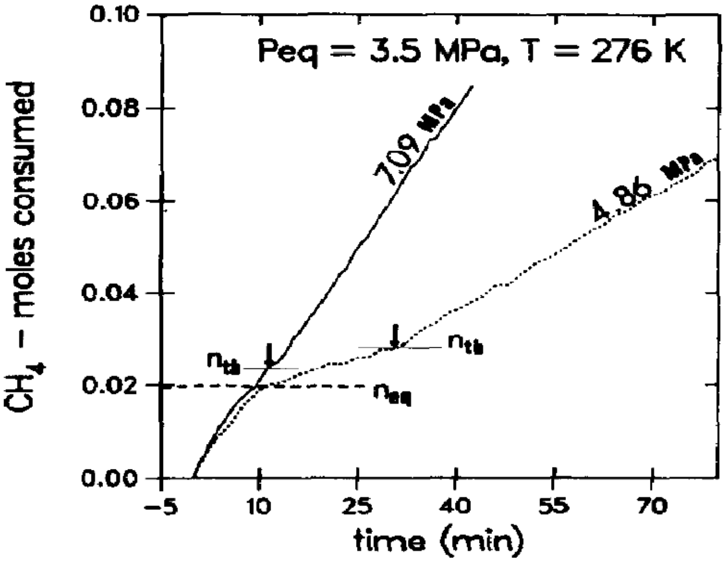

Figure 34: Experimental gas consumption curves for methane hydrate formation with small and large pressure [12].

The arrows in figure 34 indicate the turbidity points in the liquid. The phenomena turbidity is the liquid becoming less clear and transparent due to the development of, in this case hydrate particles. Therefore, the nucleation period ranges from the beginning of the experiment until a point in time indicated by these arrows. Meanwhile, the growth period of the hydrate crystals starts from the arrows and further along the curve as time progresses. This can be interpreted in the direction that with a larger driving force, the induction period is shorter and therefore gas hydrate particles can be observed earlier compared to the lower driving force curve.

Previous research suggests that turbulence and stirring rate influence the crystallization process, crystal size, duration of the induction period and the distribution of crystals in the measured environment. Englezos et al. [12] found out that higher stirring rates resulted in shorter induction periods, which can also be viewed in figure 34. In addition, the amount of gas consumed up to the turbidity point is less for a higher stirring rate. A higher stirring rate then results in a less amount of supersaturation required for hydrate nucleation. This can be viewed in figure 35.

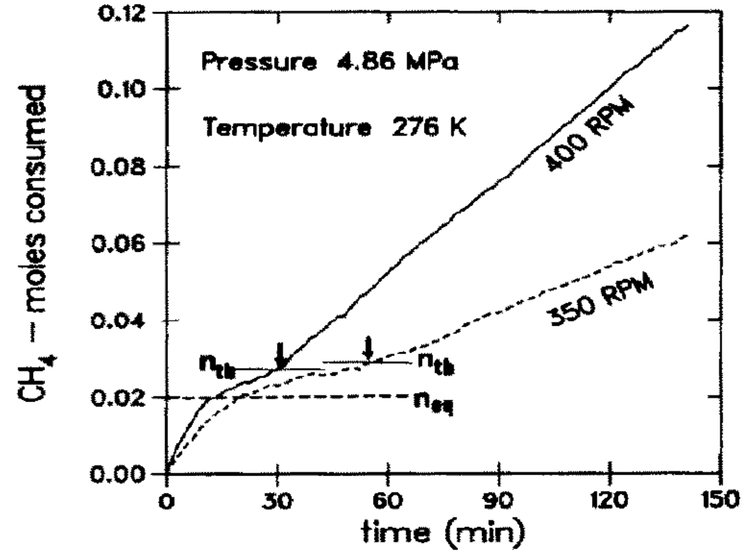

Figure 35: Experimental effects of different stirring rates on the induction period and the supersaturation for the methane hydrate formation [12].

They concluded that as long as supersaturation exists as a result of the dissolution process, gas hydrate formation can develop everywhere in the liquid.

The model developed consisted of one adjustable parameter, namely the rate constant for the hydrate particle growth. Nevertheless, the crystallization theory combined with mass transfer expressions at the gas-liquid interface provides a scientifically description of the formation of gas hydrate formation.

5.2 Numerical studies

5.2.1 Modelling agglomeration and deposition with CFD-PBM technique

Balakin et al. [32] did numerical simulations with the PBM technique coupled with CFD using an Eulerian-Eulerain approach, investigating details about the process of hydrate formation and agglomeration. This model is capable of simulating turbulent slurry of oil, water and hydrates. This research was motivated by the problems of gas hydrates plugging pipelines and other process equipment. Also, the problem increase when the transportation lines gets longer and the operating temperature gets lower. Therefore, accurate gas hydrate risk analysis is valuable for the petroleum industry, where CFD is a tool used to predict the behaviour of artificial gas hydrate build up. The objective was to develop and PBM-CFD model that can predict the formation, agglomeration and deposition of gas hydrates in transportation lines and other equipment in the petroleum industry. Also, it was emphasized that this model should be valid for a general, wide range of scenarios in the industry.

It is challenging to use detailed simulations incorporating the DEM, discrete element method, technique to model the agglomeration of adhesive particles. However, on the industrial scale, DEM is too computationally demanding. On the other hand, PBM is simpler and much faster approach which handles the size distribution, or agglomerate size. Balakin et al. [32] describes a CFD-PBM model capable to simulate the deposition of hydrate particles as well as agglomeration in turbulent oil dominated flows. This model was compared to the CSMHyK [2] rheological model for validation of several independent experimental criterion. This model was based on an apparent viscosity concept, where it assumes that the viscosity of the hydrate particle slurry follows the rheological equation described in [40]. Furthermore, agglomeration and breakage rate constants were determined theoretically ensuring a more general use for a wide range of scenarios in the industry. The PBM model is then incorporated into a similar CFD model as in Lo [41], where the result is a three-dimensional CFD-PBM model using a rheological expression for the apparent viscosity of hydrate suspensions. Finally, they managed to validate the model when integral flow parameters were obtained during a flow loop experiments on hydrate phase formation.

5.2.2 Numerical simulations of adhesive particle agglomeration

Since the particle agglomeration is strongly represented in transportation and production of hydrocarbons, as well as in process equipment in the industry, this phenomenon contributes to operational difficulties. Hellestø et al. [42] performed numerical experiments on sheer-induced agglomeration of adhesive particles in a simple shear flow. A soft sphere collision model was introduced and numerous numerical simulations were performed. The goal was to analyse the results of the simulations in terms of primary particles, magnitude and distribution of agglomerate size and fractal dimension. The results were then compared to existing models, and this revealed in most cases that the development of agglomerates showed maxima.

Other industries are affected by particle agglomeration as well, such as medicine and nano-fluid applications. Some industries have the need for particle agglomeration in their materials and product, such as manufacturing chemicals, ceramics and so on. The knowledge about these mentioned phenomenas and how they work are limited by the experimental studies of the properties of particle agglomeration. Hellestø et al. [42] used as mentioned a soft-sphere model for modeling interparticle interactions. The differential equations of motion for the particles during the collision can then be solved, and therefore provides information about each collision in the flow. However, this is relatively computationally demanding and time consuming.

A two-dimensional flow consisting of particles was simulated studying the agglomeration process taking place in a shear flow. They found out that for an increasing shear rate the rate of agglomeration increased as well. A higher value of fractal dimension, which represent the density of the agglomerate, more densely packed and structurally stable agglomerates were obtained as time proceeded. The fractal dimension was also found to be independent of the magnitude of shear rate. They compared the simulation data with relevant research done by Chimmili et al. [43], Crowe et al., [21] and Mühle [44], which confirmed the theoretical models. The simulation results were therefore in correlation with the literature models.

6 Results and discussion

In this section the results of the analytical analysis as well as the numerical simulations are shown. Attention was paid to three analytical methods and two main simulations with different stirring rates. The analytical analysis concerns the particle diameter size estimation influenced by the stirring rate. The simulations focused on particle size distribution, particle diameter size and particle growth. The simulations are shown using volume average and monitor plots, as well as snapshots illustrating the distribution of particle size and particle growth. Mesh independence was also a part of the simulations to validate the flow and choose the correct mesh size for a balanced simulation environment regarding computational time and the level of accuracy.

6.1 Analytical calculations of the impact of stirring rate on the crystal size

It is important to investigate the influence of the stirring rate on the particle size diameter and the total number of particles to enhance the understanding of crystallization mechanisms of methane hydrate. Herri et al. [1] performed experiments on this issue at a low supersaturation. The low supersaturation ensured that the crystallization process did not occur too rapidly so that the turbidity-measurement system could lead to satisfactory results. Furthermore, their experiments were conducted at temperature 1°C and 30 bar pressure [1]. Using the software PlotDigitizer, digitalized results from their experiments are shown in figures 36 and 37, which depict the particles mean diameter and particles density, respectively.

It is clear that both the particle mean diameter and particle concentration are dependent on the stirring rate. Figure 36 shows that the average particle diameter increases with stirring rate. In addition, as figure 37 shows, the total number of particles increases as the stirring rate increases as well.

The objective is to reproduce and calculate these graphs from the experiments from Herri et al. [1] analytically, and validate their findings. As figure 36 shows, there are two stirrer rate configurations, namely 400 and 500 rpm, that do not represent a configuration that converge, and therefore it is difficult to draw conclusions. As a consequence, these stirrer rates are excluded from further results.

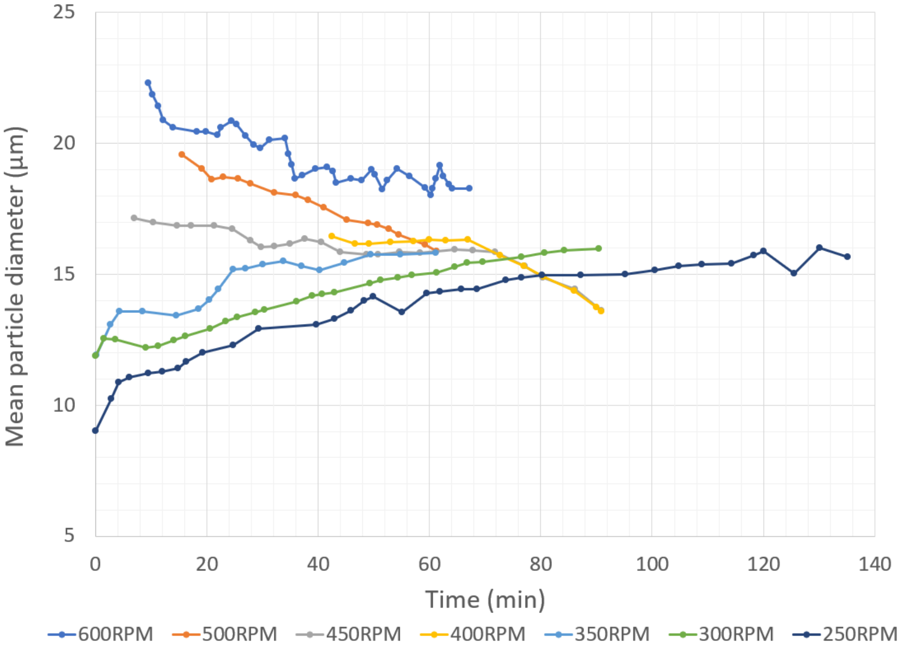

Figure 36: A digitalized particle diameter plot from Herri et al. [1].

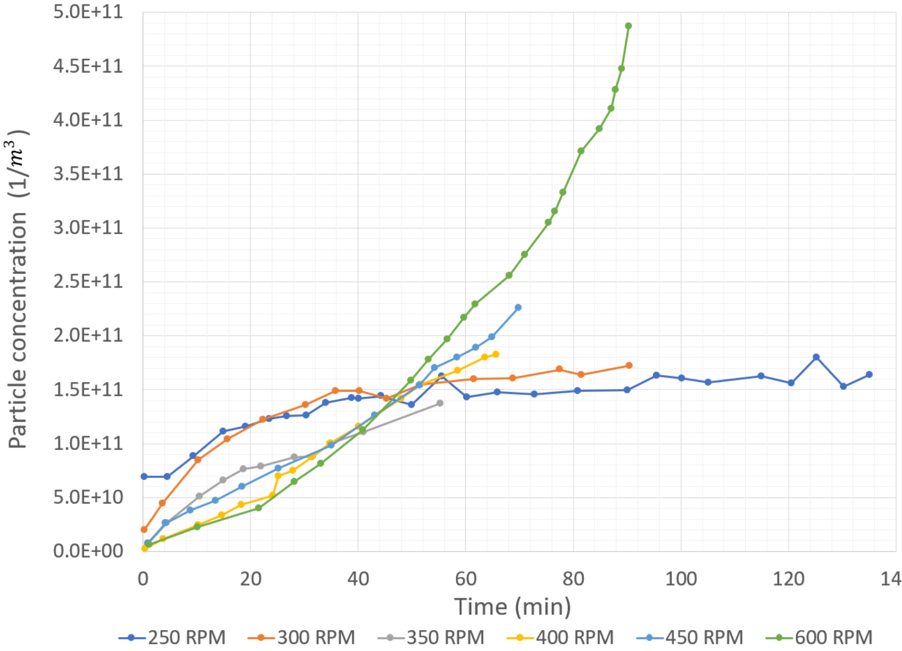

Figure 37: Digitalized particle concentration plot from Herri et al.[1].

Table 9: Mean value of particle diameter for different stirring rates from Herri et al. [1].

Stirrer Rate [rpm]	Particle Mean Diameter [μm]
600	18.57
450	15.41
350	15.54
300	15.71
250	15.30

Table 10: Mean value of particle density for different stirrer rates from Herri et al. [1]

Stirrer Rate [rpm]	Particle Concentration [1/m^3]
600	$2.42 \cdot 10^{11}$
450	$1.14 \cdot 10^{11}$
350	$7.54 \cdot 10^{10}$
300	$1.29 \cdot 10^{11}$
250	$1.38 \cdot 10^{11}$

Figure 38 shows how the particle diameter size increases with stirring rate.

Several methods for analytical calculations of the particle diameter size are shown in the following.

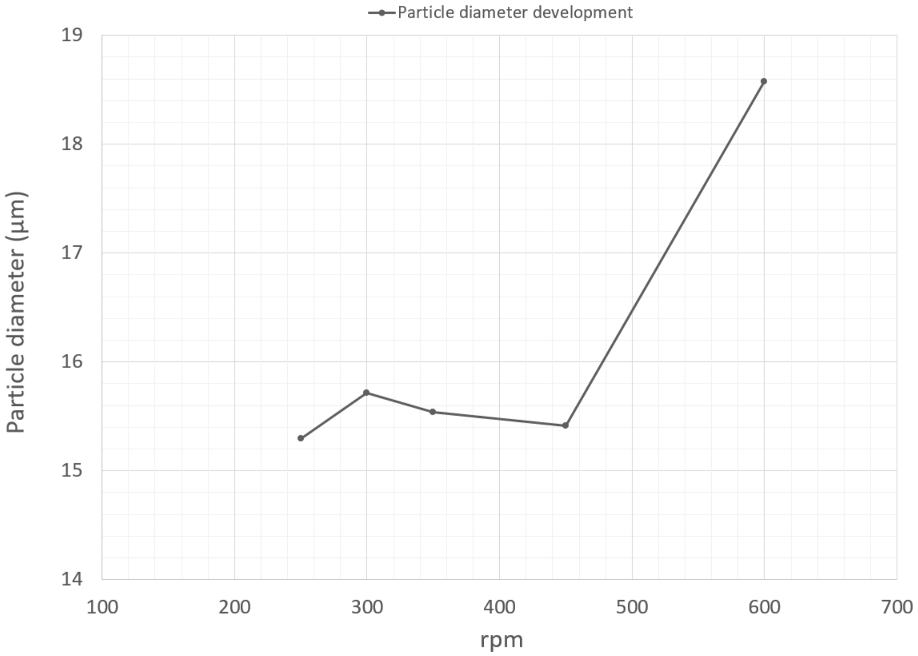

Figure 38: The graph shows the experimental result for the mean particle diameter from the Herri et al. [1] for the different stirring rates.

6.1.1 Particle diameter with shear rate, energy dissipation rate and volume fraction

Hellestø et al. [42] investigated shear-induced agglomeration of adhesive particles in a simple shear flow. They studied and performed numerical simulations of agglomeration of micron-sized particles with the use of a soft-sphere model. A flow driven agglomeration of particles is a process that occurs when particles obtain a relative velocity and collide. An illustration can be seen in figure 39. This relative velocity is caused by shear rate in the carrier phase. Due to these collisions, energy dissipation occurs as a result of various effects. If this dissipation energy is large enough, the particles may not be able to withstand any adhesive force acting between them, hence the particles agglomerate. If it is assumed that all particles that collide will agglomerate, the Smoluchowski equation [45] gives the rate of loss of monodisperse primary particles due to agglomeration:

$$-\frac{dn}{dt} = \frac{16}{3}\gamma {R_0}^3 n^2, \tag{52}$$

where R_0 is the primary particle radius, which are not agglomerated. Furthermore, γ is the shear rate and n is the number of particles per m^3 of suspension.

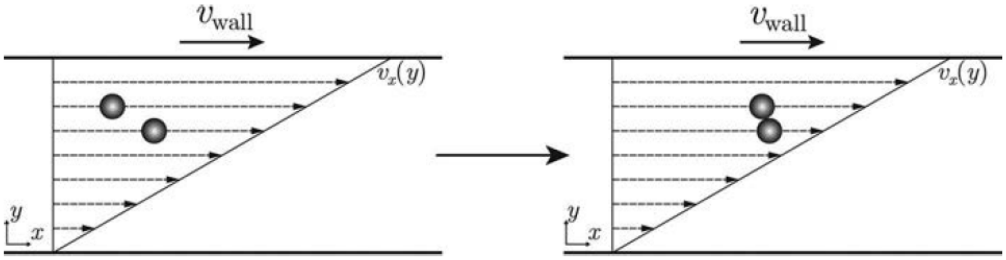

Figure 39: Collision and agglomeration of two particles having a relative velocity due to shear [42].

A collision frequency parameter α, should be multiplied with the right hand side of equation (52). This is due to collisions of particles that bounce off each other, i.e. the collision does not lead to agglomeration. However, after some time the size distribution of the primary particles and agglomerates will evolve, and processes like agglomeration and breakage will continuously occur. Because of this, an equilibrium size distribution will be attained. Using a PBM model, Chimmili et al. [43] derived an equation for the mean particle radius R, as a function of time. This expression was based on the PBM model [45] of equation (52):

$$R = \frac{R_{eq}}{\left[1 + \left(\left(\frac{R_{eq}}{R_0}\right)^3 - 1\right) exp(-\frac{8}{\pi}\phi\gamma\alpha t)\right]^{\frac{1}{3}}}, \tag{53}$$

where R_{eq} is the equilibrium mean particle radius after long enough time to reach equilibrium, and ϕ is the solid volume fraction [42]. As time passes, and the agglomerates have become so large and separated, the flow can be treated as dilute. Due to this, the agglomerates no longer grow considerably. This can be assumed when estimating R_{eq}. However, a criterion was derived by Crowe et al. [21] for the system to be treated as dilute. Hellestø et al. derived an expression for the particle diameter for a dilute flow. The following expression is considered to be the equilibrium agglomerate diameter, and $D_{eq} = 2R_{eq}$ [42]:

$$D_{eq} = \frac{3\mu_c}{\phi\rho_d v_{rel}}, \tag{54}$$

where

$$v_{rel} = \frac{8R_{eq}\gamma}{3\pi}. \tag{55}$$

The parameter v_{rel} is the mean relative velocity in the collision surface around a particle of radius R_{eq}.

Combining equation (55) and (54), the particle diameter can be found [42]:

$$D_{eq} = \sqrt{\frac{9\pi\mu}{4\phi\rho_d\dot{\gamma}}}, \tag{56}$$

where ϕ is the volume fraction:

$$\phi = N \cdot \frac{\pi {d_{avrg}}^3}{6}. \tag{57}$$

The particle diameter d_{avrg} and number density N are both from the experimental mean values, respectively from tables 9 and 10. Furthermore, shear rate $\dot{\gamma}$ is calculated as [1]:

$$\dot{\gamma} = \sqrt{\frac{2}{15}\frac{\epsilon}{\nu}}, \tag{58}$$

where ν is the kinematic viscosity for water and ϵ is the energy dissipation rate.

The energy dissipation rate ϵ is calculated as [31, 1]:

$$\epsilon = \frac{N_p {D_s}^5 (N_{rate})^3}{V}, \tag{59}$$

where N_p is the power number of the stirring device, and is approximated to 1 for a four blade stirrer. The stirrer diameter is the parameter D_s, while N_{rate} is the stirring rate in rounds per second and V as the volume of the stirred medium [1].

Table 11: Parameters and their values for this calculation method of the particle mean diameter

Parameter	Symbol	Value	Unit
Dynamic Viscosity	μ	$1.72 \cdot 10^{-3}$	$\mathrm{Pa \cdot s}$
Kinematic Viscosity	ν	$1.79 \cdot 10^{-6}$	$\mathrm{m^2/s}$
Density Continuous	ρ_c	1001.36	$\mathrm{kg/m^3}$
Density Dispersed	ρ_d	910.00	$\mathrm{kg/m^3}$
Power Number of Stirrer	N_p	≈ 1	
Stirrer Diameter	D_s	0.0647	m
Stirring Rate	N	250-600	rpm
Volume of Stirred Medium	V	$0.90 \cdot 10^{-3}$	$\mathrm{m^3}$

The stirrer diameter D_s is 0.0647 m, which is an average between two values found in two separate sources. Herri et al. [1] and Pic [46] have a stirrer rate respectively of 0.058 m and 0.0714 m.

The results are shown in table 12. It is clear from the results that the particle diameter D_{eq}, for different stirring rates, are significantly larger and does not

Table 12: Calculated values for different stirring rates from experiments.

rpm	Volume Fraction ϕ [μ]	Energy Dissipation Rate ϵ [m^2/s^3]	Shear Rate $\dot{\gamma}$ [s^{-1}]	Particle Diameter D_{eq} [μm]
600	812.93	1.26	306.32	7333.66
450	219.11	0.53	198.96	17527.51
350	148.02	0.25	136.48	25748.09
300	261.67	0.16	108.30	21739.10
250	258.51	0.09	82.39	25076.48

correspond to the results of Herri et al. [1] shown in table 9. It shows that the method from Hellestø et al. [42] does not lead to satisfying results.

6.1.2 Particle diameter with adhesive force using Hamaker constant and subcooling

Another method for calculating the particle diameter was suggested by Sinquin et al. [47] based on the work of Mühle [44]. The equilibrium size was derived from a balance between the shear stress, which disprupts the agglomerates, and the adhesion force, F_a. This gives the maximum agglormerate size, and can be viewed in equation (60). This expression was also used by Hellestø et al. [42]. In addition, a different approach was selected for the adhesive force value which is inspired by Hu and Koh [48]:

$$D_{eq} = \left(\frac{F_a (d_0)^{2-d_f}}{\mu \gamma} \right)^{\frac{1}{4-d_f}} . \tag{60}$$

The primary particle size d_0, was taken from Herri et al. [1], where figure 40 shows the mean primary particle diameter d_0, as a function of time for two stirring rates, and it serves as a simplified model of primary growth.
The fractal dimension value d_f of the agglomerate varies typically between 1 and 3, where $d_f = 3$ gives the maximum agglomerate density. The adhesive force F_a, can be calculated in two ways. Therefore, two separate solutions for the particle diameter are presented that incorporate two different methods for the adhesive force. These two following methods for finding F_a includes

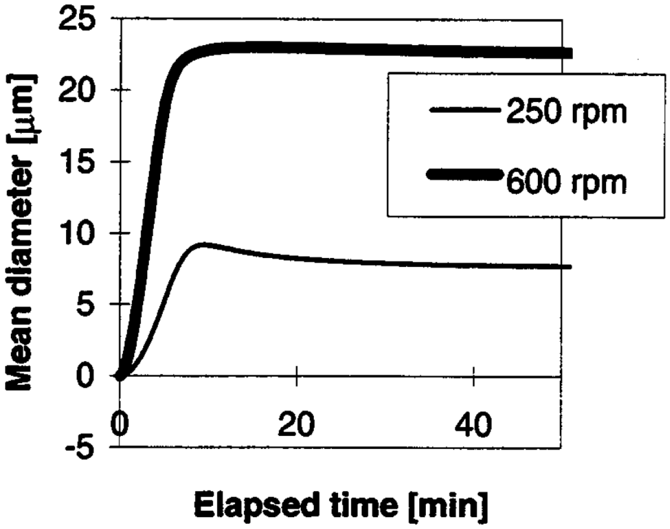

Figure 40: Mean primary particle size d_0, for two different stirring rates [1].

the Hamaker constant and subcooling. The expression using the Hamaker constant is [21]:

$$F_a = \frac{A\frac{d_0}{2}}{12z^2}, \tag{61}$$

where A is the Hamaker constant [49] for a methane hydrate-water system and z is the particle separation distance, where the expression can be seen in equation 31.

In the case where subcooling is used, the expression for the adhesive force becomes [32]:

$$F_a = \frac{d_0}{2} \cdot [0.0017(7.7 - \Delta T) + 0.0007], \tag{62}$$

where ΔT is the difference between the experimental temperature and the equilibrium temperature. In this case, this parameter is the system subcooling relative to the hydrate equilibrium curve which can be viewed in figure 3.

Table 13: Parameters used for calculation of the particle mean diameter.

Parameter	Symbol	Value	Unit
Primary Particle Size	D_0	$2.25 \cdot 10^{-5}$	m
Fractal Dimension	d_f	3.00	
Dynamic Viscosity	μ	$1.72 \cdot 10^{-3}$	$\mathrm{Pa} \cdot \mathrm{s}$
Hamaker Constant	A	$4.59 \cdot 10^{-21}$	J
Particle Separation Distance	z	$9.30 \cdot 10^{-10}$	m
Roughness	d_{nuclei}	$3.40 \cdot 10^{-10}$	m
Mean Free Path	h	$2.50 \cdot 10^{-10}$	m
Temperature Difference	ΔT	≈ 0	K
Adhesive Force Hamaker	F_a	$4.98 \cdot 10^{-9}$	J/m
Adhesive Force Subcooling	F_a	$1.55 \cdot 10^{-7}$	J/m
Adhesive Force CSM	F_a	$1.88 \cdot 10^{-7}$	J/m

Table 13 show the values for the different parameters used for calculating the particle diameter. Values for the shear rate are gathered from table 12. The final result for this calulation method using the adhesive force are listed table 14.

Table 14: Particle mean diameter for the different calculation methods of adhesive force.

rpm	Particle Diameter (Hamaker) D_{eq} [μm]	Particle Diameter (Subcooling) D_{eq} [μm]	Particle Diameter (CSM) D_{eq} [μm]
600	410.62	12803.85	15516.07
450	632.19	19712.81	23888.54
350	921.65	28738.58	34826.22
300	1161.41	36214.75	43886.06
250	1526.72	47605.53	57689.72

In the case of using the method of subcooling for the calculation of F_a, the difference in experimental and equilibrium temperature ΔT, becomes zero at a 30 bar pressure with an experimental value of 1°C. The equilibrium temperature is shown in figure 3.

It is clear the results in table 14 are still not satisfying. Using the Hamaker constant approach results in particle size that is too large. Nevertheless, use of the subcooling approach leads to even higher particle sizes. Likewise, the approach using the adhesive force value from Hu and Koh [48] shows that the values are also too large. It is safe to conclude the values do not correspond to the experiments from Herri et al.[1]. Although, from the results from section 6.1.1 and 6.1.2, a trend of decreasing particle diameter size with stirring rate is shown, which is the opposite of the results from Herri et al. [1]. This trend is shown in figures 41 and 42.

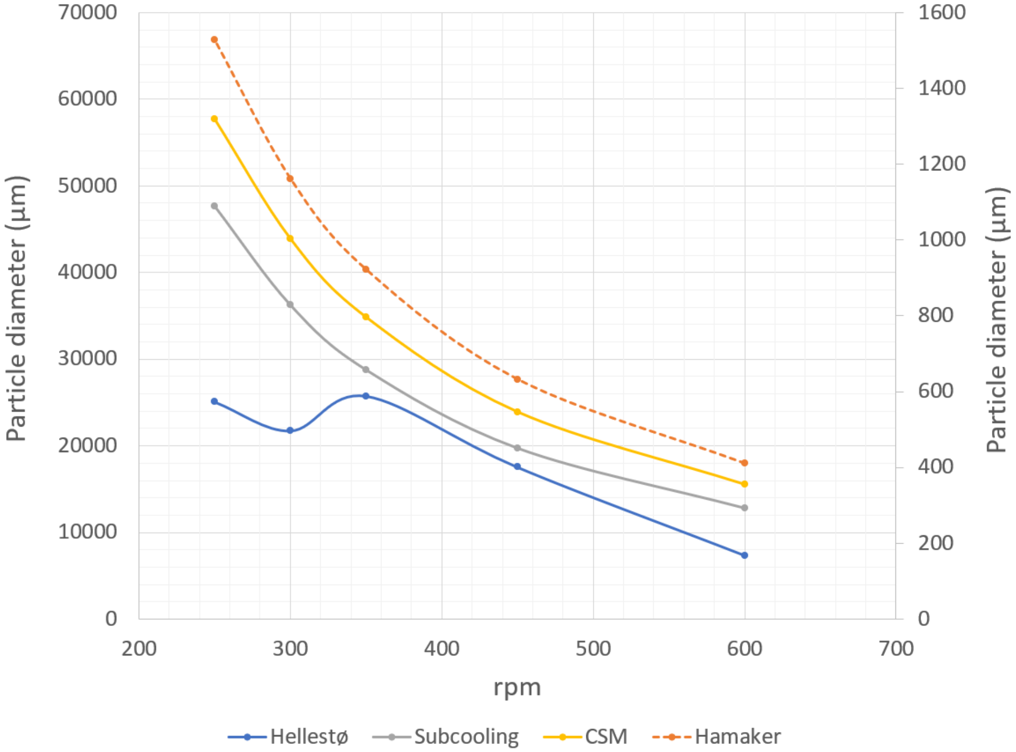

Figure 41: A plot showing the particle diameter size for different stirring rates for the different methods used in the analytical analysis. It is a clear trend of decreasing particle size with stirring rate. The dotted Hamaker graph line utilize the alternate y-axis (on the right of the graph window).

6.1.3 Implicit relation for the agglomerate diameter equilibrium

Another approach to determine the particle diameter for different stirring rates is presented by Zerpa et al. [2] and also later stated and slightly altered by Balakin et al. [32]. This rheological model is based on an apparent viscosity concept. It is assumed that the viscosity of the hydrate particle-liquid slurry follows the rheological equation by Snabre and Mills [40]:

$$\mu_r = \frac{1-\phi_e}{\left[1-(\phi_e/\phi_{max})\right]^2}, \tag{63}$$

where μ_r is the ratio of the apparent viscosity of the suspension μ_a, to the liquid phase viscosity μ_o. The maximum packing fraction of the hydrates ϕ_{max} is set to a value of 0.57, which was also used in CSMHyK. Furthermore, ϕ_e is the effective volume fraction of the hydrate agglomerates, where the agglomerates consist of primary particles. [2]. According to Balakin et al. [32], a model that assumes that the liquid is immobilized inside aggregates can be shown as:

$$\phi_e = \phi_{hyd} \left(\frac{d_a}{d_0}\right)^{3-d_f}, \tag{64}$$

where d_0 is the diameter of primary hydrate particles, ϕ_{hyd} is the volume fraction of the primary hydrate particles, d_a is the diameter for the agglomerates and d_f is the fractal dimension of the agglomerates.

Furthermore, according to Balakin et al. [32] and Mühle [50], the maximum agglomarate diameter $d_{a,max}$, is found using the following relation:

$$d_{a,max} = \left[\frac{F_a d_0^{2-d_f}}{\mu_o \gamma}\right]^{\frac{1}{4-d_f}}, \tag{65}$$

where γ is the shear rate and F_a is the adhesive force between hydrate particles.

According to Zerpa et al. [2], if the average size of the hydrate agglomerate d_a, is assumed to be proportional to the maximum size $d_{a,max}$, an implicit relation for d_a^{eq} is achieved:

$$\left(\frac{D_{eq}}{d_0}\right)^{4-d_f} - \frac{F_a\left[1-\left(\frac{\phi_{hyd}}{\phi max}\right)\left(\frac{D_{eq}}{d_0}\right)^{3-d_f}\right]^2}{d_0^2\mu\gamma\left[1-\phi_{hyd}\left(\frac{D_{eq}}{d_0}\right)^{3-d_f}\right]} = 0. \tag{66}$$

This is an expression for the equilibrium agglomerate size. As time passes, agglomeration and break-up processes are balanced by the adhesive force and the disruptive shear force, respectively. Equation (66) express the steady-state particle size after infinite time where these processes have occurred [32].

If the fractal dimension d_f, is set to 3, equation (66) becomes rather straightforward to solve. However, this gave too large values for the particle diameter, and therefore will not be presented here. Instead, the fractal dimension value was changed to 2.5, and the procedure, shown by Balakin et al. [32], for solving the equation was followed as described in the appendix.

Table 15 shows the different values and parameters used for this method.

Table 15: Parameters and their values for this calculation method of the particle mean diameter.

Parameter	Symbol	Value	Unit
Primary Particle Size	D_0	$8.00 \cdot 10^{-6}$	m
Fractal Dimension	d_f	2.50	
Dynamic Viscosity	μ	$1.72 \cdot 10^{-3}$	$\mathrm{Pa} \cdot \mathrm{s}$
Hamaker Constant	A	$4.59 \cdot 10^{-21}$	J
Particle Separation Distance	z	$9.30 \cdot 10^{-10}$	m
Roughness	d_{nuclei}	$3.40 \cdot 10^{-10}$	m
Mean Free Path	h	$2.50 \cdot 10^{-10}$	m
Adhesive Force Hamaker	F_a	$1.77 \cdot 10^{-9}$	J/m
Maximum packing fraction of hydrate particles	ϕ_{max}	0.57	

Values for shear rate γ, and volume fraction ϕ_{hyd}, for different stirring rate are collected in table 12. The value of the adhesive force F_a, is found with the Hamaker approach, which can be seen in equation (61). The value of Hamaker constant A is from Bonnefoy et al. [49].

The result of the particle size diameters using this implicit relation method is showed in table 16 for the different stirring rates.

Table 16: Particle diameter for different stirrer rates from equation (66).

Stirrer Rate [rpm]	Particle Diameter D_{eq} [μm]
600	29.66
450	34.30
350	38.90
300	42.99
250	46.00

The experimental results from Herri et al. [1] illustrated in table 9 and figure 38 clearly show that higher stirring rates result in increasingly larger particle diameter. On the other hand, it is also clear from the expression shown by Zerpa et al. [2] and Balakin et al. [32], that higher stirring rates result in a decreasing particle diameter.

It is clear that these results for the particle diameter is in coherence with the experimental results from Herri et al. [1]. However, a crucial difference is that these two set of result are opposite of each other as figures 38 and 42 show.

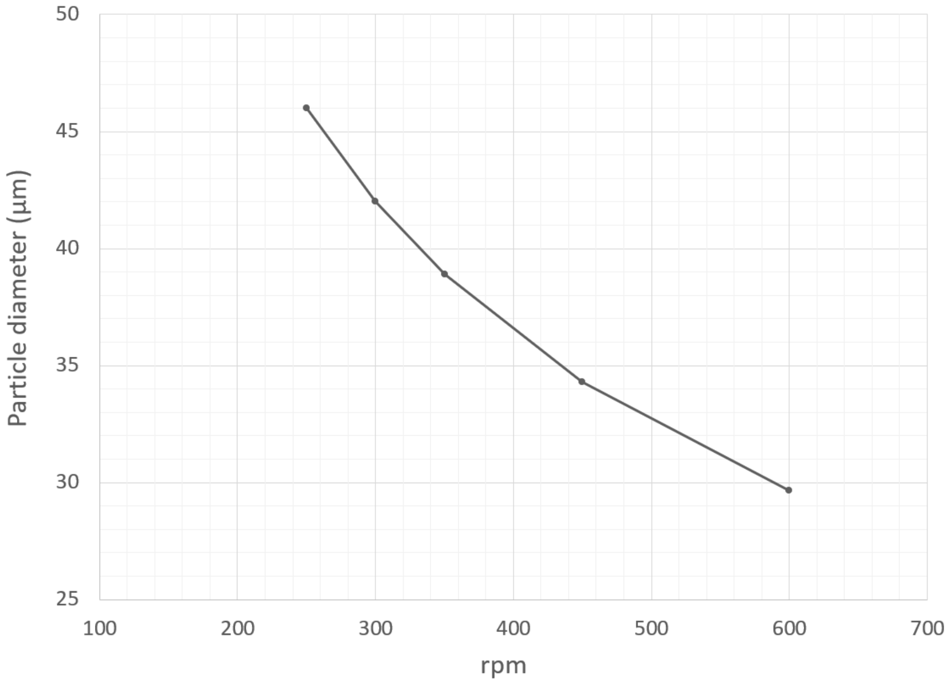

Figure 42: The graph shows the results from the Zerpa equation (66) for the different stirring rates. A clear trend of decreasing particle diameter size with stirring rate.

6.2 Simulations of the particle size distribution in the tank

A volume average plot of the particle diameter size as a function of time is presented in this section, which corresponds to equation (37). This plot represents the dimensionless diameter for the particle, more specifically $d/d0$. This is done due to a large difference in initial particle diameter size for each stirring rate, which ensures clear plots. Visual snapshots giving an overview of the distribution of the particle size in the tank, velocity profiles and streamlines for the continuous phase are presented as well.

In this thesis, numerical simulations of the particle size distribution in a tank were conducted for several stirring rates using a 5-phase CFD model, and compared qualitatively with the studies carried out by Herri et al. [1]. Their work suggests that the particle diameter size increases with stirring rate. The aim is to investigate the mechanisms, which govern the granulometry of a liquid-solid system. The distribution of the slurry flow will develop and disperse due to turbulent diffusion as time progresses. Due to lack of detailed information about the exact measurement location in the tank from the experiments of Herri et al. [1], Herri provided additional information about this issue in a private communication. Pic [46] did experiments with a turbidity sensor and the location of this sensor can be seen in figure 43. Therefore, an adequate location that corresponds to the sensor in figure 43 to measure the average particle diameter size in the tank is at the top probe line, which is shown in figure 59. The initial values of the hydrate volume fractions for the different stirring rates can be seen in table 8, which are average values from the experiments of Herri et al. [1]. The location for the initial hydrate volume fraction is shown in figure 28.

A plot of the dimensionless particle diameter $d/d0$ for the different stirring rates can be seen in figure 44, which corresponds to the location of the sensor in the experiments of Herri et al. [1]. Figure 45 shows the same plot, but measures for the whole tank. Both plots correspond to equation (37). Although, these plots were yet to fully converge, hence the simulations for the 5-phase CFD model were not completed, therefore it would be speculation to discuss these results before convergence is achieved. Nevertheless, a theory will be presented in the following. As shear rate and stirring rate are low, the hydrates stay preferably at the water-gas interphase due to buoyancy. Increasing the stirring rate, the largest and most inertial particles are transported upwards to the sensor location, where the mean size grow. At high rpm, the slurry becomes homogeneous, which results in a decrease in the particle mean size. However, if this concept preserves in the terminal condition, the expected outcome of the particle diameter-rpm plot would be a ”bell” shaped curve, first growing up to a maximum and then reduce back to around unity. Now, the measurements from Herri et al. [1] could be influenced by the left branch of the ”bell”.

Figures 46 - 50 show the distribution of the average particle diameter in the tank at the different stirring rates. The average particle diameter is largest in the top area of the tank for every stirring rate configuration.

Snapshots of the hydrate volume fraction distribution combined with the velocity vector profile of the continuous phase in the tank at 600 rpm can be seen in figures 51 - 54. Eddies can be seen in the bottom corners of the tank, as well as in both sides around the impeller area near the wall.

The water volume fraction distribution is shown in figure 55, and less water relative to the hydrate phase can be found directly underneath the impeller towards the bottom of the tank.

Streamlines of the hydrate phase in the tank for 600 rpm can be seen in figure 56. This illustrates how the hydrate particles disperse in the tank in time.

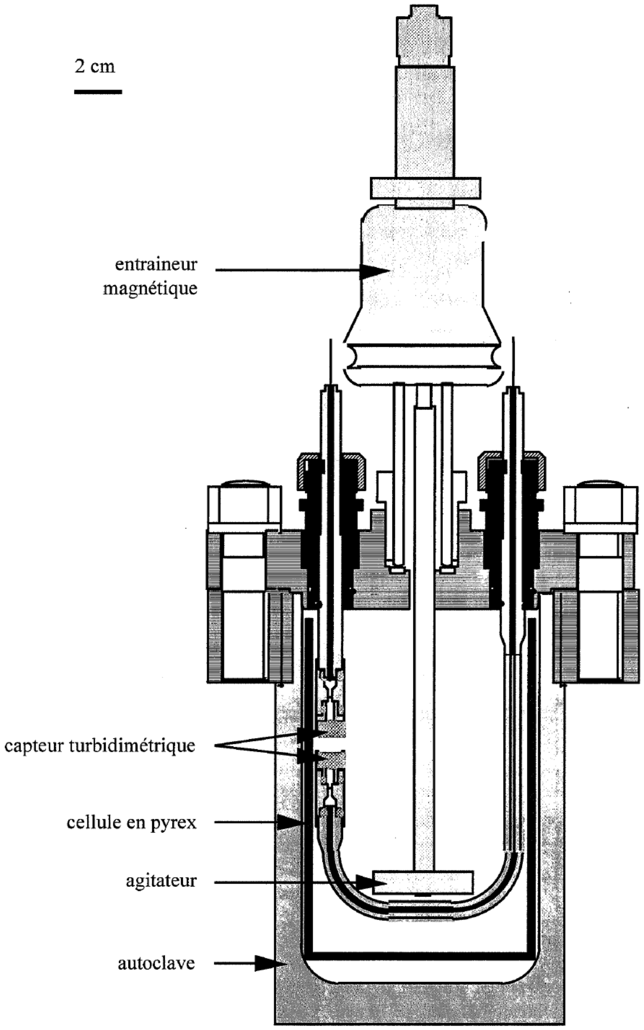

Figure 43: Illustration of the location of the sensor that measures the particle size in the tank [46].

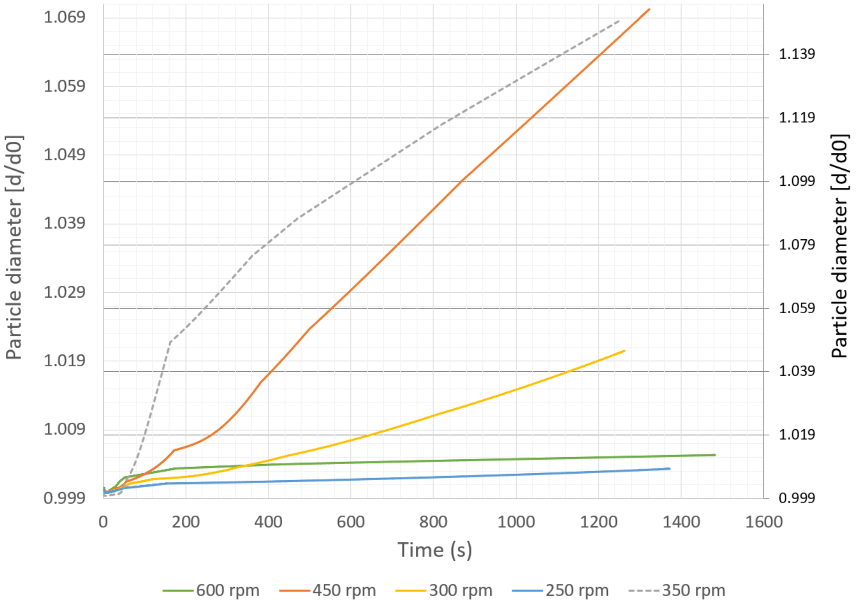

Figure 44: 5-phase CFD model: Particle diameter ($d/d0$) for the stirring rates, location of measure is from Herri et al.[1].

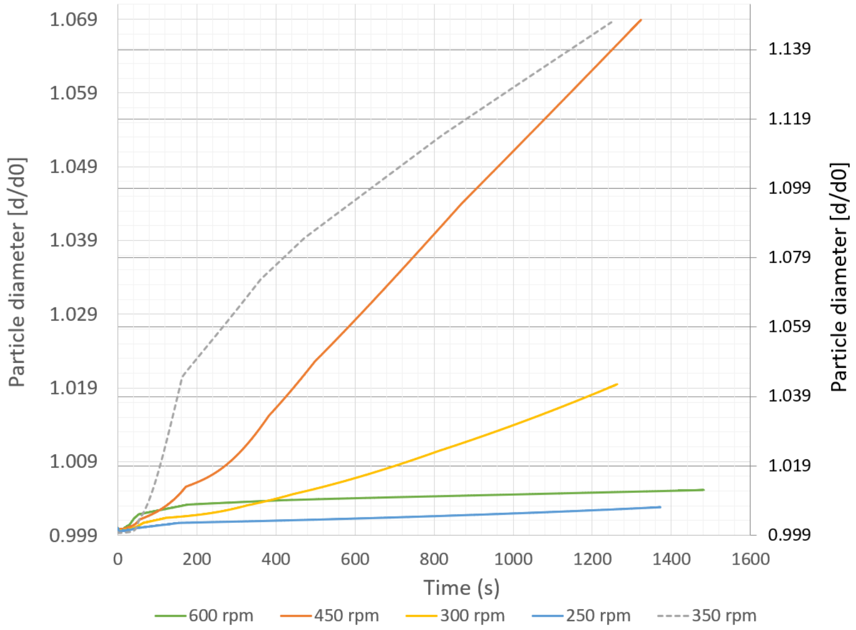

Figure 45: 5-phase CFD model: Average particle diameter ($d/d0$) for the stirring rates, measured for the whole tank.

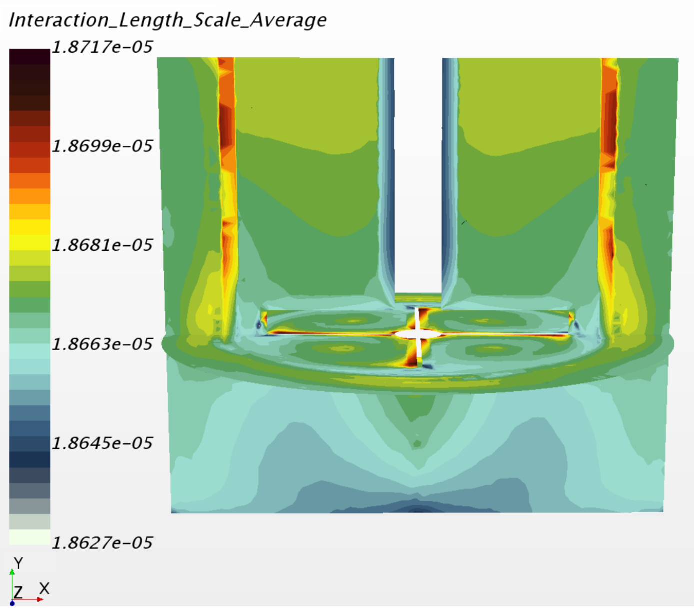

Figure 46: 5-phase CFD model: Average particle diameter distribution: 600 rpm.

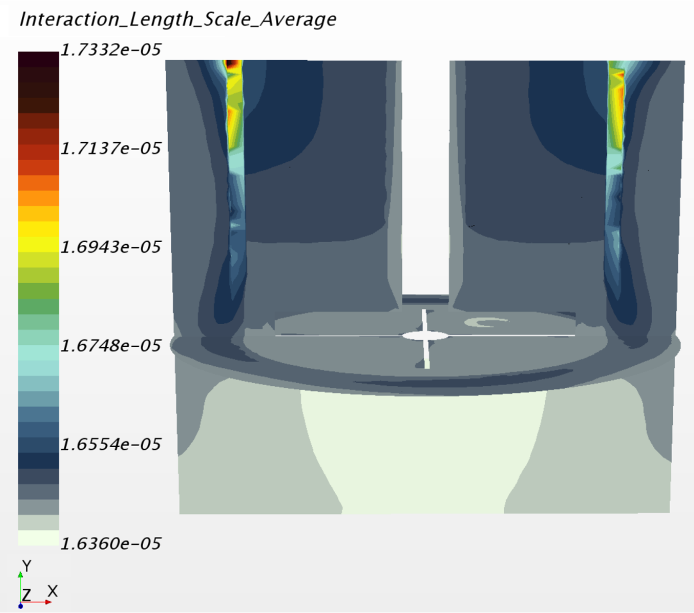

Figure 47: 5-phase CFD model: Average particle diameter distribution: 450 rpm.

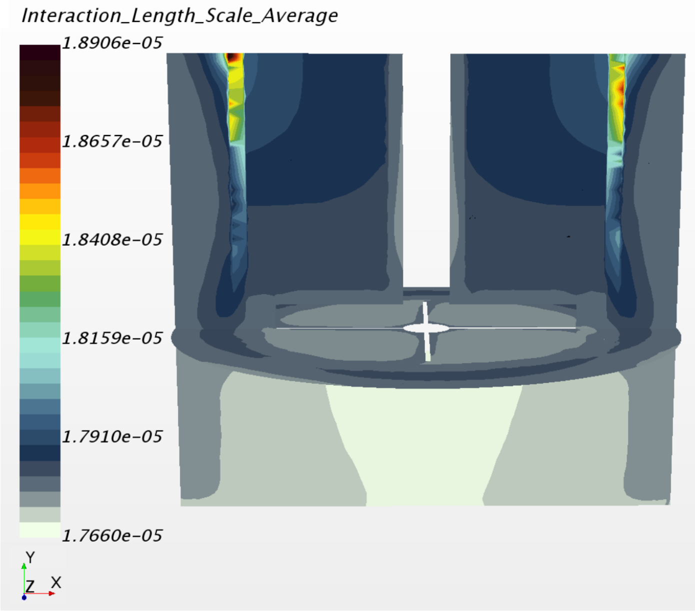

Figure 48: 5-phase CFD model: Average particle diameter distribution: 350 rpm.

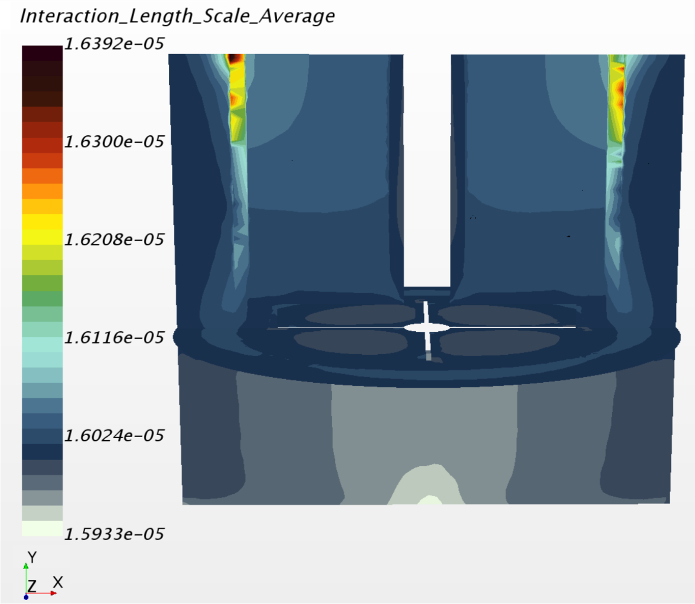

Figure 49: 5-phase CFD model: Average particle diameter distribution: 300 rpm.

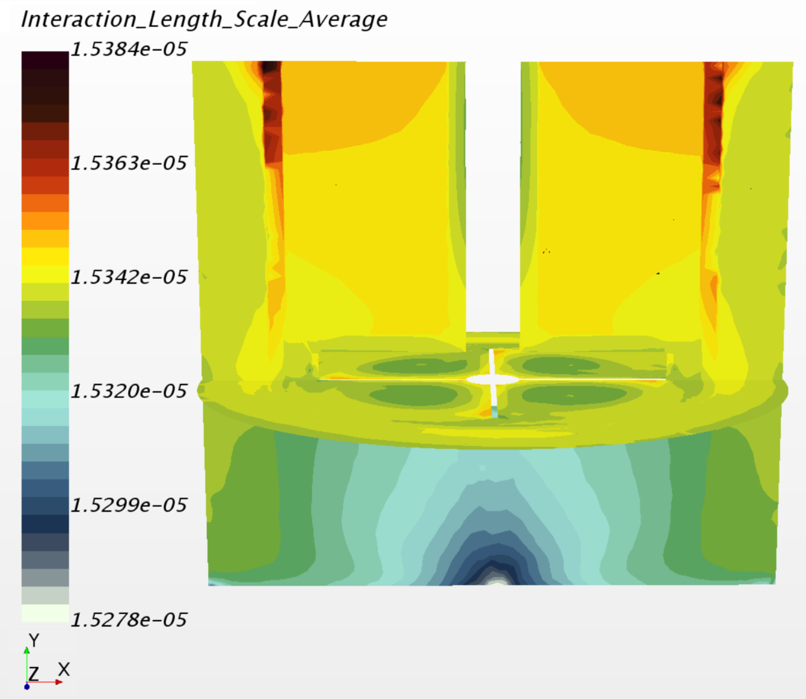

Figure 50: 5-phase CFD model: Average particle diameter distribution: 250 rpm.

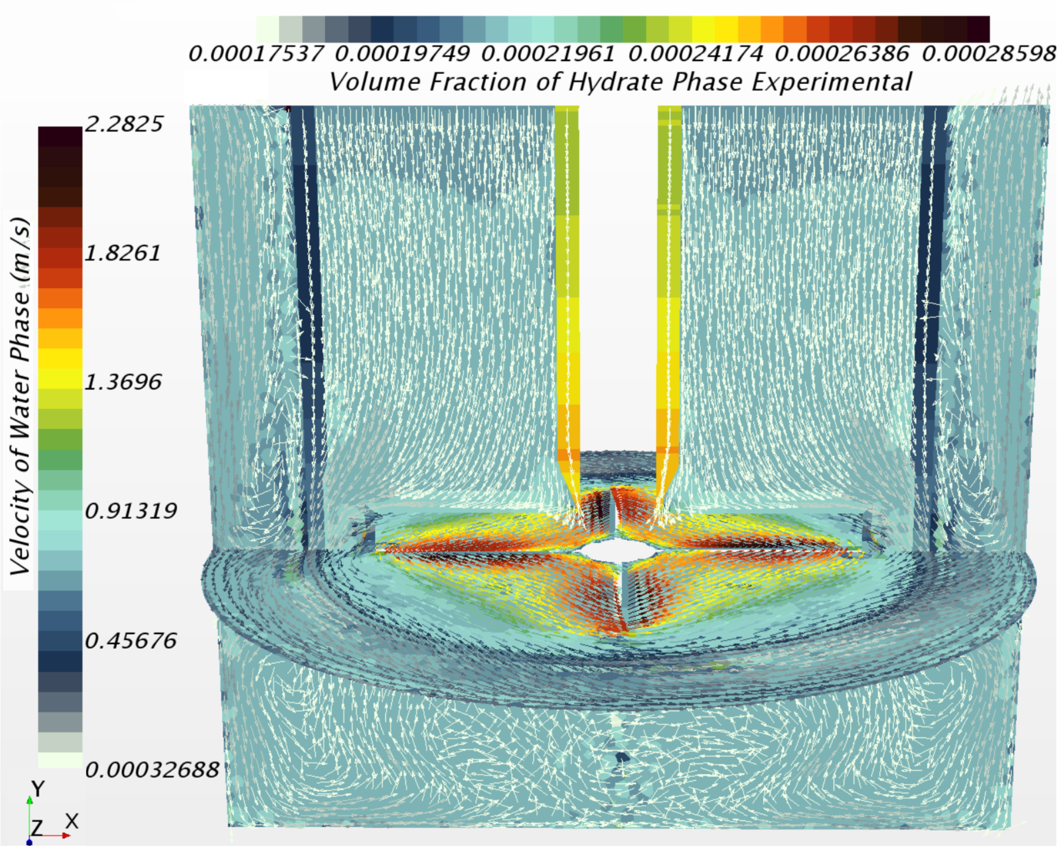

Figure 51: 5-phase CFD model: Hydrate volume fraction distribution combined with velocity profile for the water phase in the tank at 600 rpm. Front view of the tank, including impeller. The fluid is transported downwards to the bottom, and eddies are located in the bottom corners.

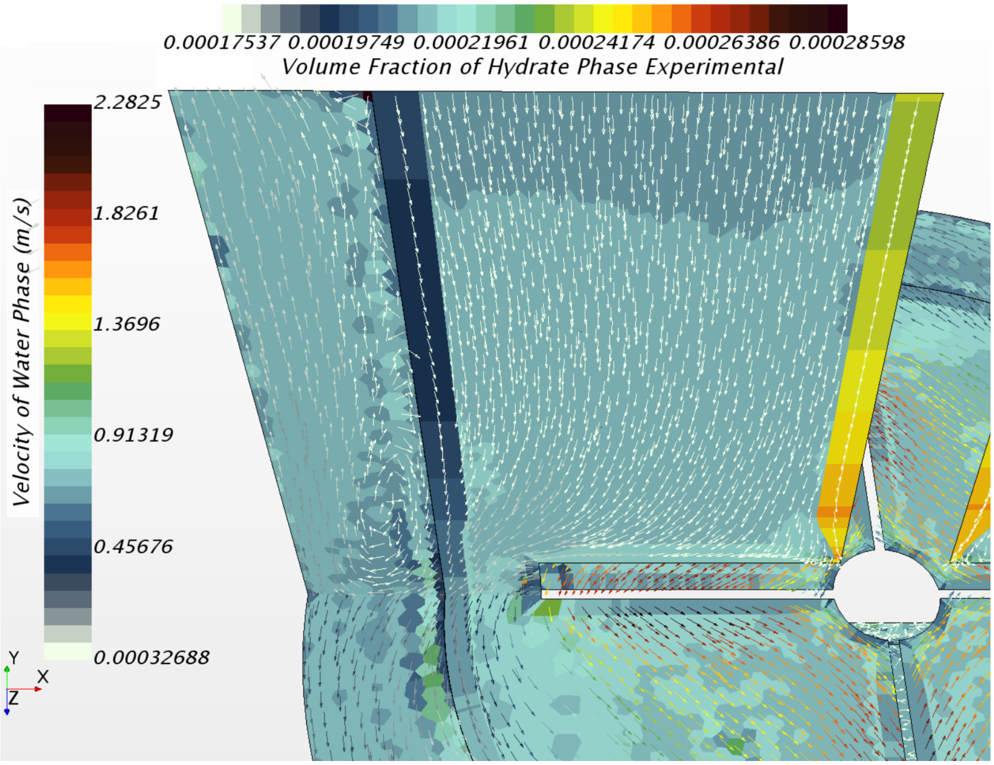

Figure 52: 5-phase CFD model: Hydrate volume fraction distribution combined with velocity profile for the water phase in the tank at 600 rpm. Close-up snapshot of the transition from the stationary- to the rotating region.

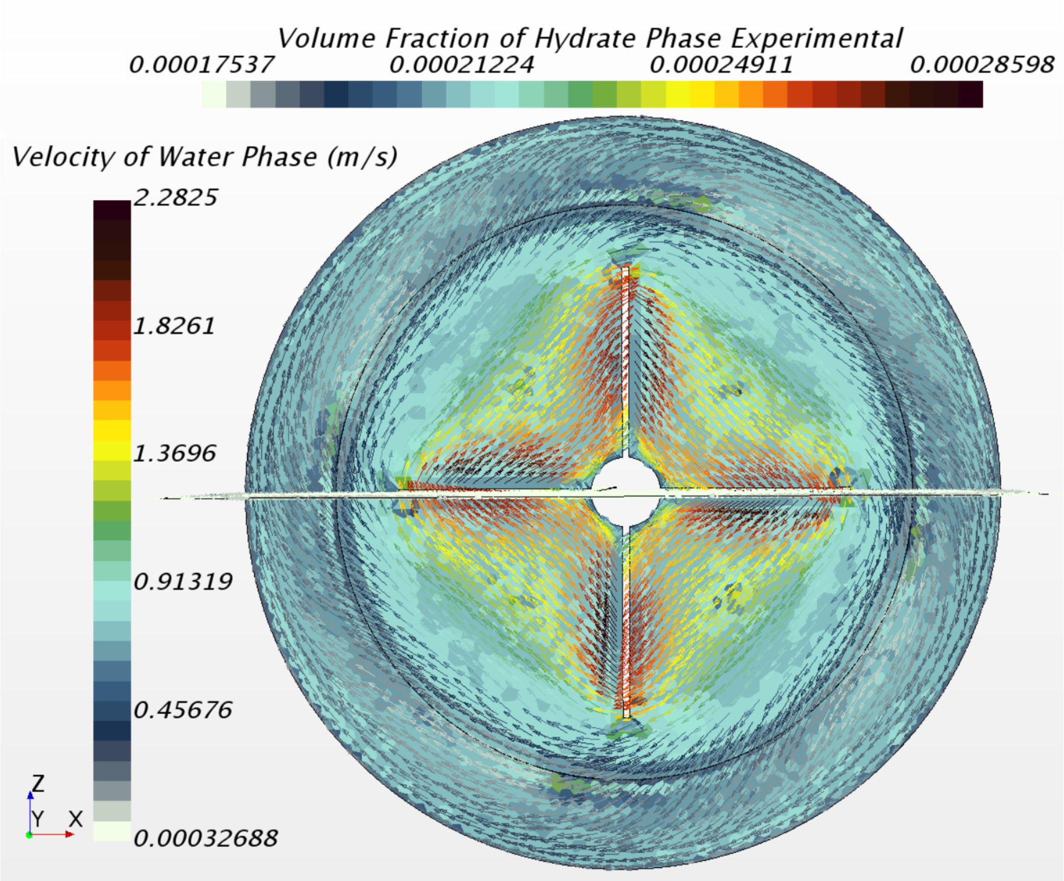

Figure 53: 5-phase CFD model: Hydrate volume fraction distribution combined with velocity profile for the water phase in the tank at 600 rpm. Top view of the impeller.

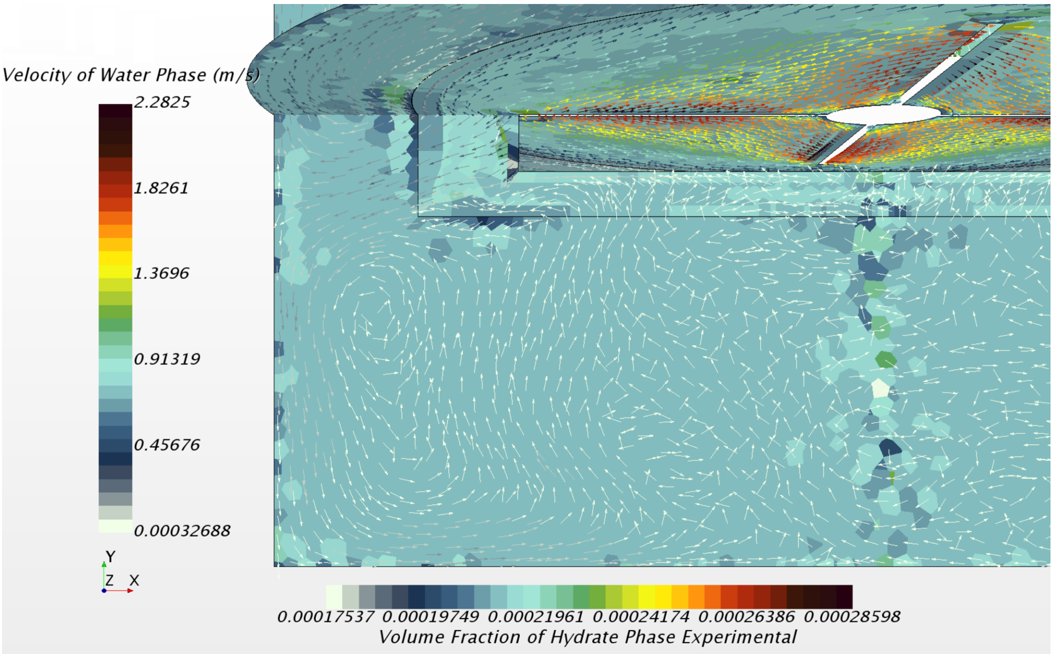

Figure 54: 5-phase CFD model: Hydrate volume fraction distribution combined with velocity profile for the water phase in the tank at 600 rpm. Eddies are located in the bottom corner.

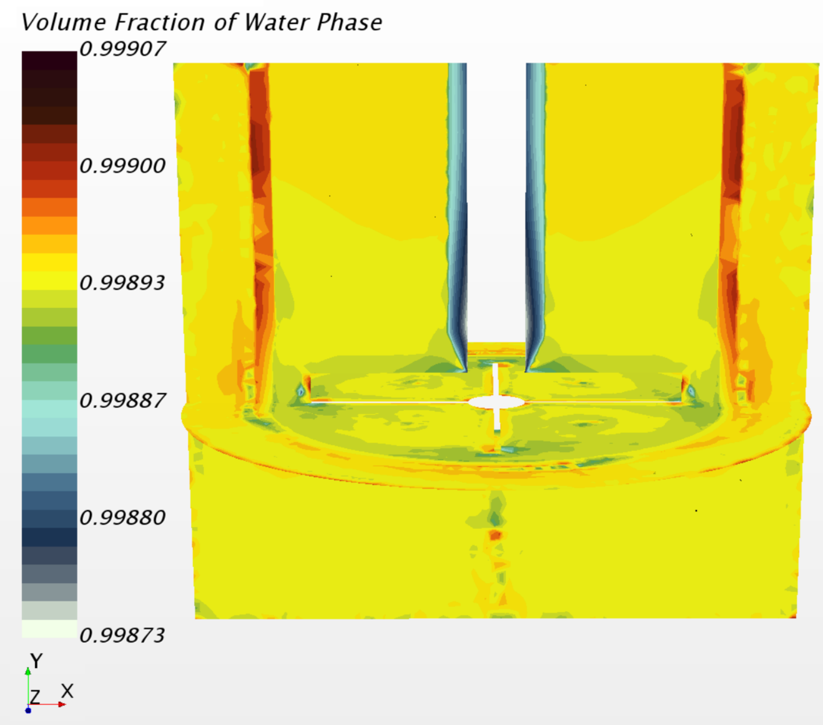

Figure 55: 5-phase CFD model: Volume fraction distribution of the water phase for 600 rpm.

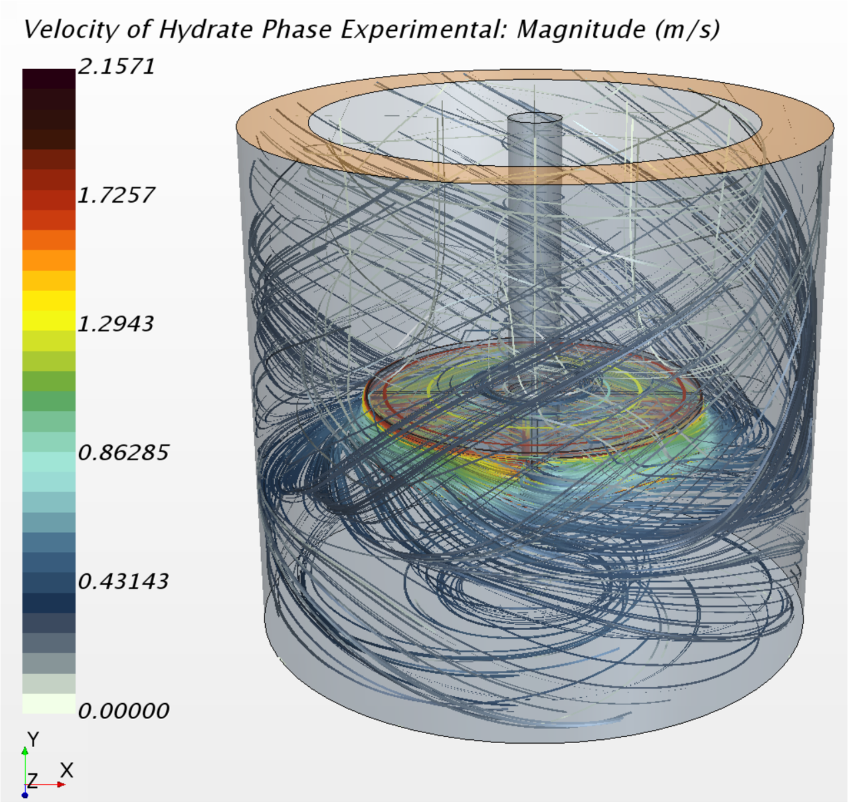

Figure 56: 5-phase CFD model: Hydrate phase streamlines distribution for 600 rpm.

6.3 Mesh independence and simulation validation

Mesh independence was controlled for validation of the simulations. This was done by measuring the velocity as a function of position inside the tank. This was made possible by inserting probe lines across the tank at three different locations, which can be viewed in figure 59. The values of y+ needs to be addressed, and to achieve a decent computational time for analytical solutions, this value should either be under 5 or over 30. This was considerably beneficial since time consuming simulations took place. Mesh independence is introduced to find a balance between adequate values of y+, but also a compatible mesh detail level, especially for the rotating region where small parts are located. As a result of this, the use of surface wrapper and prism layer models are used. The $\kappa - \omega$ model was used for the flow validation, while the $\kappa - \epsilon$ model was used to gather the y+ values for both regions. Both models are described in section 4.2.

Table 17: Mesh thickness for the two regions

Region	Fluid	Rotation
Thickness (mm)	4.00	3.00
	3.00	3.00
	1.50	3.00
	1.50	1.50
	1.00	1.00
	0.75	0.75

Table 17 shows the selected values of thickness of the mesh in both regions. Figure 57 show the generated mesh in the rotating region. This mesh configuration is well balanced with a base size of 1.5 mm both in the rotating- and the fluid region. It is clear from the figure that even small parts in the rotating region are meshed successfully without any artefacts.

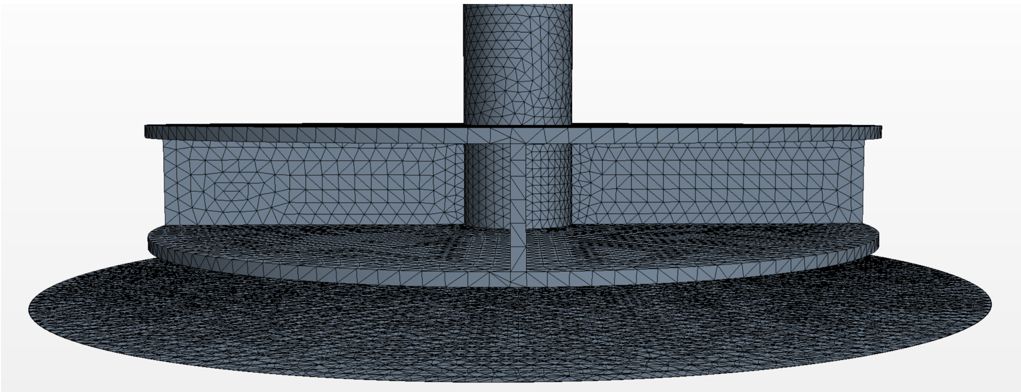

Figure 57: Mesh of the rotating region with a base size of 1.5 mm. It is clear that this mesh configuration provides adequate detail level without any artefacts or irregularities.

Table 18: Y+ values for the rotating region with different mesh thickness.

Report	4/3	3/3	1.5/3	1.5/1.5	1/1	0.75/0.75	(mm)
Y+ [Rotation]	18.07	18.10	18.04	10.59	8.41	5.63	

The result of the mesh independence is shown in table 18, and it is clear that the y+ values are not satisfying. To solve this issue, the case where the mesh size is 1.5 mm in both regions was chosen. Furthermore, one prism layer was introduced to the mesh model in the rotating region. This is set to 200 % relative to the base size and therefore 3 mm in absolute size. This prism layer is more coarse and should therefore increase y+ values, and also enables the solver to resolve near wall flow accurately. From this, figure 58 show sufficient and satisfying y+ values in the rotating region near the impeller since the value of y+ is over 30. It is clear that higher stirring rates gives higher y+ values.

6.3.1 Validation of the model

Probe-lines placed in the tank that can extract different types of information are used to validate the flow pattern in the model. It was also of interest to compare these flow patterns to each other for the different mesh thickness combinations, and see how these change the flow pattern. The velocity as

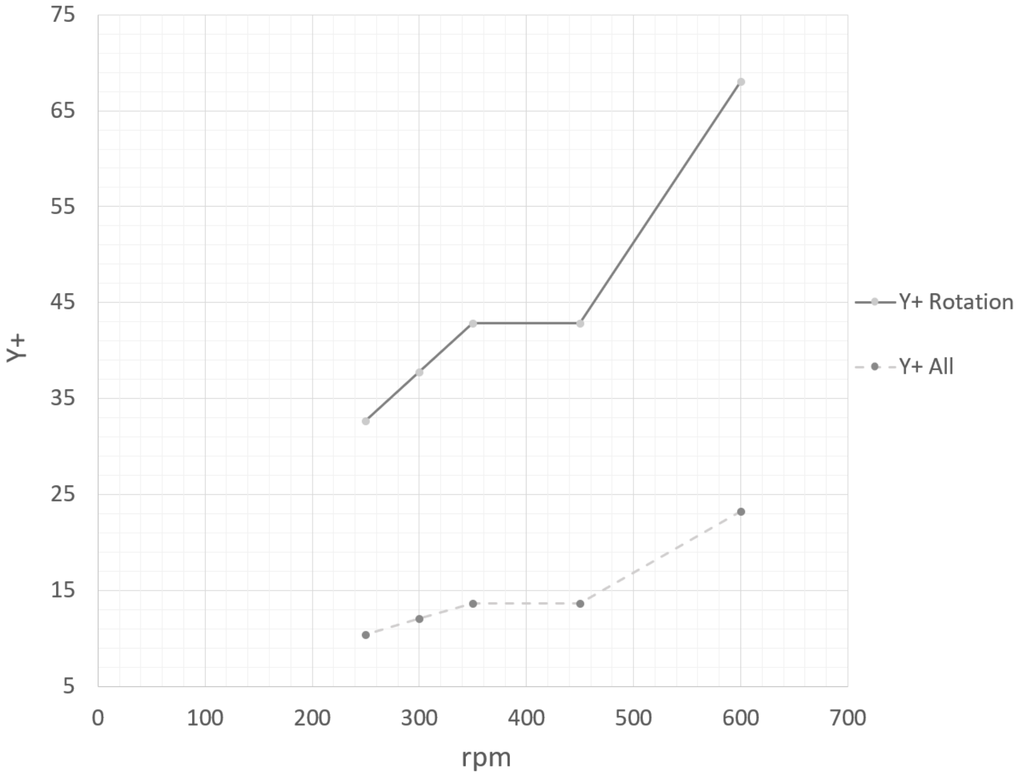

Figure 58: Satisfying y+ values with one prism layer.

a function of position was measured and compared, and as figure 59 shows, these probe-lines were placed in the top and bottom of the tank, as well as in the impeller area. The results for the impeller area are presented in figure 60, which shows the velocity as a function of position for different mesh thickness. The best option is the mesh with 1.5 mm in both regions, which has a very small variation relative to the other meshes. This gives a good balance among the tested meshes.

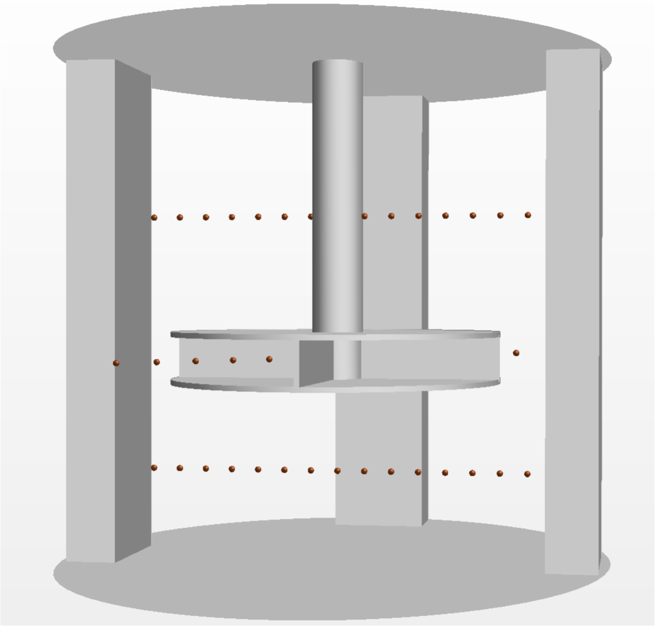

Figure 59: Location of probe-lines.

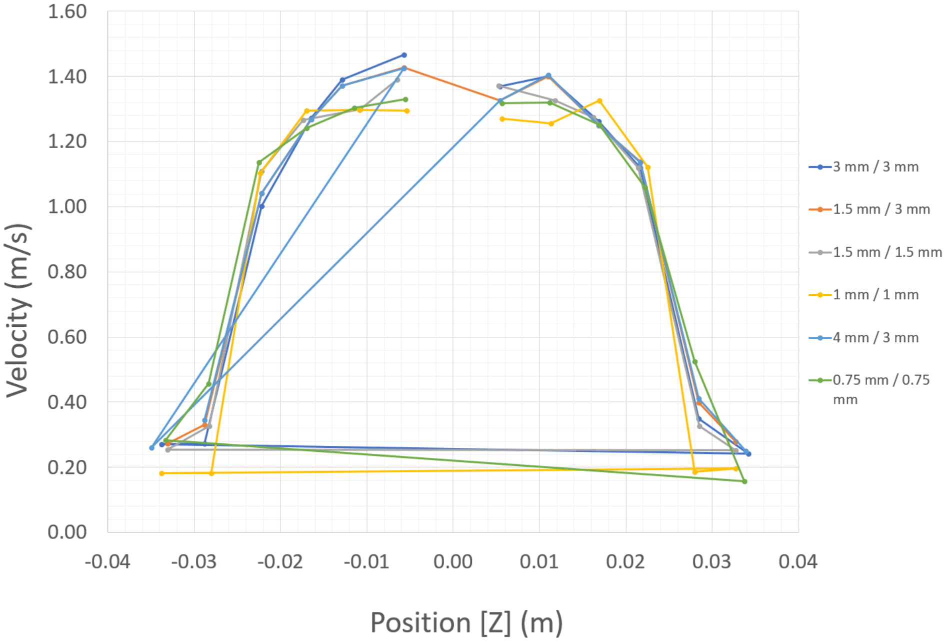

Figure 60: Velocity development as a function of position for different mesh thickness.

6.4 Simulations of particle growth using the CFD-PBM technique

In this thesis, simulations of the particle growth due to chemical interactions in the tank were conducted for several stirring rates. The numerical simulations using the 2-phase CFD-PBM model have completed and all of the plots are therefore converged. For the different stirring rates, plots of the particle diameter, which correspond to equation (48), are presented in this section. Snapshots of the particle- as well as the volume fraction distribution of the dispersed phase in the tank are provided. Volume fraction distribution of the hydrate phase combined with velocity vectors of the continuous phase, as well as velocity profiles and streamlines for the continuous phase are also included.

6.4.1 Particle growth

The history of particle diameter for the different stirring rates is shown in figure 61. This figure shows a larger particle diameter for lower stirring rates. A possible explanation could be at a lower stirring rate, more particles are located in the top area of the tank, and since both the concentration of methane and growth rate are largest at this area, particles may grow bigger around the top boundary. However, there are no such effects in the model from Herri et al. [1] to support this, since they did not simulate in three-dimensions. Illustrations of the concentration of methane and growth rate distribution in the tank can be seen in figure 63 and 64, respectively.

However, results of the simulation model done by Herri et al. [1], which can be seen in figure 33, compared to the results of the 2-phase CFD-PBM model in this thesis, show an opposite trend. Herri et al. [1] presented, from their simplified model of primary nucleation/growth, an increasing particle diameter size with stirring rate. On the other hand, the results from the 2-phase CFD-PBM model seen in figure 61 show a decreasing particle diameter size with stirring rate.

Figure 61 also shows a decrease in particle diameter. After some time, the particle diameter for all the stirring rates evenually converge, and the graphs flatten out. This reduction may be due to reconstruction of velocity and volume fraction profiles when the particles finally have grown to a certain size. According to Vaziri et al. [51], starting with a suspension of primary

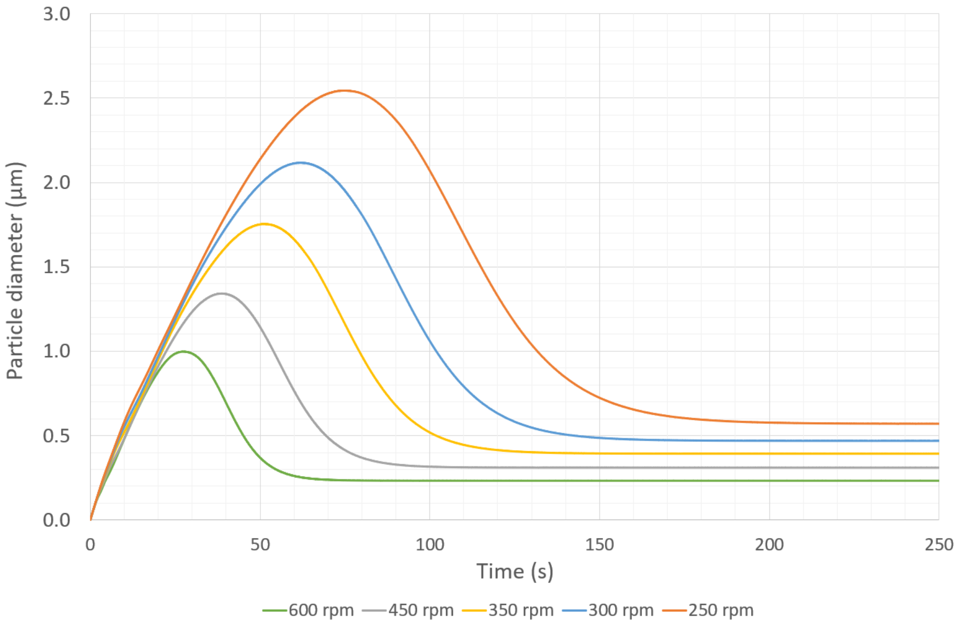

Figure 61: 2-phase CFD-PBM model: Hydrate particle diameter for different stirring rates. Lower stirring rates yields larger particle diameter size.

particles, the average cluster size may first increase to a maximum before a relaxation event sets in, which can be seen in figure 62. Furthermore, the reduction in size is linked to migration of the hydrate phase at start up. Vaziri et al. [51] found out that deposition, or migration, of the solid phase could lead to this size reduction pattern shown in figure 61.

However, the results from the 2-phase CFD-PBM model do not seem to be in a qualitative agreement with Herri et al. [1]. The quantitative agreement was also not obtained due to difficulties comparing the model from Herri et al [1] to the CFD-PBM model used in this thesis.

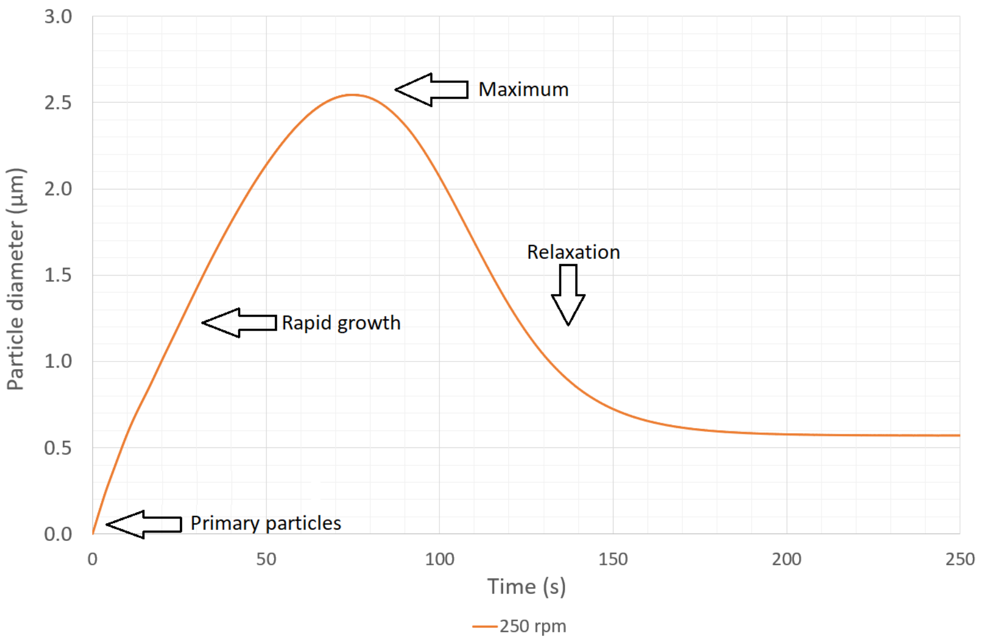

Figure 62: 2-phase CFD-PBM model: A suspension of primary particles grows rapidly, reach maximum, and eventually relaxation sets in. This is from the result of particle size diameter simulation at 250 rpm.

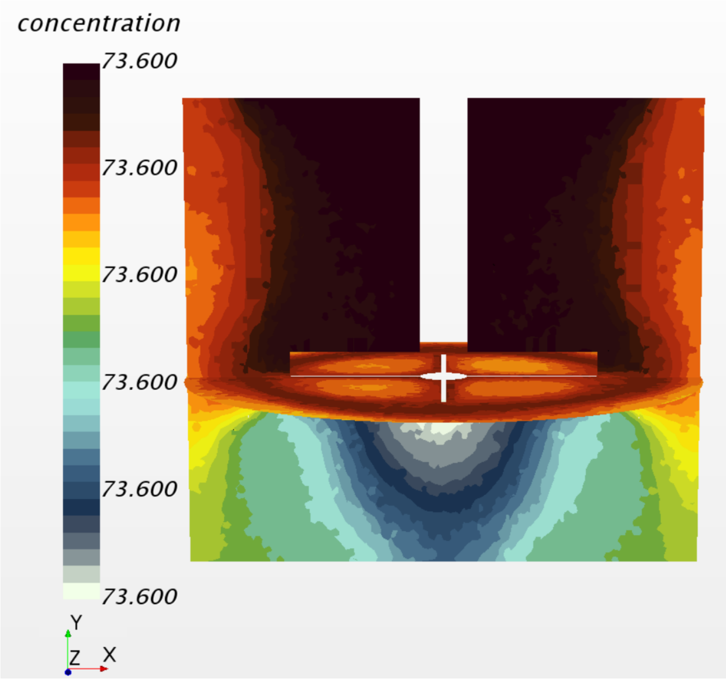

Figure 63: 2-phase CFD-PBM model: Concentration of methane distribution in the tank.

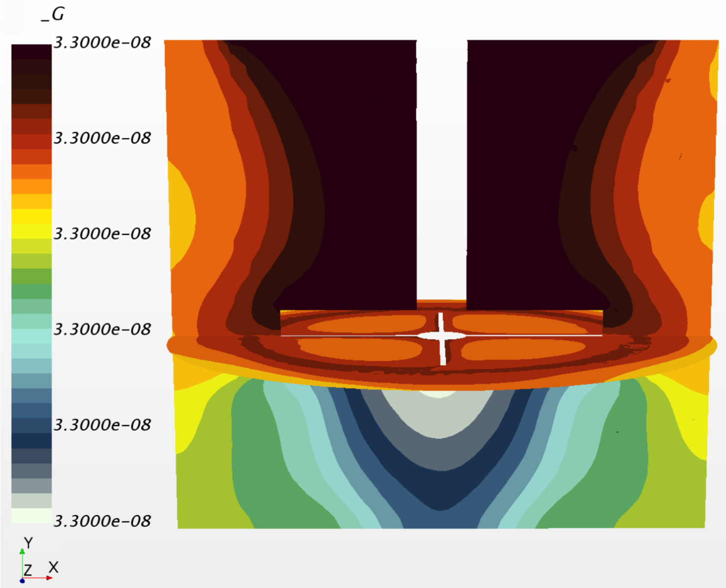

Figure 64: 2-phase CFD-PBM model: Growth rate distribution in the tank.

The development of the volume fraction of the hydrate phase for the different stirring rates is shown in figure 65. The hydrate volume fraction ϕ_d, increases with stirring rate as time progresses. A possible explanation could be that the quantity and size of the hydrate phase increase more rapidly with more small-sized particles that are present in the tank since they are more in contact with the gas. This also leads to a quicker conversion to gas hydrates. However, no data from Herri et al. [1] can be found to support this statement.

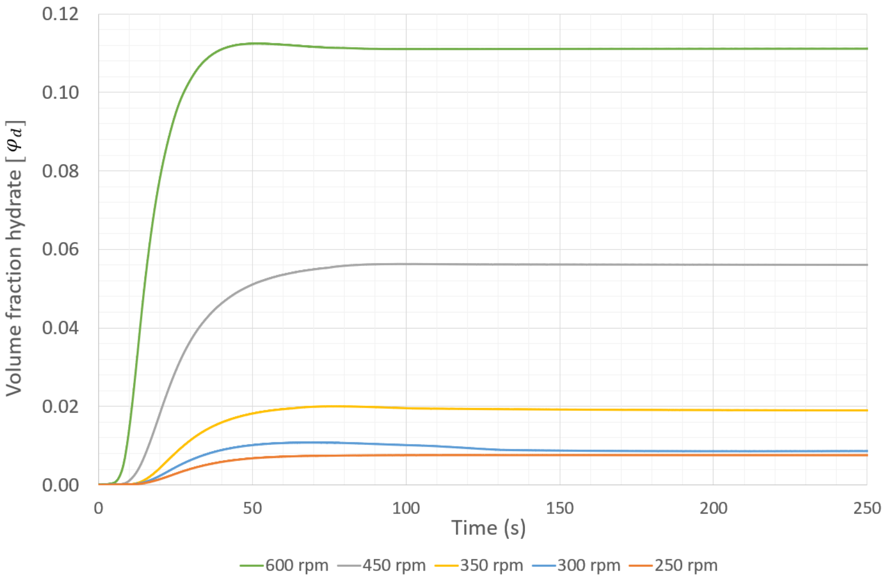

Figure 65: 2-phase CFD-PBM model: Volume fraction development of the hydrate phase at different stirring rates.

The distribution of the particle diameter in the tank for the different stirring rates can be seen in figures 66 - 70, where the stirring rate ranges from 600-250 rpm.

The distribution of volume fractions for the hydrate phase combined with velocity vector profiles for the water phase at 600 rpm is shown in figures 71 - 74. However, it is clear that the volume fraction of the hydrate phase is in correlation with concentration and growth rate profiles, which can be seen in figures 63 and 64. Nevertheless, the velocity vectors show that the impeller transports the fluid in a downwards motion, which can explain the accumulation location of the particles towards the bottom of the tank seen in figures 66 - 70. In addition, the volume fraction distribution of the water phase at 600 rpm can be seen in figure 75.

Figure 76 shows a scalar scene of the velocity distribution of the water phase in the tank for 600 rpm. In addition, streamlines of the hydrate phase velocity in the tank for 600 rpm was produced to give an illustration of how the dispersed phase develops with time, and is shown in figure 77.

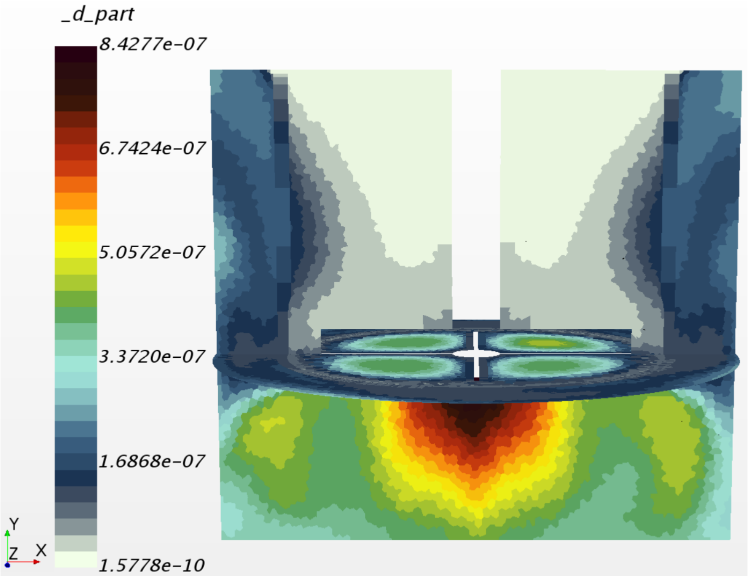

Figure 66: 2-phase CFD-PBM model: Particle diameter distribution in the tank for 600 rpm.

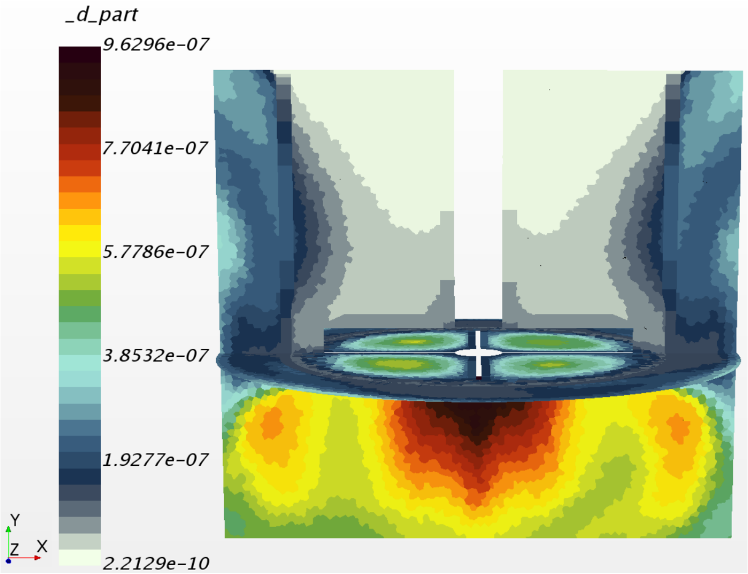

Figure 67: 2-phase CFD-PBM model: Particle diameter distribution for 450 rpm.

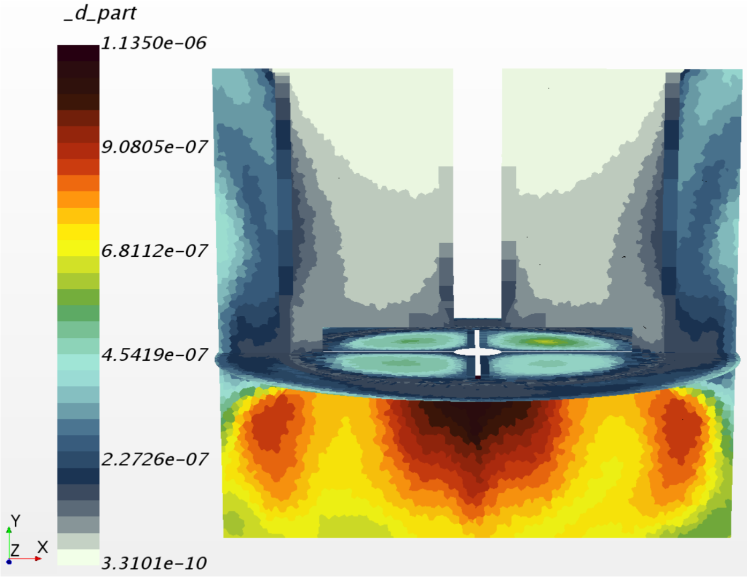

Figure 68: 2-phase CFD-PBM model: Particle diameter distribution in the tank for 350 rpm.

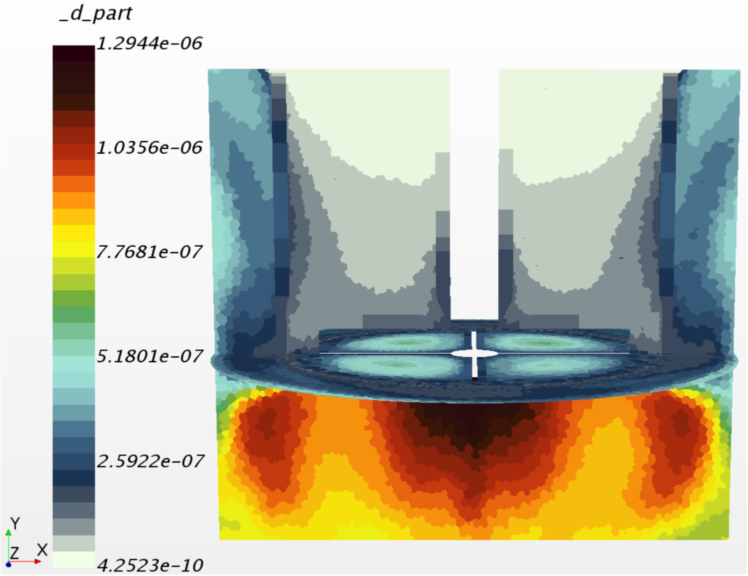

Figure 69: 2-phase CFD-PBM model: Particle diameter distribution for 300 rpm.

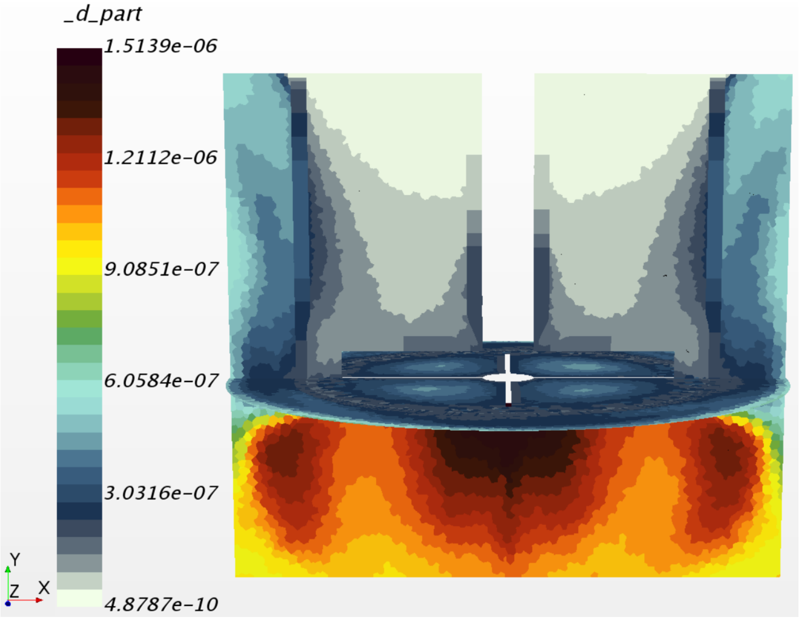

Figure 70: 2-phase CFD-PBM model: Particle diameter distribution in the tank for 250 rpm.

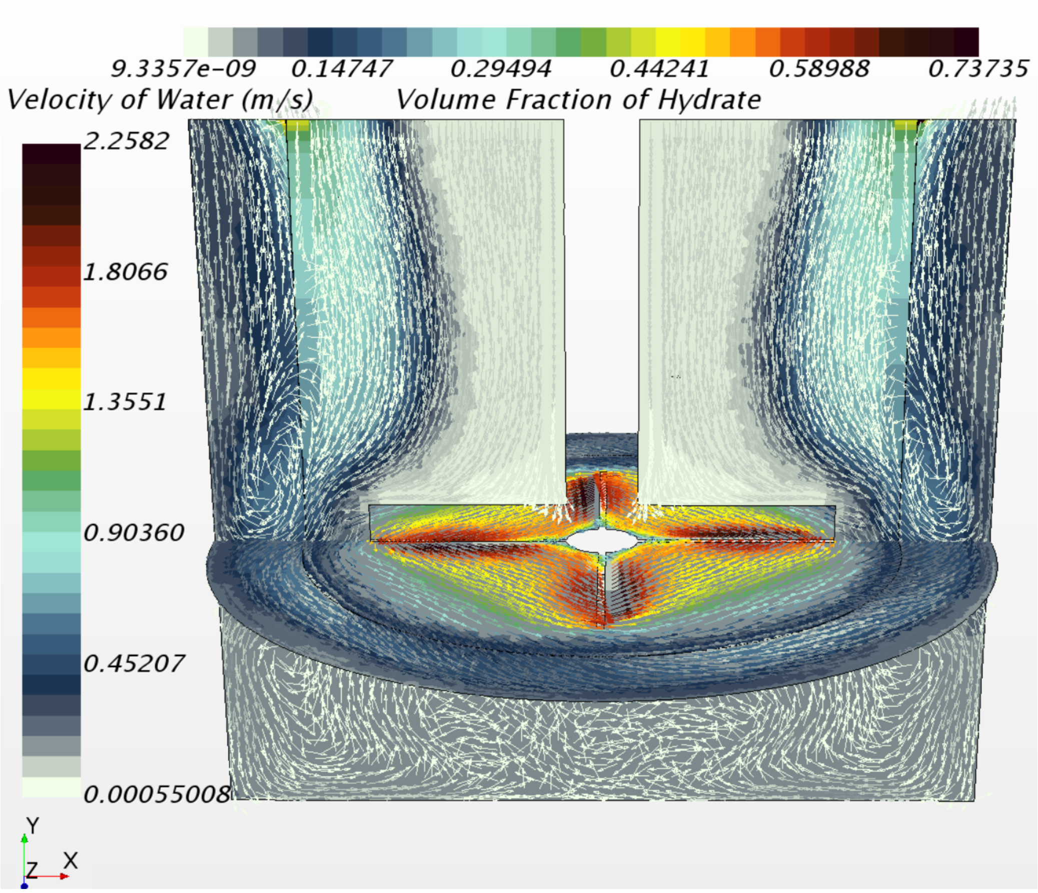

Figure 71: 2-phase CFD-PBM model: Volume fraction distribution of hydrate particles combined with velocity vector profile of the water phase at stirring rate 600 rpm. Front view of the tank, including the impeller.

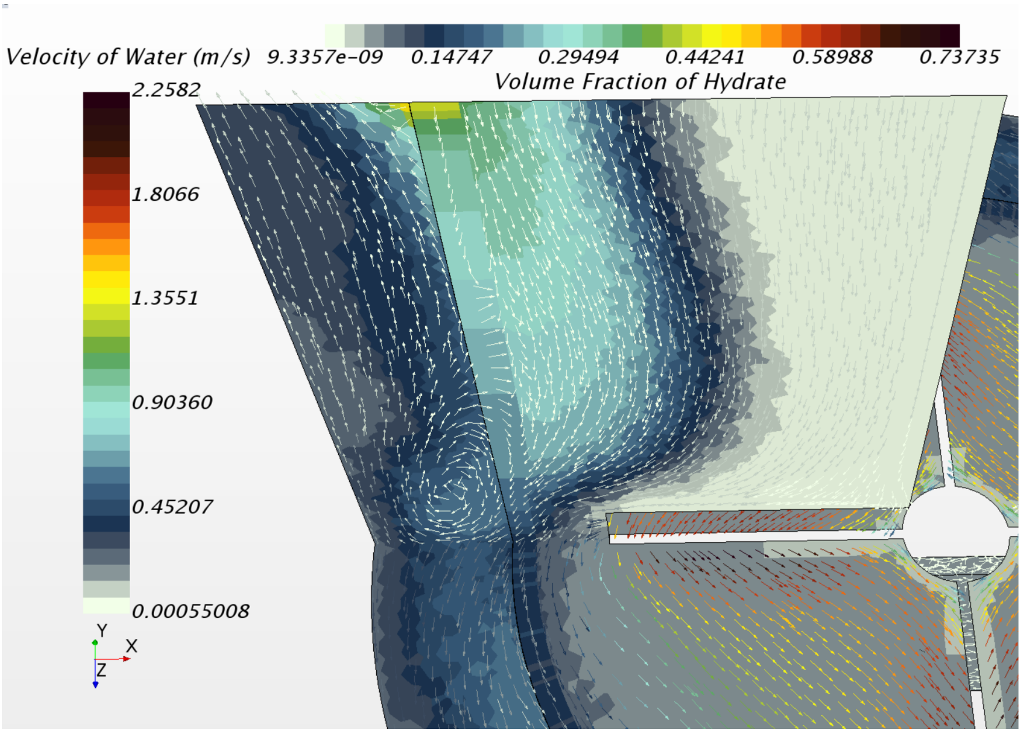

Figure 72: 2-phase CFD-PBM model: Volume fraction distribution of hydrate particles combined with velocity vector profile of the water phase at stirring rate 600 rpm. Transition view from the fluid region to the rotating region. The fluid is transported downwards. Eddies can be seen to the left of the impeller.

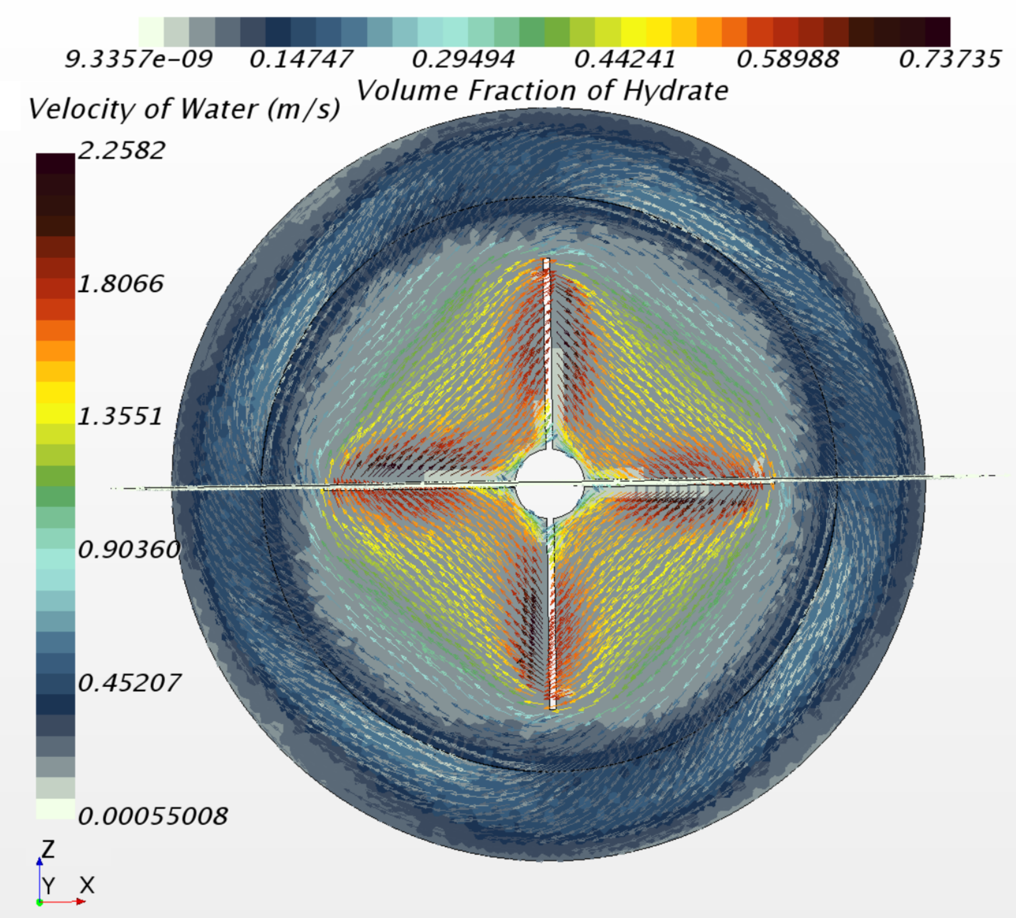

Figure 73: 2-phase CFD-PBM model: Top view of the volume fraction distribution of hydrate particles combined with velocity vector profile of the water phase at stirring rate 600 rpm.

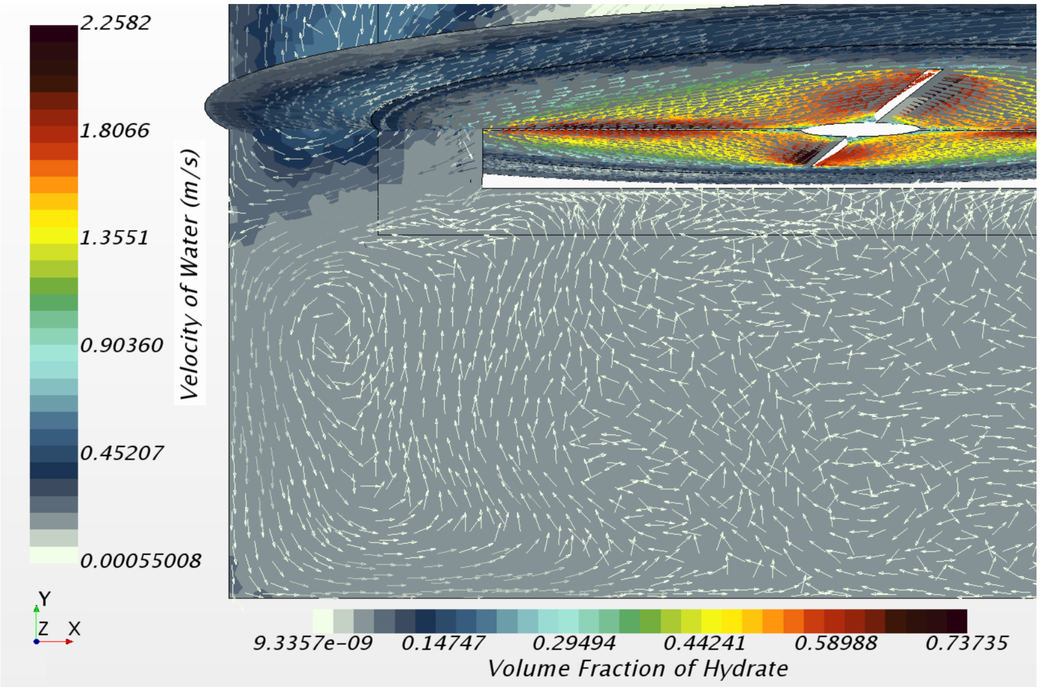

Figure 74: 2-phase CFD-PBM model: Volume fraction distribution of hydrate particles combined with velocity vector profile of the water phase at stirring rate 600 rpm. Eddies are formed in the bottom corner.

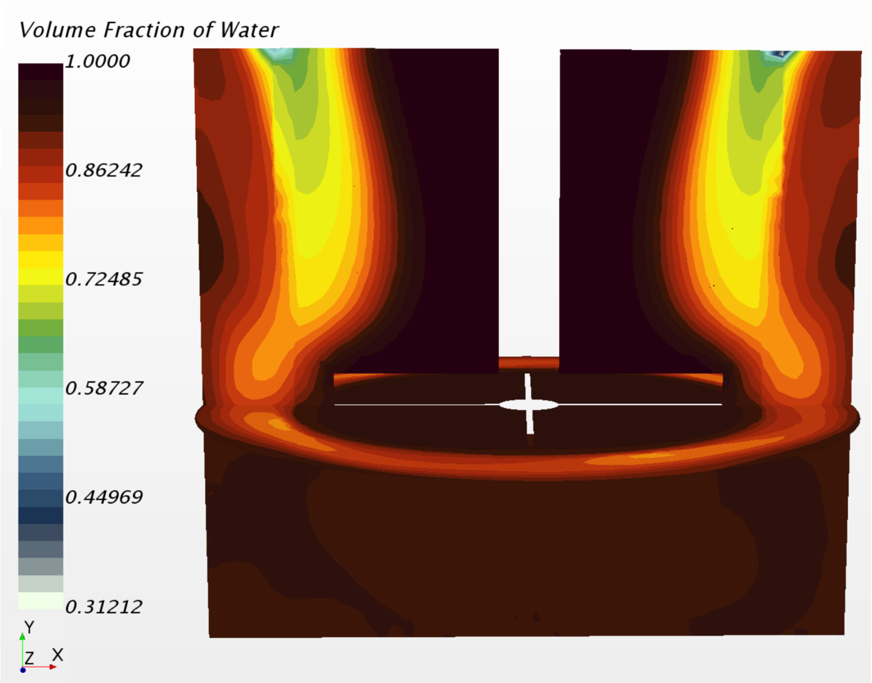

Figure 75: 2-phase CFD-PBM model: Volume fraction distribution of the water phase at stirring rate 600 rpm.

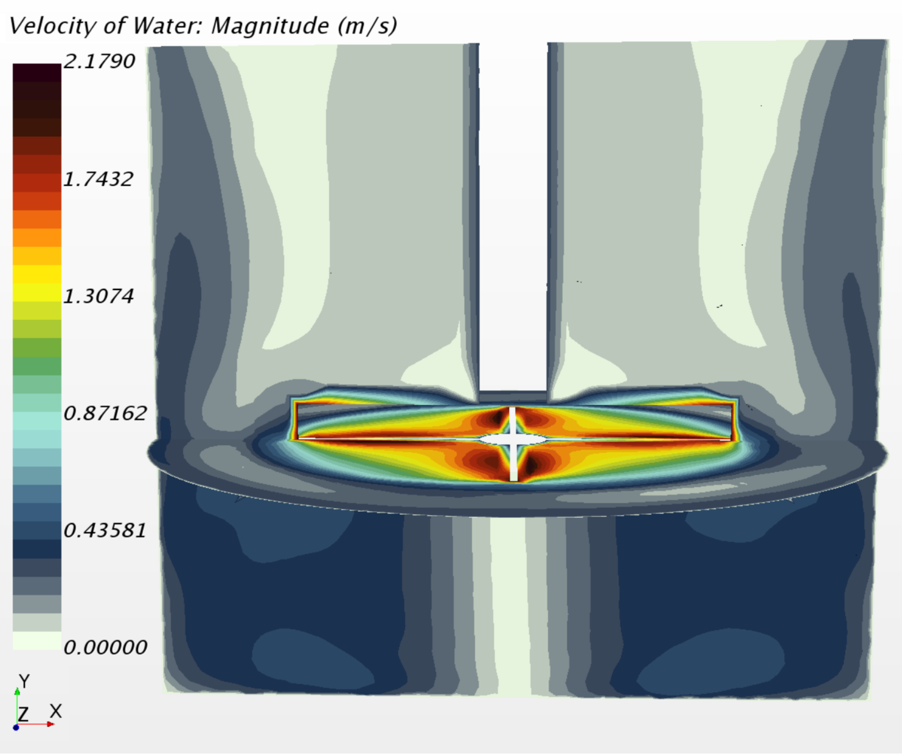

Figure 76: 2-phase CFD-PBM model: Velocity distribution of the water phase in the tank for 600 rpm.

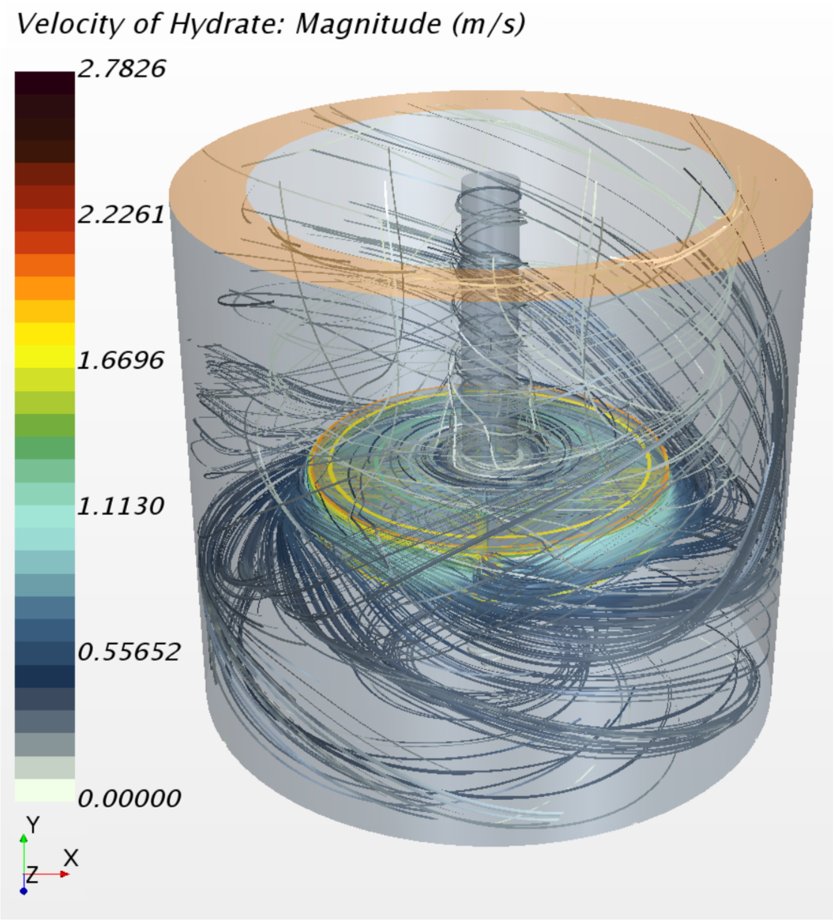

Figure 77: 2-phase CFD-PBM model: Streamlines of hydrate phase at 600 rpm.

7 Concluding remarks

Numerical studies using a three-dimensional Eulerian-Eulerian multiphase approach were conducted for the investigation of two different mechanisms that determine the granulometry of a liquid-slurry flow using the simulation software Star-CCM+. In addition, an analytical analysis of particle size and development was also done. Properties like velocity, volume fraction, shear rate, TKE, y+ values and adhesive forces were investigated. The aim was to achieve better knowledge of how the gas hydrate particles disperse due to turbulent diffusion in an agitated high water-cut system using a 5-phase CFD model. In addition, a 2-phase CFD-PBM model was developed where chemical growth of hydrate particles were studied and analysed. Furthermore, mesh independence and validation of the simulations was conducted.

The results from the analytical analysis showed an interesting trend of decreasing particle diameter size with stirring rate for all methods used. However, almost every method was not in coherence with the work of Herri et al. [1] regarding the magnitude for particle diameter size, except for the implicit relation from Zerpa et al. [2]. This method had values of the same magnitude as Herri et al. [1], but an important contrast was the opposite development of particle diameter size with stirring rate.

The numerical simulations using the 5-phase CFD model did not complete, hence the particle diameter-rpm plots did not show convergence. However, a concept was developed, describing a "bell" shaped curve for the particle diameter. Low shear rate and stirring rate result in hydrates to stay at the water-gas interphase due to buoyancy. If the stirring rate is increased, the largest particles are transported up to the location of the sensor, increasing the mean particle diameter. Eventually, at high stirring rates, the mean particle diameter size is reduced again due to the slurry becoming homogeneous. The measurements done by Herri et al. [1] could have been influenced by the left branch of the "bell". However, particle size distribution due to turbulent diffusion was described with streamlines of the gas hydrate particles, as well as velocity profiles of the continuous phase combined with volume fraction of the hydrate phase. It was shown that the largest particles were located in the top area of the stirred tank.

The numerical simulations using the 2-phase CFD-PBM model revealed that the particle diameter size and growth of the hydrates increased with lower stirring rates. This is also in coherence with the analytical analysis done in this thesis. An explanation could be more particles that are present in the top area of the stirred tank at a lower stirring rate, where both the concentration of methane and growth rate are largest, which may result in increasingly larger hydrate particles around the top boundary of the tank. However, accumulation of particles is eventually in the bottom of the tank since velocity profiles of the continuous phase show the transport of the fluid in a downwards motion. However, the results from the 2-phase CFD-PBM model does not appear to be in qualitative agreement with the simulated PBM model from Herri et al. [1], which had an increasing particle diameter with stirring rate. Figure 40 from Herri et al. [1], shows values of 23 and 8 μm for 600 and 250 rpm, respectively. In the 2-phase CFD-PBM model, values for the same stirring rates are 0.25 and 0.6 μm at terminal condition, respectively. However, maximum values are 1 μm for 600 rpm and 2.6 μm for 250 rpm. A quantitative agreement with Herri et al. [1] was not found due to difficulties comparing the models.

8 Further work

Based on the work done in this thesis, there are several possibilities for further work:

- 2-phase CFD-PBM model: couple the moments directly to the hydrate phase and use the procedure described in section 4.4. Hence, a better estimation of the growth rate will be obtained, as well as a better representation of particle growth. Furthermore, agglomeration could also be introduced.

9 Appendix

Implicit relation for particle size agglomerate D_{eq}

This section presents the calculation method of equation (66) shown by both Zerpa et al. [2] and Balakin et al. [32]. This equation could be simplified to:

$$Z^3 - \frac{A\,(1 - BZ)^2}{1 - CZ} = 0, \tag{67}$$

where $Z = x^{0.5}$, $A = F_a/d_0^2\mu_o\gamma$, $B = \phi_{hyd}/\phi_{max}$ and $C = \phi_{hyd}$. It is further transformed to the canonical form:

$$aZ^4 + bZ^3 + cZ^2 + dZ + e = 0. \tag{68}$$

The coefficients are $a = -C$, $b = 1$, $c = -AB^2$, $d = 2AB$, $e = -A$ with discriminants:

$$\Delta_0 = c^2 - 3bd + 12ae \tag{69}$$

and

$$\Delta_1 = 2c^3 - 9bcd + 27b^2e + 27ad^2 - 72ace. \tag{70}$$

The following coefficients are further found:

$$Q = \sqrt[3]{\frac{\Delta_1 + \sqrt{\Delta_1^2 - 4\Delta_0^3}}{2}} \tag{71}$$

$$p = \frac{8ac - 3b^2}{8a^2} \tag{72}$$

$$S = \frac{1}{2}\sqrt{-\frac{2}{3}p + \frac{1}{3a}\left(Q + \frac{\Delta_0}{Q}\right)} \tag{73}$$

and

$$q = \frac{b^3 - 4abc + 8a^2d}{8a^3}. \tag{74}$$

The first group of roots is:

$$Z_{1,2} = -\frac{b}{4a} - S \pm \frac{1}{2}\sqrt{-4S^2 - 2p + \frac{q}{S}}. \tag{75}$$

The second group of roots:

$$Z_{3,4} = -\frac{b}{4a} + S \pm \frac{1}{2}\sqrt{-4S^2 - 2p - \frac{q}{S}}. \tag{76}$$

The first group of roots has complex values of A, B and C. These are then physically meaningless. The second group however, are real numbers. Z_3 results in too large $\frac{d_a}{d_0}$, but Z_4 gives a satisfying result which can be viewed in table 16.

10 Bibliography

References

[1] Jean-Michel Herri, Jean-Stéphane Pic, Frédéric Gruy, and Michel Cournil. Methane hydrate crystallization mechanism from in-situ particle sizing. *AIChE Journal*, 45(3):590–602, 1999.

[2] Luis E Zerpa, E Dendy Sloan, Amadeu K Sum, and Carolyn A Koh. Overview of csmhyk: A transient hydrate formation model. *Journal of Petroleum Science and Engineering*, 98:122–129, 2012.

[3] Keith A Kvenvolden. Methane hydrate — a major reservoir of carbon in the shallow geosphere? *Chemical geology*, 71(1-3):41–51, 1988.

[4] E Dendy Sloan Jr and Carolyn Koh. *Clathrate hydrates of natural gases*. CRC press, 2007.

[5] National Energy Technology Laboratory. 2012 Ignik Sikumi Gas Hydrate Field Trail. `https://www.netl.doe.gov/research/oil-and-gas/methane-hydrates/co2-ch4exchange`, 2012. Online accessed 05-april-2018.

[6] Brian Anderson, Ray Boswell, Timothy S Collett, Helen Farrell, Satoshi Ohtsuki, Mark White, and Margarita Zyrianova. Review of the findings of the iġnick sikumi co 2–ch 4 gas hydrate exchange field trial. In *Proceedings of the 8th international conference on gas hydrates (ICGH8-2014)*, volume 28, 2014.

[7] E Dendy Sloan Jr. *Fundamental principles and applications of natural gas hydrates*, volume 426. Nature Publishing Group, 2003.

[8] John Carroll. *Natural gas hydrates: a guide for engineers*. Gulf Professional Publishing, 2009.

[9] Karin Andreassen. *Marine Geophysics, lecture notes for Geo-3123*, volume 106. 2009.

[10] Kvamme B. Re: Ptek232: Fundamentals of natural gas hydrates and practical implications, 2017.

[11] E Dendy Sloan and Carolyn A Koh. Clathrate hydrates of natural gases third edition. *Chemical Industries-New York Then Boca Raton-Marcel Dekker Then CRC Press-*, 119, 2008.

[12] P Englezos, N Kalogerakis, PD Dholabhai, and PR Bishnoi. Kinetics of formation of methane and ethane gas hydrates. *Chemical Engineering Science*, 42(11):2647–2658, 1987.

[13] Boris V. Balakin. *Experimental and theoretical study of the flow, aggregation and deposition of gas hydrate particles.* PhD thesis, 2010.

[14] Sanjeev V Joshi, Giovanny A Grasso, Patrick G Lafond, Ishan Rao, Eric Webb, Luis E Zerpa, E Dendy Sloan, Carolyn A Koh, and Amadeu K Sum. Experimental flowloop investigations of gas hydrate formation in high water cut systems. *Chemical Engineering Science*, 97:198–209, 2013.

[15] John David Anderson and J Wendt. *Computational fluid dynamics*, volume 206. Springer, 1995.

[16] Michael Schäfer. *Computational engineering: Introduction to numerical methods.* Springer, 2006.

[17] Hyun-Joo Kim. Multiphase Modelling in STAR-CCM+. `https://mdx2.plm.automation.siemens.com/sites/default/files/Presentation/34%20Korea2012_Multiphase_HJKim.pdf`, 2012. Online accessed 20-December-2017.

[18] Donald Sadoway: Massachusetts Institute of Technology: MIT OpenCourseWare. 3.091SC Introduction to Solid State Chemistry. `https://ocw.mit.edu`, Fall 2010. Online accessed 20-march-2018.

[19] Christopher Earls Brennen and Christopher E Brennen. *Fundamentals of multiphase flow.* Cambridge university press, 2005.

[20] Siemens PLM Software Simcenter. STAR-CCM+ user guide for version 12.02, 2018.

[21] Clayton T Crowe, John D Schwarzkopf, Martin Sommerfeld, and Yutaka Tsuji. *Multiphase flows with droplets and particles.* CRC press, 2011.

[22] Chemistry LibreTexts. Lennard-Jones Potential. `https://chem.libretexts.org/Core/Physical_and_Theoretical_Chemistry/Physical_Properties_of_Matter/Atomic_and_Molecular_Properties/Intermolecular_Forces/Specific_Interactions/Lennard-Jones_Potential`, 2017. Online accessed 21-January-2018.

[23] Peter Atkins and Julio De Paula. *Physical chemistry for the life sciences.* Oxford University Press, USA, 2011.

[24] Andrew Burrows, John Holman, Andrew Parsons, Gwen Pilling, and Gareth Price. *Chemistry 3: introducing inorganic, organic and physical chemistry.* Oxford University Press, 2017.

[25] Fabio L Leite, Carolina C Bueno, Alessandra L Da Róz, Ervino C Ziemath, and Osvaldo N Oliveira. Theoretical models for surface forces and adhesion and their measurement using atomic force microscopy. *International journal of molecular sciences*, 13(10):12773–12856, 2012.

[26] The University of Virginia. Properties of water. `http://galileo.phys.virginia.edu/classes/304/h2o.pdf`. Online accessed 11-March-2018.

[27] Matic Šavli. Turbulence kinetic energy–tke. In *University of Ljubljana, Faculty of Mathematics and Physics, Department of Meteorology. Seminar: 4th Class. May*, volume 27, 2012.

[28] Jean-Michel Herri, Frédéric Gruy, Jean-Stéphane Pic, Michel Cournil, Béatrice Cingotti, and Anne Sinquin. Interest of in situ turbidimetry for the characterization of methane hydrate crystallization: Application to the study of kinetic inhibitors. *Chemical Engineering Science*, 54(12):1849–1858, 1999.

[29] Peace Software. Properties of water. `http://www.peacesoftware.de/einigewerte/wasser_dampf_e.html`. Online accessed 19-october-2017.

[30] Herold G Dehling, Timo Gottschalk, and Alex C Hoffmann. *Stochastic modelling in process technology*, volume 211. Elsevier, 2007.

[31] Guan-Heng Yeoh, Chi Pok Cheung, and Jiyuan Tu. *Multiphase flow analysis using population balance modeling: bubbles, drops and particles.* Butterworth-Heinemann, 2013.

[32] Boris V Balakin, Simon Lo, Pawel Kosinski, and Alex C Hoffmann. Modelling agglomeration and deposition of gas hydrates in industrial pipelines with combined cfd-pbm technique. *Chemical Engineering Science*, 153:45–57, 2016.

[33] A D_ Randolph. A population balance for countable entities. *The canadian journal of chemical engineering*, 42(6):280–281, 1964.

[34] Anthony Vysniauskas and PR Bishnoi. A kinetic study of methane hydrate formation. *Chemical Engineering Science*, 38(7):1061–1072, 1983.

[35] AG Jones, J Hostomsky, and Li Zhou. On the effect of liquid mixing rate on primary crystal size during the gas-liquid precipitation of calcium carbonate. *Chemical Engineering Science*, 47(13-14):3817–3824, 1992.

[36] A Vysniauskas and PR Bishnoi. Kinetics of ethane hydrate formation. *Chemical Engineering Science*, 40(2):299–303, 1985.

[37] Per Skovborg and Peter Rasmussen. A mass transport limited model for the growth of methane and ethane gas hydrates. *Chemical Engineering Science*, 49(8):1131–1143, 1994.

[38] Cécile Gaillard. *Cinétique de formation de l'hydrate de méthane dans une boucle de laboratoire.* PhD thesis, Toulouse, INPT, 1996.

[39] SG Kane, TW Evans, PLT Brian, and AF Sarofim. Determination of the kinetics of secondary nucleation in batch crystallizers. *AIChE Journal*, 20(5):855–862, 1974.

[40] P Snabre and P Mills. I. rheology of weakly flocculated suspensions of rigid particles. *Journal de Physique III*, 6(12):1811–1834, 1996.

[41] Simon Lo et al. Cfd modelling of hydrate formation in oil-dominated flows. In *Offshore Technology Conference*. Offshore Technology Conference, 2011.

[42] Aslak S Hellestø, Maryam Ghaffari, Boris V Balakin, and Alex C Hoffmann. A parametric study of cohesive particle agglomeration in a shear flow—numerical simulations by the discrete element method. *Journal of Dispersion Science and Technology*, 38(5):611–620, 2017.

[43] Srinivas Chimmili, Deepak Doraiswamy, and Rakesh K Gupta. Shear-induced agglomeration of particulate suspensions. *Industrial & engineering chemistry research*, 37(6):2073–2077, 1998.

[44] Mühle K. edited by B. Dobias. Coagulation and flocculation: theory and application. surfactant science serie. 47:355–390, 1993.

[45] M Von Smoluchowski. M. von smoluchowski, z. phys. chem. 92, 129 (1917). *Z. Phys. Chem.*, 92:129, 1917.

[46] Jean-Stéphane Pic. *Etude du mécanisme d'action d'un inhibiteur cinétique sur la cristallisation de l'hydrate de méthane.* PhD thesis, Ecole Nationale Supérieure des Mines de Saint-Etienne, 2000.

[47] Palermo I. Sinquin, A. and Y. Peysson. Oil gas sci. technol. - revue d ifp energies nouvelles. 59:41–57, 2004.

[48] Sijia Hu and Carolyn A Koh. Interfacial properties and mechanisms dominating gas hydrate cohesion and adhesion in liquid and vapor hydrocarbon phases. *Langmuir*, 33(42):11299–11309, 2017.

[49] Olivier Bonnefoy, Frédéric Gruy, and J-M Herri. Van der waals interactions in systems involving gas hydrates. *Fluid Phase Equilibria*, 231(2):176–187, 2005.

[50] K. Mühle. Flock stability in laminar and turbulent flow. in: Coagulation and flocculation: Theory and applications (chapter 8). 1996.

[51] Ramiar Sadegh-Vaziri, Kristin Ludwig, Kai Sundmacher, and Matthaus U Babler. Mechanisms behind overshoots in mean cluster size profiles in aggregation-breakup processes. *Journal of colloid and interface science*, 2018.